Helsinki University of Technology Publications in Physical Metallurgy
and Materials Science
Espoo 2003

# A STUDY ON THE EROSION AND EROSION-OXIDATION OF METAL MATRIX COMPOSITES

**Xuwen Liu**



Dissertation for the degree of Doctor of Technology to be presented with due permission for public examination and debate in Auditorium V1 at Department of Materials Science and Rock Engineering (Vuorimiehentie 2A, Espoo, Finland), at Helsinki University of Technology on the 31st of October 2003 at 12 o'clock noon.

Helsinki University of Technology
Department of Materials Science and Rock Engineering
Laboratory of Physical Metallurgy and Materials Science

Teknillinen korkeakoulu
Materiaali- ja kallioteknikan osasto

Distribution: Laboratory of Physical Metallurgy and Materials Science
Helsinki University of Technology
Department of Materials Science and Rock Engineering
Laboratory of Physical Metallurgy and Materials Science
P. O. Box 6200
Fin-02015 HUT
Tel. +358-9-451 2683
Fax +358-9-451 2677


ISBN 951-22-6756-X
ISSN 1239-0518
Otamedia Oy
Espoo 2003

Xuwen, Liu: A Study on the Erosion and Erosion-oxidation of Metal Matrix Composites. Helsinki, 2003, 108 pp. ISBN 951-22-6756-X. ISSN 1239-0518©

## Abstract:

The potential of metal matrix composites (MMCs) as new generation erosion and erosion-corrosion resistant materials is investigated. As a type of wear attack, erosion involves destructive impact of free-moving particles on a solid. The high-strain-rate and hence adiabatic deformation conditions that the target surface experiences during erosion are often the reasons behind the poor correlation of erosion rate with static mechanical properties of the targets, imparting difficuties on erosion study. On the other hand, a good correlation exists between erosion rate and the thermophysical properties of the target. This, however, suggests limited possibilities of enhancing erosion resistance on a monolithic alloy. A literature study at the beginning elaborates the complex of erosion as a physical phenomenon, and lies the theoretical base for the experiment.

In the experiment, nickel-chromium superalloy- and heat resistant steel-based composites are manufactured through a powder metallurgy route. Ceramic particles are added at different volume fractions as the reinforcements. Efforts are made to optimise the powder mixing and powder consolidation procedures to ensure a homogeneous microstructure and full densification of the final composites. Two types of erosion tester are used in the study: a centrifugal erosion tester is for the erosion tests at room temperature, and a gas-blast erosion tester is for the erosion-oxidation tests at high temperature. With the gas-blast tester, both the temperature and oxygen concentration is controlled to simulate real application situations.

The discussion is focused on the tests under a $60^{o}$ angle of impact. Optical and SEM (scanning electron microscopy) observations are carried out on the eroded surfaces to assess the damage pattern and general behaviour of the studying composites. Meanwhile, on cross-sectioned specimens the bonding and material dissolution at the matrix/reinforcement interfacial regions and the deformation situation at the sub-surfaces are examined by EDS (energy dispersion spectroscopy) and microhardness measurements to reveal the erosion mechanisms of the composites. The experimental results suggest that the strain localisation mode is valid in describing erosion process of a ductile metal, but may need modifications when applying to MMCs. The erosion response of a MMC system is determined by not only the internal parameters of the composites, but also external factors involving all parameters of erosion. In addition, this study provides useful guidelines to the selection of composite systems having high erosion resistance for industrial applications and to the future study as well.

## Preface

This thesis has been prepared in the Laboratory of Physical Metallurgy and Materials Science at Helsinki University of Technology during the years 2000 – 2003.

I would like to express my sincere gratitude to Professor Veikko Lindroos, my supervisor, for providing me the opportunity to work and study in the laboratory, and for his encouragement, valuable suggestions and unconditional support to my research. In many delicate moments, he has granted me almost complete freedom to carry out this thesis in the way that I have chosen, with trust, flexibility and patience.

I would like to thank Dr. Emmanouel Pagounis for good advice and intense discussions. His wide experiences and solid knowledge in materials science has in many occasions inspired me to explore the fields with which the thesis deals.

I am grateful to Mr. Markku Pohjola, for his role in conducting the tests in the study, and for the open discussions that have become so important in pinpointing the mechanisms and forming the ideas for the thesis. Special thanks are due to Mr. Juha Peltonen and Mr. Jussi Laurila, for their precious advice and skilful operation in microhardness measurements. In addition, I want to thank Mrs. Desiree Luhulima for her kind help in SEM observation and sample preparation. I am very grateful to all the members in the research project (ERCOMAT – Erosion and erosion-corrosion resistant powder metallurgical materials for the applications of energy technology), for their indispensable contribution to the completion and success of the whole body of the experimental work that is crucial for the thesis.

I am indebted to Professor Juha Pietikäinen, for multiple discussions. Special thanks are due to Professor Roman Nowak, for his knowledge and his view toward tomorrow's materials science, and for his extraordinary sense of humour, making chat with him always enjoyable. I have the pleasure to thank Dr. Risto Toivanen, for the various help during my study. Thanks are also due to Mrs. Outi Söderberg, Mrs. Arja Teramo, Mrs. Pirjo Korpiola and all staff of the Laboratory of Physical Metallurgy and Materials Science, for co-operation and friendship. Many thanks are due to Mr. Yossi Ezer for being a good friend and having great time together.

The financial support of The Technology Development Centre of Finland (TEKES) and companies attending the project (Fortum Oyj, Metso Oyj, Wärtsilä Oyj and Foster Wheeler Energia Oy) are greatly acknowledged.

My warm thanks are due to my mother and my mother- and father-in-law, for understanding and encouragement that has become so important in helping me walk out those difficult situations in the passing years.

Finally, my deepest emotional thanks are due to Mari for her love, understanding, endless patience and unconditional support, and to my son and daughter for making me a father and being the best comfort in many painful moments during the thesis work.

Espoo
October 2003 Xuwen Liu

# Contents

# 1. Introduction

In systems in which particles move at high speeds in a fluid stream, serious wear attack has been observed. This type of wear is called erosion and can be defined as the wear resulting from the impact of free-moving particles on a solid. Erosion has been a problem in many industrial operations, for instance, in regenerators, air mills, gas turbines, and fluid-bed systems. One example of using fluid-bed systems in industry is the bubbling fluidised combustor. This process is attractive because of the extremely high heat transfer rates that can be achieved and for its ability to handle high sulphur coal. However, erosion or erosion-corrosion from coal powder and the remaining silica in the sulphur-containing atmosphere has been the major obstacle in the development of this process [1]. Another example is the fluid bed process for catalytic cracking of oil to lower molecular weight hydrocarbons. This is perhaps the most expensive erosion problem ever encountered by industry, as small catalyst particles circulating at very large flow rates through vessels and pipes show high destructive power [2].

The first technical papers on erosion began to appear at the beginning of the last century. Until the 1940's, ingenious solutions had been devised for many practical erosion problems. However, little progress had been made on the fundamental understanding of the mechanisms by which particles remove material. Attempts to understand the basic mechanisms involved in erosion started after the Second World War and have continued to the present day [2].

Historically, studies on the mechanisms of erosion were focused on ductile metals until the 1970's, when publications from systematic research on the erosion of brittle materials started to appear. This can be seen from the wide availability of review articles on the erosion mechanisms of ductile materials in the 1970's and 1980's [3-8], while much less on brittle materials in the same period [9]. However, an extraordinary amount of work in the area of erosion of brittle materials has been carried out since the mid-1980's, and a review article published in the early 1990's [10] sums up much of the work.

## 1.1 The development of the Erosion Model on Ductile Metals

There is general agreement concerning the erosion mechanisms of ductile metals that extensive plastic deformation is necessary before metal removal occurs. This is reflected by a remarkable feature of ductile erosion behaviour: the variation of the weight loss with impact angle is very similar for materials with widely different thermal and physical properties (Fig. 1.1, 1.2). This, according to Finnie [2], not only is the erosion mechanism the same in all cases, but it involves primarily a single physical property which most would agree is plastic deformation.

There is, however, appreciable disagreement about what material properties, or what criteria, are critical for specifying when erosive loss on ductile metals occurs. Therefore, different theories concerning the erosion mechanisms of ductile metals have been developed. In the following, models representing pioneering efforts and the recent development in the study of erosion of ductile metals are introduced.

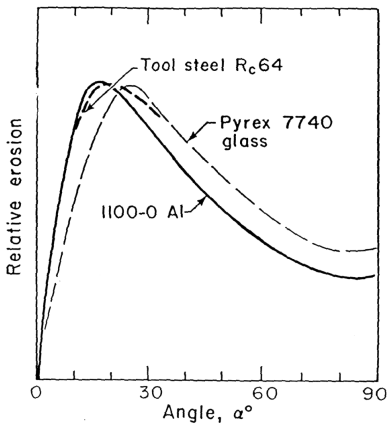


Fig. 1.1 Erosion of 1100-0 Al, Pyrez 7740 glass and a quenched untempered tool steel with SiC particles (9μm) at 152 m/s. Maximum erosion is used to normalise the curves [2].

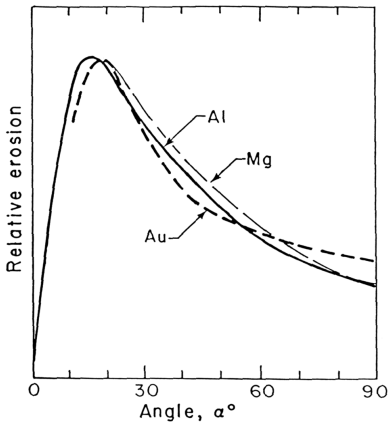


Fig. 1.2 Erosion of Al, Au and Mg by 127μm SiC particles. Maximum is used to normalise the curves. Erosion velocities were: Al, 168 m/s; Au, 132 m/s; Mg, 76 m/s [2].

### 1.1.1 General Review of Erosion Model on Ductile Metals

In this section, representative models are introduced in an attempt to track the developments in the understanding of the fundamentals of erosion.

**Bitter's model**

Bitter attempted cover both ductile and brittle erosion using the same equations [11, 12]. He considered erosion to consist of two simultaneous processes, "cutting wear" and "deformation wear". For ductile metals, cutting wear predominates at low angles, while at high angles deformation wear predominates. In the case of hard and brittle materials, only deformation wear is responsible for material loss and cutting is negligible. The model was then developed based on elastic contact stress calculations and energy balances. If $W_D$ and $W_C$ represent deformation and cutting wear loss, respectively, Bitter's models are given as

$$W_D = \frac{\frac{1}{2}M(V\sin\alpha - K)^2}{\varepsilon} \tag{1-1}$$

$$W_{C_1} = \frac{2MC\ (V\sin\alpha - K)^2}{\sqrt{V\sin\alpha}}\left(V\cos\alpha - \frac{C\ (V\sin\alpha - K)^2}{\sqrt{V\sin\alpha}}Q\ \right) \tag{1-2}$$

$$W_{C_2} = \frac{\frac{1}{2}\left[V^2\cos^2\alpha - K_1(V\sin\alpha - K)^{3/2}\right]}{Q} \tag{1-3}$$

In which:

$W_{C_1}$ = cutting wear loss if impinging particle stays in the target after collision,

$W_{C_2}$ = cutting wear loss if particle leaves the target surface after collision,

$\varepsilon$ & $Q$ = wear factor of deformation and cutting wear, respectively,

$V$ = incident velocity of erosive particle,

$M$ = total mass of impinging particles,

$K$ & $K_1$ = constants determined by the elastic properties of target,

$C$ = constant and

$\alpha$ = impact angle.

In the equations, $\varepsilon$ and $Q$ are defined as the energy needed to remove or scratch a unit volume of material from the target by deformation and cutting wear, respectively, and their values depend on the mechanical properties of the target. There is, however, no description in the studies [11, 12] about how this amount of energy is applied in removing material. This simply leads to a suggestion that, as far as the erosive particle loses $\varepsilon$ or $Q$ amount of energy from their initial kinetic energy, a unit of material is lost from the target. Moreover, the constants $K$ and $C$ in the equations are determined purely by the elastic constants of the erosive particle and the target. Therefore, though this model can predicts the variation of the weight loss with impact angle in some cases, it sheds little light on the understanding of the fundamental processes involved in erosion. Finally, this model also suggests that the erosion resistance of materials should have a direct relation to their mechanical properties, mostly to their elasticity.

**Finnie's model**

Finnie's approach is to analyse the motion of the striking particle sweeping over the target surface and removing material [13, 14]. In Fig. 1.3, a rigid polyhedral grain strikes on the surface of a ductile metal and does not fracture. If little rotation of the particle is assumed, the co-ordinates of the particle's centre of gravity $X$, $Y$ and its tip $X_T$, $Y_T$ are related by $X_T \approx x + r\phi$ and $Y \approx Y_T$.

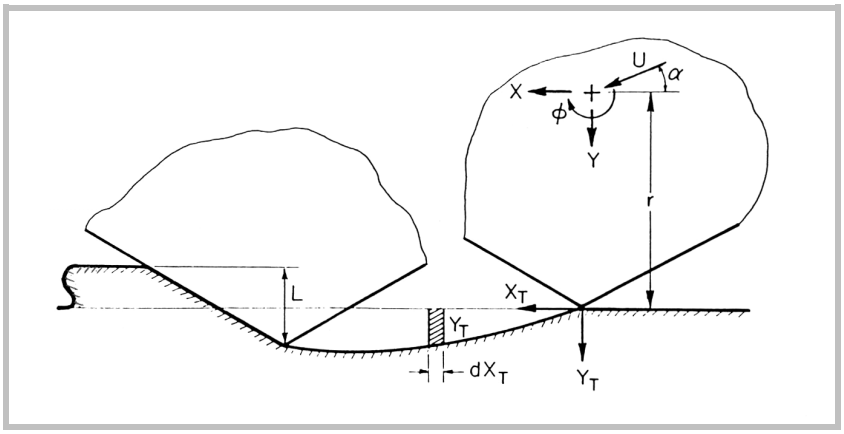


Fig. 1.3 Idealised two-dimensional model of a rigid grain cutting into a ductile metal [7].

As the particle's rotation is limited, the cutting configuration is approximately and geometrically similar while the particle cuts into the surface. In addition, with sharp tip, considerable strain should occur from the beginning of the cutting process, suggesting the progress of the plastic deformation of the target under full work-hardened conditions. These assumptions lead him to assume further that the ratio of vertical to horizontal force ($K$) is a constant during cutting. Therefore, a constant plastic flow pressure exists with its horizontal component being given as $p$. Finally, the volume removed is taken as the product of the area swept out by the tip of the particle and the width $b$ of the cutting edge. That is

$$V = b\int Y_T dX_T = b\int_0^{t_c} Y_T\left(\frac{dX_T}{dt}\right) \tag{1-4}$$

where $t$ is the time from the start of cutting and $t_c$ the time at which the particle ceases to cut [15]. By introducing the factor $P$, Finnie solved the equation of motion of the colliding particle.

$$P = \frac{K}{\left(1+\frac{mr^2}{I}\right)} \tag{1-5}$$

in which, $m$ is the mass of an individual particle and $I$ the mass moment of inertia about its centre of gravity. The resulting expressions for the volume $V$ removed by a total mass $M$ of impinging particles are

$$V = \frac{cMU^2}{2\psi p}\left[\frac{2}{K}\left(\sin 2\alpha - \frac{2}{p}\sin^2\alpha\right)\right] \qquad \alpha \le \tan^{-1}\frac{P}{2} \tag{1-6}$$

when the particle leaves the surface while still cutting, and

$$V = \frac{cMU^2}{2\psi p}\left[\frac{\cos^2\alpha}{\left(1+\frac{mr^2}{I}\right)}\right] \qquad \alpha \geq \tan^{-1}\frac{P}{2} \tag{1-7}$$

when the particle comes to rest while cutting. In the equations, $c$ is the fraction of particles of all that cut the target in the idealised manner [13].

Examining the model with test results, it shows that it can well predict the erosion of pure metals as a function of impact angle, providing the angle is less than 45°. What is more, the model can also predict the erosion dependence on particle velocity after a slight modification [14]. The modified equation explains the observed values of the velocity exponent, typically 2.3 to 2.4 and ranging from 2 to 3 for ductile metals, while the original model (Eqs. 1-6 and 1-7) predicts a relation of $V \sim U^2$. The most significant limitation of this model is that it can not detect situations of erosion at higher angles, for example $\alpha > 45^o$, since at high angles, much of the material at target surface is at first only displaced rather than removed straight away. In addition, it is noticed that the horizontal component of the flow pressure $p$ is the only means of comparing the relative erosion resistance of different materials. As studies have shown [15, 16] that Vickers' hardness cannot be relied upon to predict relative erosion resistance of ductile materials, this model becomes incapable when selecting materials for erosion problem. Finally, factor $c$, the fraction of particle cut the target surface in the idealised manner, is considered too difficult to estimate.

**Hutchings' treatment**

Hutchings' treatment has some similarities with Finnie's idea. However, Hutchings has revealed, based on the results of single-impact experiments, that there are three possible types of plastic deformation induced by hard irregular particle impact that can all lead to metal removal: plowing, type *I* cutting, and type *II* cutting [17]. Figure 1.4 is the schematic drawing of the three types of deformation. In the plowing deformation, the lip material at the exit end of the crater is pushed up in front of the striking particle and folded over onto the undisturbed surface (Fig. 1.4a). By no means can all the material displaced from the crater be extruded into the lip. For example, in one study the lip represents only about 10 to 25 percent of the total crater volume, and the other displaced material forms less strained ridges around the sides of the crater [18]. This type of deformation is expected from the impact of spherical particles or irregular particles of rounded surface. The other two types of deformation are produced by sharp irregular particles. At an impact angle of 30° and rake angle in a range between –17° and –90°, type *I* cutting deformation is resulted. The triangular shape of indentation is an indication that appreciable

forward rotation is experienced by the particle rebounding from the surface (Fig. 1.4b). Type *II* cutting (Fig. 1.4c) results from backward rotation of the striking particle having a rake angle between 0 to 17$^{o}$ and impacting at a low angle, for example 30$^{o}$. This type of deformation is a perfect machining action, as a chip of material can be cut out from the target surface by a single strike. However, since it occurs over a narrower range of rake angle, type *II* cutting is rare compared to type *I* cutting in practice.

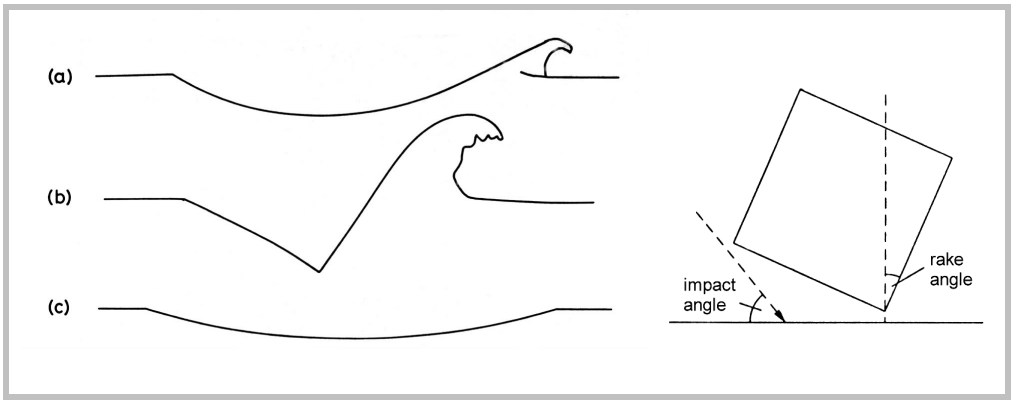


Fig. 1.4 Three types of plastic deformation. Impact direction left to right. (a) Plowing deformation. (b) Type *I* cutting. (c) Type *II* cutting [17].

The significance of Hutchings' treatment is seen in three aspects [17, 19]. Firstly, by revealing the existence of the three types of deformation, this treatment covers theoretically all the possibilities of solid particle erosion, for example erosion by irregular particle of sharp or rounded edges at all impact angles. Secondly, it assumes a constant yield pressure acting over the area of the particle that is plastically deforming the target, suggesting a force vector continually changing direction during impact. In Finnie's model, a constant ratio of normal to tangential force, and hence a constant force vector, is assumed. This rationalises the fact that Finnie's model overestimates erosion rates, since within a critical range of rake angle at each impact angle, a large amount of impinging particles rotates forward (Type *I* cutting), and do not remove material directly, but displace it at first. Finally, this model leads to a physical explanation of the observed dependence of crater volume and impact velocity, in which the exponent of the velocity is usually between 2 and 3, while 2 was predicted in the original treatment by Finnie. According to this model, the origin of the higher exponent is due to the impact of spherical particles resulting in plowing deformation. As the impact velocity of a sphere increases, the angle of the exit "ramp" of the crater becomes steeper and therefore, the sphere loses more of its energy in the later stage of the impact. This actually creates an extra volume of the crater, which is a function of velocity cubed. The total volume loss of the target is therefore the combination of the dominant term involving velocity squared and a much smaller term involving velocity cubed, resulting in the high velocity exponent observed.

Though the treatment of Hutchings makes good progress toward understanding the basic mechanisms involved in erosion, its limitation is still obvious. Mostly, there is only one material property, the yield pressure of the target, involved in the treatment. Therefore, the question posed earlier why strength measurements and hardness tests give such poor indication of the relative erosion rate of ductile materials remains unanswered.

**Sundararajan's model**

The development in erosion study has been driven by not only industrial interests but also the availability of new techniques. The most important progress has come from the examination of the eroding surface by using scanning electron microscope (SEM). This has led to new models that relate the erosion rate to the physical and mechanical properties of the target material, as SEM provides a much clearer picture of the structure of the eroding surface. The localisation model developed by Sundararajan is an attractive one among them. By emphasising the high-strain-rate nature of the deformation that target surface experiences during erosion, this model successively connects the mechanical and thermophysical properties of a ductile metal with its erosion rate. The basic idea of the model is that erosion loss is processed under high-strain-rate and hence adiabatic deformation conditions, and therefore, the mechanical response of the target is dynamic. Under the unique deformation conditions, strain localisation occurs in a narrow range around the impact sites, leading to the formation of craters with heavily strained lips and/or platelets at the sides. The erosion loss of ductile metals is then intimately related to the formation and fracture of the lips and/or platelets. It is declared that this model is able to explain the six general observations found in steady-state erosion of ductile metals (Table 1.1).

Table 1.1 General observations in steady-state erosion of ductile metals [8]

| | Observations ($E$, dimensionless erosion rate, grams of target loss per gram of erosive) |
|---|---|
| 1 | $E$ varies as (impact velocity)$^n$, where "n" is usually between 2.2 to 3.0 (mean value of 2.4). |
| 2 | A maximum in the erosion rate for ductile metals is found at an impact angle of $15^o$ to $30^o$, or in the case of hardened steel at a range of $60^o$ to $90^o$. |
| 3 | For a given alloy, $E$ is not changed by large increases in hardness developed by heat treatment, ageing, or cold work. |
| 4 | At low impact velocity, $v$, an incubation time is observed that increases roughly as $v^{-1}$. |
| 5 | An excellent correlation exists between the erosion rate and the thermophysical properties of target metal, i.e. the heat to raise the target metal to its melting point. |
| 6 | The erosive loss of ductile metals is intimately related to the formation and fracture of lips and/or platelets formed around the impact sites. |

**Other models**

Other interesting models for dealing with erosion of ductile metals include the *Fatigue Models* [20-22], the *Delamination Model* [23, 24], and the *Adiabatic Shear-Induced Spalling Model* [25, 26].

The ***Fatigue Models*** are built on the theories of low cycle fatigue. It assumes that, for a target undergoing steady-state erosion, each impact produces a strain increment, and hence a stain-accumulation is built up in the surface layer of the target. An element volume $V_d$ will be lost once it accumulates a critical stain $\varepsilon_c$, the fracture strain of the target. These models predict higher velocity exponent than usually observed (3 from ref. 19 and 20, 3.5 from ref. 21). What is more, all of the models of this kind can not explain the observation 5 (Table 1.1).

The ***Delamination Model*** suggests that voids nucleate beneath the impact surface, primarily at inclusions. Under steady-state erosion, the voids grow into subsurface microcracks, whose depth increases with the impact velocity. Then the target loses its surface layer by the way of delamination. The model fits only to the observation 2 (Table 1.1).

The ***Adiabatic Shear-induced Spalling Model*** argues that shear bands form instead of voids and microcracks in the deformed volume beneath the crater, since erosion is progressed under adiabatic, high-strain-rate and hence constraint deformation conditions. The removal of chunks of materials, therefore, is the result of the intersecting of the shear bands. This model provides an attractive explanation for the observation that in hardened steels the angle of maximum erosion shifts from roughly $20^o$ to close to $90^o$ as the hardness is increased to over HRC 60. This is because the shear bands form more easily in high strength (low work hardening) alloys and at high angles.

In summary, it appears that the strain localisation model is attractive in revealing the fundamentals of erosion phenomena in ductile metals. It is believed that this model can provide useful guidelines for material selection in dealing with erosion problems. Therefore, the theoretical background and the derivation of the analytical formulas of this model are detailed in the following sections. At first, the confusing phenomena concerning erosion of ductile metals are highlighted. Then, the theoretical background in the derivation of the analytical formulas is explored. Finally, the merit of this model is demonstrated by applying it to rationalising the confusing phenomena in the erosion of ductile metals.

### 1.1.2 Confusing Phenomena in the Erosion of Ductile Metals

The confusing phenomenon in erosion of ductile metal is reflected by the poor correlation of erosion rate with static mechanical properties of the targets. A good summary [27] demonstrates

a situation in which the correlation between the erosion date and various mechanical properties for different materials is examined.

**Erosion and strength**

The strength of a material can be characterised by its hardness (HV), yield ($\sigma_Y$), and ultimate tensile strength ($\sigma_{UTS}$) or the strength coefficient ($K$; $\sigma = K\varepsilon^n$, where $\sigma$ is the flow stress, $\varepsilon$ is the true plastic strain and $n$ is the strain hardening exponent). It has been found that in pure metals, stainless steels, and cast irons there is a clear correlation between material strength and erosion resistance so that an increase in strength results in higher erosion resistance. For example, a martensitic stainless steel (AISI 410SS, HV 360) exhibits higher erosion resistance than two austenitic stainless steels (AISI 304SS and 316SS, HV 160) [28]. In another example, a strengthened nodular cast iron with spherical matrix shows higher erosion resistance than a nodular cast iron with normal pearlitic matrix [29]. However, erosion data on many other alloy systems indicate that there is no consistent trend in the correlation between erosion and material strength. It has been reported that in Cu and Cu alloys, increasing material strength (or hardness) by solid solution strengthening actually degrades erosion performance [30]. In another case, the lowest erosion rate has been achieved either in solution treated or overaged (softening compared to solution treating) conditions depend on alloy systems [31, 32]. Therefore, erosion rate can not be predicted on the basis of material strength alone.

**Erosion and ductility**

Higher ductility can have either a positive or negative effect on the erosion resistance for a given alloy system. For example, in a Cu system (Cu, Cu-Zn, Cu-Al), Al-Cu alloy reinforced with $Al_2O_3$ fibres, and to some extent in cast irons, higher erosion resistance is caused by increasing alloy ductility [29, 30, 33]. However, in the case of Al-Li system, Ti alloys and 17-4 PH stainless steels, the material with low or intermediate ductility exhibits the best erosion properties [27, 28, 31].

**Erosion and mechanical energy density**

The mechanical energy density is defined as the product, $(\sigma_Y + \sigma_{UTS})\ \varepsilon_f/2$, where $\varepsilon_f$ is the tensile ductility. It is expected that the erosion rate should be directly correlated with mechanical energy density as this product reflects the combined effect of strength and ductility of an alloy system. However, among the above mentioned alloy systems, only in the case of the cast irons and the Al-Cu composites with $Al_2O_3$ fibres is the expectation realised.

**Erosion and strain hardening exponent**

From the energy point of view, higher exponent $n$ is always desired for a material exhibiting good erosion resistance. This is because that the high $n$ allows higher energy absorption capability of a material through plastic deformation by increasing both the specific energy absorption capacity (per unit volume) and the volume over which the plastic deformation occurs.

However, a careful examination of the experimental data from literature [28, 30, 31] does not indicate a consistent correlation between erosion and the *n* value of a given alloy system.

Therefore, it is clear that none of the static mechanical properties can be utilised to correlate the erosion rate of a ductile metal on a consistent basis. This is not surprising since erosion processes take place under completely different conditions compared to those under which the static properties of a ductile metal are measured. Therefore, it is quite unrealistic to expect just one parameter to characterise all aspects of erosion.

### 1.1.3 Deformation Conditions and Plastic Flow of Material Under Erosion

To develop an appropriate erosion model, it is important to understand the uniqueness of the deformation conditions that erosion involves and the plastic flow behaviour of the target under the conditions.

**Erosion deformation conditions**

It is obvious that the process of erosion loss initiates when hard particles indent the target surface plastically, though it is arguable how the final material loss is proceeded. The stress state under which the plastic deformation occurs is not uniaxial but multiaxial, similar to the indentation in normal hardness test. Therefore, the plastic zone surrounding the indenting particle is totally confined (since the target thickness is considerably larger than the plastic zone size), resulting in constrained plastic flow in the presence of a substantial component of hydrostatic compressive stress.

The most significant aspect of the deformation under erosion conditions is the strain rate $\dot{\varepsilon}$ at which the deformation occurs. In Fig. 1.5, the variation of the calculated strain rate with impact velocity is illustrated for various particle sizes [33, 34]. The calculated strain rates lie in the range of $10^3 - 10^8$ $s^{-1}$, i.e. in the regime of ultrahigh strain rates. It is also noticed that the strain rate is not only the function of the impact velocity but also of the particle size. A comparison of strain rate regimes associated with a conventional tensile test, a sliding and abrasion wear test, and an erosion test is demonstrated in Fig. 1.6.

The direct implication of such high strain rates is that plastic deformation occurs under fully adiabatic conditions. This means that the heat generated by plastic deformation is not dissipated away, which therefore leads to an increase in the temperature of the eroding material. It has been demonstrated that the requirements for the occurrence of adiabatic deformation are well satisfied during dynamic impact [35].

**The plastic flow of target under erosion**

The first characteristic of plastic flow under erosion is dynamic response. It has been found that the flow stress for many metals has a linear relation with the strain rate, and the rate sensitivity of the flow stress increases rapidly when the strain rates are over $10^3$ $s^{-1}$ [36]. From Fig. 1.5, it can be inferred that erosion processes that are most probably encountered in practice involve deformation under strain rates between $10^4$ to $10^8$ $s^{-1}$. Therefore, investigations on erosion should be carried out under dynamic deformation conditions. A dynamic indentation technique has been developed and used successively in studying the flow behaviour of target materials under high-strain-rate deformation [35].

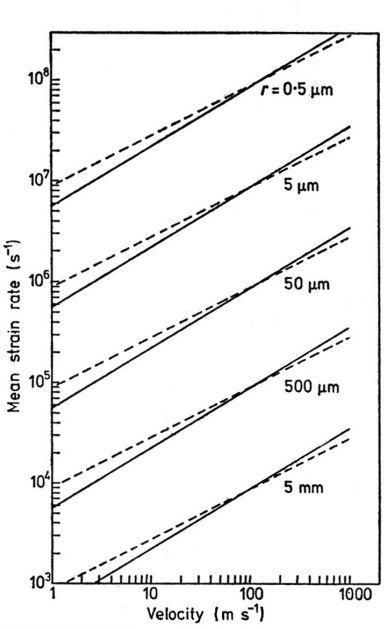


Fig. 1.5 Estimated mean strain rates associated with the impact of spheres on to a steel surface. Solid lines, purely elastic behaviour; broken lines, perfect plastic behaviour [34].

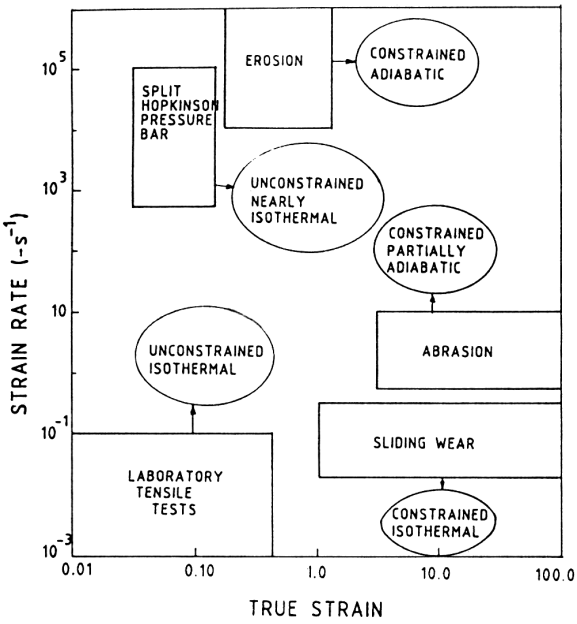


Fig. 1.6 Strain rate-strain regime associated with erosion, tensile test, sliding and abrasion wear. In the same figure, the strain rate-strain regimes pertinent to common tests are also indicated [27].

In general, the high strain rate hardness and stress-strain curves of many metals or alloys are higher than the corresponding low strain rate curves, indicating a positive strain rate sensitivity of target strength (Fig. 1.7). However, the situation is not so straightforward if the work hardening rates under high and low strain rate deformation, characterised by $n_d$ and $n_s$, are compared. As is presented in Table 1.2, such a comparison indicates that, while $n_d$ is higher than $n_s$ for Cu and Ni, $n_d$ and $n_s$ are comparable in Cu-Zn, Cu-Al and Ni-Cr alloy systems. In contrast, $n_d$ is substantially lower than $n_s$ for MA 754, and its dynamic strength coefficient ($K_d$) is actually lower than its static one ($K_s$) (Table 1.2). It should also be noticed that a peak exists at a strain level of about 8% in the dynamic hardness-strain curve of a tempered steel (Fig. 1.7 (c)), and beyond this strain the dynamic hardness starts to decrease with increasing strain. Further studies

indicate that this is a typical feature of dynamic hardness-strain curves of iron, steels, Cu, and other alloy systems, though the strain level at which the curve is peaked can be considerably different. For example, to obtain the peak value of the dynamic hardness of Cu, a strain level of over 65% must be reached [35].

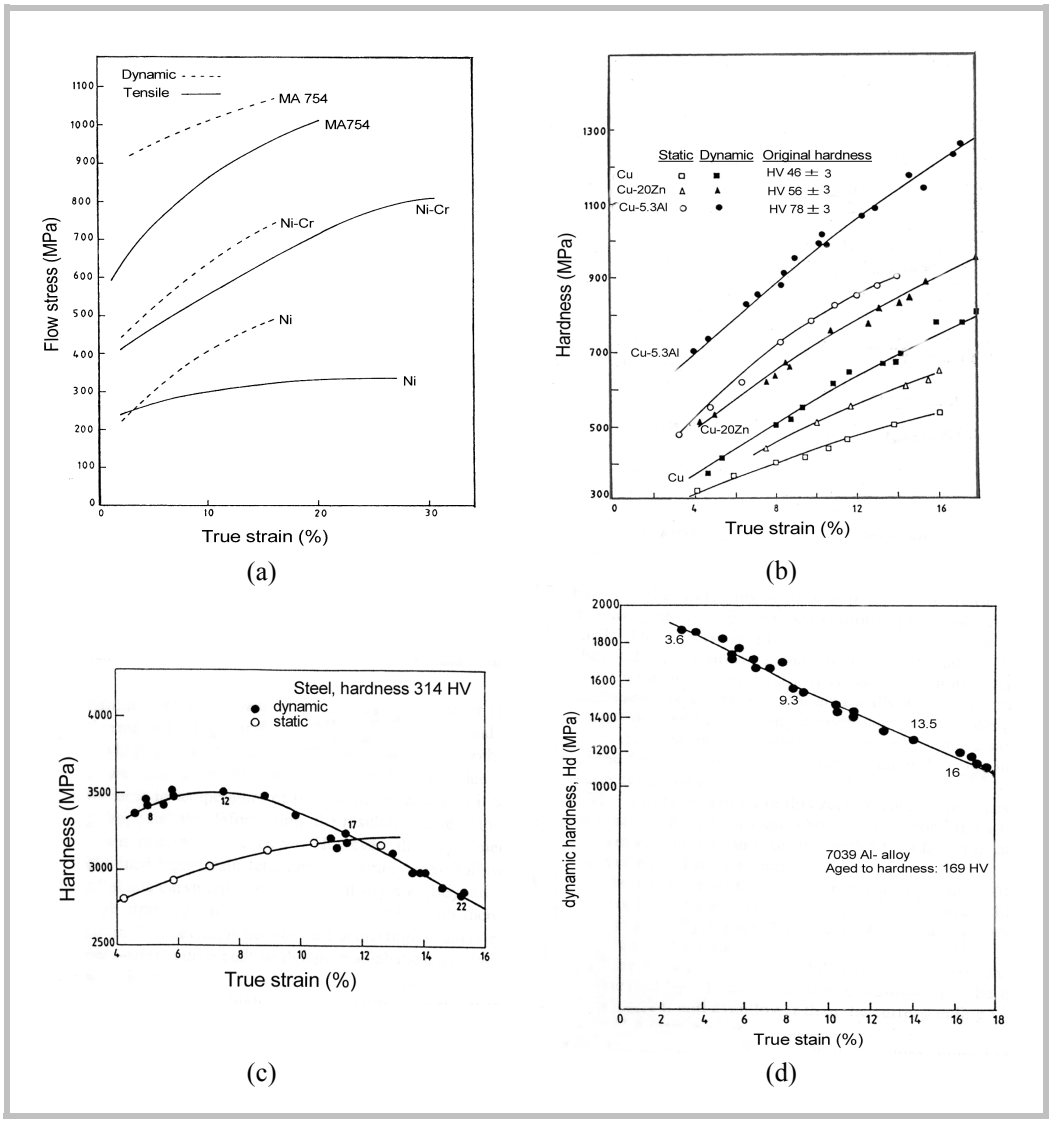


Fig. 1.7 The variation of static and dynamic hardness of metals and alloy systems as a function of average true strain. The numbers alongside the dynamic curves indicate the strain rate (Unit: $10^3$ $s^{-1}$). (a) from Ref. [30]; (b) from Ref. [29]; (c) and (d) from Ref. [27].

Table 1.2 High strain rate effects on strength coefficient and work hardening rate [27]

| **Material** | **Dynamic** | | **Static** | |
|---|---|---|---|---|
| | $K_d$ (MPa) | $n_d$ | $K_s$ (MPa) | $n_s$ |
| Copper | 853 | 0.57 | 447 | 0.42 |
| Cu-20Zn | 735 | 0.41 | 501 | 0.39 |
| Cu-5.3Al | 865 | 0.39 | 681 | 0.45 |
| Nickel | 939 | 0.38 | 490 | 0.20 |
| Ni-20Cr | 1200 | 0.27 | 997 | 0.26 |
| Ma 754 | 1245 | 0.09 | 1474 | 0.23 |

Another characteristic involved in erosion is the large strains, due to the constrained plastic flow conditions as the consequence of the presence of a substantial component of hydrostatic compressive stress. Under the conditions, fracture is inhibited by the elastic constraints of the surrounding material and the high hydrostatic pressure during straining. Similar strain situations can be found in micro-indentation hardness measurement and abrasive wear, in which extremely large strains are achieved.

The characteristics of plastic flow of ductile metals suggest that, under erosion conditions, the target materials experience first strain hardening and then strain softening. As is illustrated in Fig. 1.8, strain softening is the direct consequence of strain localisation. The onset of strain localisation can be expressed as follow [35]. At first, the target material is capable of work hardening so that $d\sigma/d\varepsilon > 0$ at all strains (Fig. 1.8 (a)). Under such conditions, the surface layer of the target is deformed first. However since $d\sigma/d\varepsilon > 0$, this deformation makes this layer harder. Therefore, it is energetically favourable for subsequent deformation to occur in the layers below the first layer since they are undeformed and hence softer. In this manner, the deformation will be spread over a large volume of material underneath the impacting ball (Fig. 1.8 (a)). As the target is strained further, a special stage is reached at a critical strain ($\varepsilon_c$) at which $d\sigma/d\varepsilon = 0$. Under these conditions, any deformation of the near surface layer does not harden it. Thus, it is energetically favourable for all the subsequent deformation beneath the impacting ball to be confined only to the surface layers as demonstrated in Fig. 1.8 (b). This is known as *strain localisation*. In practice, many metallic materials exhibit a finite work hardening capability at low strain, which then progressively decreases with increasing strain. In a more realistic situation, the work hardening capability of a metal under erosion becomes zero at $\varepsilon_c$ and then negative (softening) beyond $\varepsilon_c$ (Fig. 1.8 (c)).

As strain localisation is the unique feature of plastic flow in erosion, it is assumed that the extrusion of lips around the periphery of the craters formed by the impacting particles and the subsequent fracture of these lips is the mechanism of material loss in erosion of ductile metals.

This type of material removal has been observed experimentally in many studies [5, 28, 30-32, and 37-40].

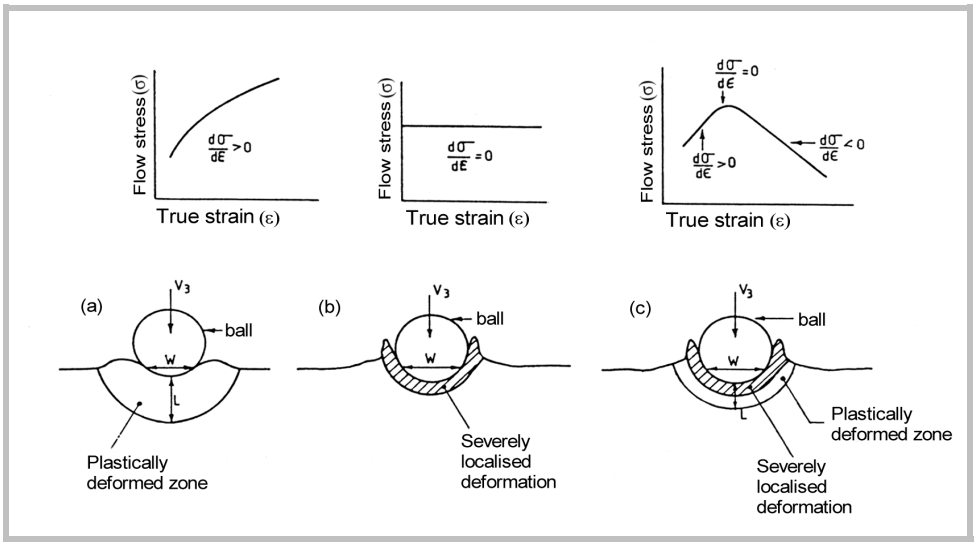


Fig. 1.8 Schematic illustration of the interrelationship between the flow stress-strain behaviour of a material and its tendency to undergo localisation of plastic flow during dynamic indentation [27].

### 1.1.4 Strain Localisation Model: Derivation of the Analytical Formulas

To derive the analytical formulas of the localisation model, it is assumed first that all of the kinetic energy of an incident erosive particle, except for stored elastic energy responsible for its rebound, is dissipated through plastic flow in the eroding material [27]. The plastic flow occurs over an almost hemispherical volume, centred on the contact area between the erodent and the eroding material (Fig. 1.9 (a)). Repeated impacts by numerous erosive particles causes these individual plastic zones to superpose (Fig. 1.9 (b)), resulting in the formation of a uniform plastic zone beneath the eroding surface to a depth $L$ (Fig. 1.9 (c)).

The criterion of the localisation model is that beyond a critical strain ($\varepsilon_c$), the material in the plastic zone (just beneath the impacting erodent) is squeezed out because of strain localisation. The dimensionless erosion rate $E$ can be expressed [26] as

$$E = \frac{L\rho_t}{N_c (4/3)\pi r^3 \rho_e}, \quad \left( \frac{\text{mass loss of target (g)}}{\text{mass of } N_c \text{ erodent particles (g)}} \right) \tag{1-8}$$

where $N_c$ is the critical number of impacts per unit area that causes an accumulation of strain of magnitude $\varepsilon_c$ within the unit volume $L$ (since unit area is considered), $r$ is the radius of the particle (assumed as sphere), $\rho_t$ and $\rho_e$ are the density of the target and the erodent, respectively. If $\Delta\varepsilon_m$ is the average strain induced by an individual impacting particle in the plastic zone, $N_c$ is given by

$$N_c = \frac{\varepsilon_c}{2\pi L^2 \Delta\varepsilon_m \{1-(t+1)/(t+2)\}F(t)} \tag{1-9}$$

where $F$(t) is the function of the strain distribution within the plastic volume. Figure 1.10 is the schematic illustration of the idealised shape of the plastic volume and the strain distribution.

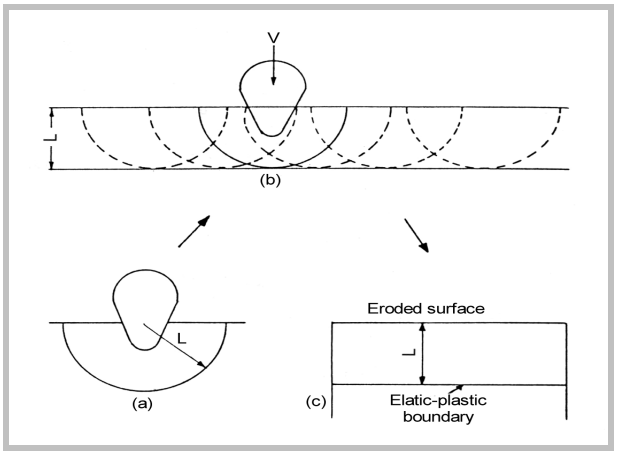


Fig. 1.9. Schematic diagram showing the interrelationship between the individual plastic zone beneath each of the impacting particles and the overall plastic zone formed during erosion involving repeating impacts [41].

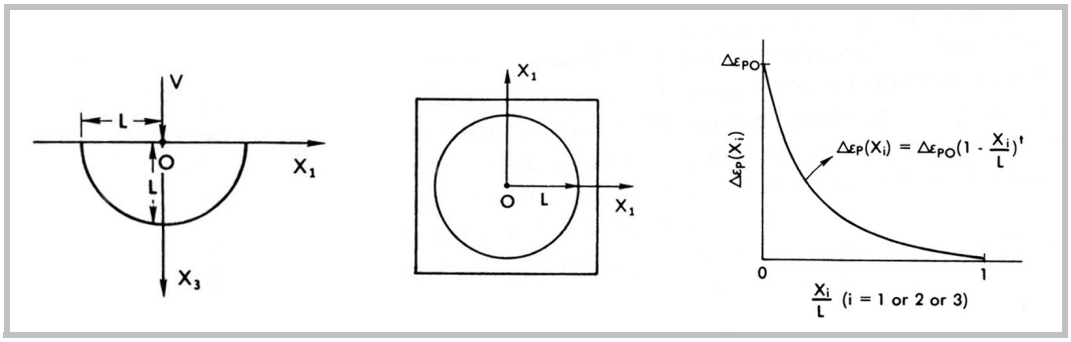


Fig. 1.10. (a), (b) Schematic show of the idealised plastic volume, and (c) the strain distribution within the volume [26].

Substitution of $N_c$ into the expression of $E$ results in the following expression:

$$E = \frac{\pi L^3 \rho_t \Delta\varepsilon_m \{1-(t+1)/(t+2)\} F(t)}{(4/3)\pi r^3 \rho_b \varepsilon_c} \tag{1-10}$$

When $L$, $\varepsilon_c$, and $\Delta\varepsilon_m$ are determined, the erosion rate of a target material can be calculated.

***Determination of $\varepsilon_c$***

To determine $\varepsilon_c$, a constitutive equation containing the physical effects relevant to high strain rates must be established at first. Such an expression can be found [45] as:

$$\sigma_f = \beta G b \sqrt{\rho_t} + \frac{KT}{V^*} \ln \frac{\dot{\varepsilon}}{\dot{\varepsilon}_0} + \frac{B}{\rho_m b^2} \dot{\varepsilon} \tag{1-11}$$

where, $\beta$ is orientation factor ≈ 1.0, $G$ is the shear modulus of the target, $b$ is burgers vector, $\rho_t$ is total dislocation density, $\rho_m$ is mobile dislocation density, $V^*$ is activation volume, $B$ is drag coefficient and $\varepsilon_0$ is a constant.

Each term in equation (2-11) represents different mechanism contributing to the total flow stress ($\sigma_f$). The first term represents the athermal component of flow stress. This stress is determined by the long rang athermal barriers that can be overcome by stress only. The second term corresponds to dislocation motion being controlled by the thermal activation over short-range barriers whose intrinsic free energy is comparable to $KT$. The thermally activated dislocation motion is important in the strain-rate range $10^{-5}$ to $10^3$/s, and predicts a weak strain rate dependence of flow stress, as $\sigma_f \propto ln\varepsilon$. The third term is the intrinsic viscous drag component contributing to the flow stress. At strain-rates higher than $10^3$/s, dislocation becomes transparent to short range barriers, and its velocity is determined solely by the intrinsic viscous resistance exerted by the lattice phonons.

From the above discussion, it follows that the thermal activated component in the flow stress can be neglected, as strain rates over $10^4$/s are usually encountered under erosion conditions. The viscous drag term is important at high strain rate, but low strains associated with single impacts on virgin surfaces. However, since it is inversely related to $\rho_m$, the magnitude of this term decreases with increasing strain, as $\rho_m$ increases with increasing strain. Thus, at high strain rate and large strains featured to stead-state erosion, the 'drag' term can also be neglected and the flow stress becomes

$$\sigma_f = \beta G b \sqrt{\rho_t} \tag{1-12}$$

At high strains, the flow stress can be further expressed in a more practical form [25], as

$$\sigma_f = K(1 - CT)\varepsilon^{n/\varepsilon^S} \qquad \varepsilon > 0.1 \tag{1-13}$$

where $K$ is the strength coefficient, $C$ is the temperature dependence of the shear modulus, $n$ is the high rate strain-hardening exponent, and $S$ is a constant in the range of 0-0.5. The higher the value of $S$, the earlier the flow stress reaches its maximum (Fig. 1.11).

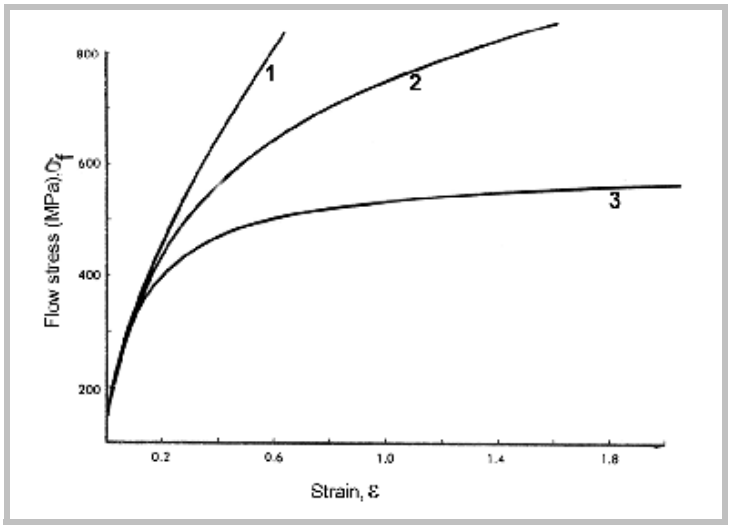


Fig. 1.11. The variation of flow stress with strain at different values of $S$ for annealed copper. Here, $S$ = 0, 0.1 and 0.3 for curve 1, 2 and 3, respectively [26].

From equation (1-13), $\varepsilon_c$ can be derived [26]. First, let the conditions of onset strain localisation be

$$\Delta\sigma = 0 = \left(\frac{\Delta\sigma}{\Delta\varepsilon}\right)_{\varepsilon^\circ, T} \Delta\varepsilon + \left(\frac{\Delta\sigma}{\Delta T}\right)_{\varepsilon^\circ, \varepsilon} \Delta T \tag{1-14}$$

Then, substitute equation (1-13) into equation (1-14).

$$\frac{\varepsilon_c^{\frac{n}{\varepsilon_c^S + s} + 1}}{1 - S \ln \varepsilon_c} = \frac{n \rho t C_p}{3KC} \tag{1-15}$$

Equation (2-15) is solved numerically to obtain the value of $\varepsilon_c$

$$\varepsilon_c = \left( \frac{n_c \rho_t C_p}{3KC} \right)^p \tag{1-16}$$

where $n_c$ is the instantaneous strain-hardening coefficient at the strain of $\varepsilon_c$. The exponent $p$ and $n_c$ can be determined once the values of $K$, $S$ and $n_i$ (the initial strain hardening exponent) are obtained from the complete stress-strain curve of target material [26].

***Mean strain increment $\Delta\varepsilon_m$***

It has been demonstrated [34] that the size of the plastic volume and the microhardness-depth profile are identical under static and dynamic indentation conditions, suggesting the applicability of quasi-static conditions to the dynamic response of target during erosion. This leads to the application of the Tabor relation [45] for estimating the mean strain increment. The Tabor relation is given by

$$\Delta\varepsilon_m \approx 0.1 \frac{W}{r} \tag{1-17}$$

where $W$ is the crater radius created at each impact, and $r$ is the radius of impacting particle. By equating the initial energy of the impacting particle with the energy expended in forming the crater, an expression of $W$ is obtained and then substituted to get $\Delta\varepsilon_m$. The resulting expression of $\Delta\varepsilon_m$ is given [26] by

$$\Delta\varepsilon_m \approx \frac{0.085 v^{1/2} \rho_p^{1/4}}{\sigma_{fav}} \tag{1-18}$$

where $\sigma_{fav}$ is the average flow stress within the deforming volume of the target, $\rho_p$ is the impacting particle density and $v$ is the particle velocity. The average flow stress depends on the average strain $\varepsilon_{av}$ in the deforming volume. Suppose the strain distribution has a form indicated in Figure 1.10 (c), the average strain can be expressed by

$$\varepsilon_{av} = \varepsilon_c / (t+1) \tag{1-19}$$

Hence, $\Delta\varepsilon_m$ is obtained as

$$\Delta\varepsilon_m = \frac{0.085 v^{1/2} \rho_p^{1/4} (t+1)^a}{K^{1/4}(1-CT_c)^{1/4}\varepsilon_c^a} \tag{1-20}$$

where $a = 0.25 n_c (t+1)^s/\varepsilon_c^s$, $T_c \approx T_0 + 0.5\times 3\sigma_{fav}\Delta\varepsilon_{p(av)}/\rho_t C_p$. Here, $T_0$ is the initial temperature of the target, $\Delta\varepsilon_{p(av)}$ is the average strain increment per impact in the plastic zone defined in Figure 1.10.

***Determination of L***

The erosion rate depends strongly on the magnitude of the deforming volume $V_d$ in the target. Referring to equation (1-10) and Figure 1.10, it is noticed that the produce of $\pi L^3$ actually equals to $V_d$. The deforming volume can be obtained by if $L$ is proportional to $W$ ($L = \alpha W$), the crater radius. In fact, $L$ is greater than $W$, since the plastic zone size is larger than the crater volume. Therefore, the deforming volume is proportional to the crater volume $V_c$. The validity of this assumption has been demonstrated in the case of static indentation in many studies for various shapes of indenters such as spheres, cones and pyramids [41-43]. It is also shown that this assumption is valid under dynamic indentation [35]. The resulted expression of $V_d$ is then given as [25]

$$V_d = \alpha V_c = \alpha \frac{(2/3)\pi r^3 \rho_p v^2 (t+1)^{4a}}{K(1-CT_c)\varepsilon_c^{4a}} \tag{1-21}$$

Therefore, $V_d$ is determined instead of $L$. With the expression of $V_d$, $\varepsilon_c$, and $\Delta\varepsilon_m$, the erosion rate can be calculated.

***General expression of erosion rate E***

The general expression of erosion rate can be obtained by substituting equation (1-9), (1-16), (1-20), and (1-21) into equation (1-8). In the case of pure metals, which the literature values of parameter $C$ (temperature dependence of the shear modulus) can be expressed mathematically as [26]

$$C = \frac{5.5\times 10^{-2}}{(T_m - 436)^{0.75}}$$

The resulted expression of erosion rate is obtained as

$$E = \frac{0.085 v^{2.5} \rho_p^{1/4} \rho_t^{1-q} \alpha (t+1)^{5a} \{1-(t+1)/(t+2)\} F(t)}{6.06^q (1-CT_c)^{1.25} \{n_c C_p T_m^{0.75}(1-436/T_m)^{0.75}\}^q K^{1.25-q}} \tag{1-22}$$

In which $q$ and $a$ are given as

$$q = (1+5a)p, \qquad a = \frac{0.25 n_c^{1-ps}(t+1)^s K^{ps}}{\left\{6.06\rho_t C_p T_m^{0.75}(1-436/T_m)^{0.75}\right\}^{ps}}$$

The definition of $s$ and $p$ can be found by referring equation (1-13) and (1-16). To calculate erosion rate from equation (1-22), the parameter $t$ representing the steepness of the strain gradient associated with each impact (Fig. 1.10(c)) is yet to be decided. Considering the determination of $p$ and $s$ which requires the complete stress-strain curve of the target under erosion, equation (1-22) is rather a demonstration of the governing parameters in controlling the erosion loss than a practical formula for convenient use. However, it is nevertheless a significant step since the expression connects the erosion rate to mechanical properties ($K$, $C$) as well as the physical and thermophysical properties of the target and the erodent ($\rho_t$, $\rho_p$, $C_p$, and $T_m$).

It should be mentioned here that the above expression of erosion rate is development under normal impact conditions. However, it is demonstrated [47] that based on the same idea expressions of erosion rate under oblique and intermediate angle impact can be developed. The major difference between the normal and the oblique impact models is that, while a number of impact at the same location are usually required to accumulate the critical strain ($\varepsilon_c$) under normal impact, material is assumed to remove during each impact under oblique impact and steady state erosion. This is because during oblique impact, a significant amount of plastic deformation occurs in the near-surface shear layer due to the tangential frictional force existing at the contact surface between the particle and the eroding material. It is argued [47] that the shear strains accumulated in this layer during each impact are sufficiently high to onset strain localisation.

### 1.1.5 Strain Localisation Model: Prediction of Erosion Rate

From equation (1-10), it follows that erosion rate can be expressed as

$$E \propto \frac{L^3 \Delta\varepsilon_m}{\varepsilon_c} \tag{1-23}$$

with $L$, $\varepsilon_c$ and $\Delta\varepsilon_m$ are defined earlier. Studies [46, 48] have shown that under normal and angular particle impact it is appropriate to assume a constant value in the range from 0.06 to 0.3 for $\Delta\varepsilon_m$. This is based on the results of static indentation tests on metallic materials using pyramid and cone indenters. Such tests indicate that with angular indenters at normal angle,

geometric similarity of the indentation is maintained and thus a constant value of $\Delta\varepsilon_m$ can be assumed. Consequently, under normal impact, $L^3/\varepsilon_c$ should scale in the same manner as the erosion rate, i.e. $E \propto L^3/\varepsilon_c$.

As is showed earlier the plastic zone size $L$ is proportional to the diameter $W$ of the crater formed on the eroded surface. The determination of $L$, therefore, merely requires obtaining an expression of $W$, which can be achieved by equating the energy required for forming the crater with the incident energy of the impacting particle. The resulting expression [43] indicates that $L$ increases with increasing $n$, and decreases with increasing $K$, $K$ and $n$ are the static value of strength coefficient and work hardness exponent of target, respectively.

A practical way of estimating $L$ is by using the microhardness-depth profile illustrated in Fig. 1.12. With this method, $L$ can be determined accurately especially when the test material exhibits a finite strain hardness capability [44, 49]. The microhardness measurement can be carried out using a Vickers' indenter on the sectioned and polished surface at regular intervals and up to a depth deep enough so that the original microstructure is precisely measured. The depth at which the hardness value equals the base value is then defined as the depth of the plastic zone (Fig. 1.12).

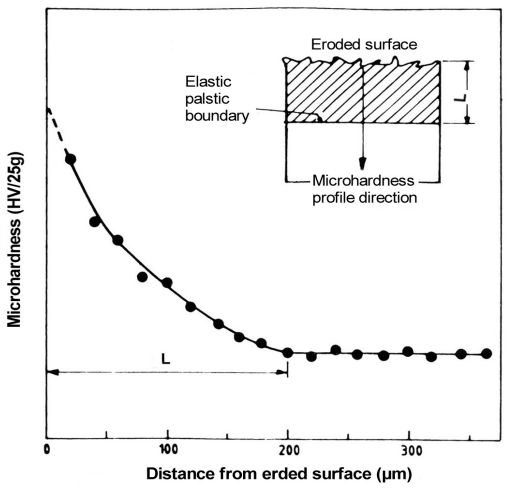


Fig. 1.12. A schematic illustration showing the microhardness-depth technique in determining the plastic zone size $L$ [44].

To estimate $\varepsilon_c$, the following expression has been used [25]:

$$\varepsilon_c = \left( \frac{n\rho_t C_p}{3KC} \right)^{1/n+1} \tag{1-24}$$

Referring to equation (1-15), it can be seen that equation (1-24) is obtained if $S = 0$, i. e. under static deformation conditions. The constant $C$ representing the temperature dependence of the shear modulus of the target is usually inversely proportional to its melting point $T_m$, i.e. $C = C_0/T_m$ [51]. Therefore, equation (1-24) can be expressed as

$$\varepsilon_c = \left( \frac{n\rho C_p T_m}{3KC_0} \right)^{1/n+1} \tag{1-25}$$

Under dynamic deformation conditions, it has been demonstrated [49] that $\varepsilon_c$ can still be estimated from equation (1-25) by simply using the dynamic values of $K$ and $n$. The validity of such a treatment is questionable, as the substitution of dynamic values of $K$ and $n$ into equation (1-15) can not yield equation (1-25), since $S \neq 0$ under dynamic conditions. However, it is shown that the variation of $L^3/\varepsilon_{cd}$ matches the experimentally observed trend in the erosion rates, in which $\varepsilon_{cd}$ is obtained from equation (1-25) by using the dynamic value $K_d$ and $n_d$ [49]. Thus, the critical strain under dynamic conditions becomes

$$\varepsilon_{cd} = \left( \frac{n_d \rho C_p T_m}{3K_d C_0} \right)^{1/n_d+1} \tag{1-26}$$

Though the localisation model is extended satisfactorily to oblique impact conditions [47], the derivation of the analytical expressions of $\varepsilon_c$ and $\Delta\varepsilon_m$ is difficult. This is because the complicity of the stress state, which changes from nearly hydrostatic to nearly pure shear as one approaches the eroded surface from the elastic-plastic boundary. However, it has been shown [51] that on a qualitative basis $\Delta\varepsilon_m$ of per impact will be significantly higher under oblique impact owing to the near-surface shear deformation which occurs under unconstrained conditions, and that $\varepsilon_c$ will be probable lower because of the additional texture-softening effects. Consequently, the term $\Delta\varepsilon_m/\varepsilon_c$ is expected to be substantially higher under oblique impact conditions. On the other hand, $L$ would be lower compared to that under normal impact conditions, since a large amount of deformation is concentrated in the near-surface shear layer. Therefore, the general observation that maximum erosion rate occurs at low impact angles for ductile metals is perhaps due to the fact that the increase of $\Delta\varepsilon_m/\varepsilon_c$ more than offsets the decrease of $L^3$. After all, it has been demonstrated that the magnitude of $L^3$ appears valid in predicting qualitatively the relative erosion rate among a group of materials of identical type [52].

### 1.1.6 Strain Localisation Model: Rationalisation of erosion behaviour of ductile metals

From the foregoing analysis, it follows that the erosion rate of a ductile metal is largely determined by the manner in which the two parameters, $L^3$ and $1/\varepsilon_c$, vary with material properties. Moreover, it is demonstrated [41] that $L$ increases with $n_d$ but decreases with $K_d$, the work hardening exponent and strength coefficient of target under high strain rate conditions. Some of the confusing phenomena in the erosion of ductile metals can be rationalised with the idea of strain localisation.

Firstly, increasing strength can be positive to the erosion resistance for certain ductile metals. In the case of pure metals, which exhibit approximately similar $n$ values (0.3 to 0.45), the parameter $L^3/\varepsilon_c$ is proportional to $1/K_d^{\,n/n+1} T_m^{\,1/n+1}$ (sine $L^3 \propto 1/K_d$ if the influence of $n$ can be ignored [44], and $1/\varepsilon_c \propto (K_d/T_m)^{1/n+1}$, equation 26). As the annealed strength of pure metals correlates with their melting point, the positive effect of increasing strength on erosion resistance is explained. In another case, a martensitic stainless steel (AISI 410SS, HV360) exhibits higher erosion resistance than the other two austenitic stainless steels (AISI 304 and 316, HV 160). This is because, while though $K_d$ values for all the three steels are comparable, 410SS has an extremely low value of $n$, resulting in lower values of $L$ and $\varepsilon_c$ [28]. However, since the erosion rate $E$ is proportional to $L^3$, the decrease in $E$ due to the decrease in $L$ offsets the opposite effect of $\varepsilon_c$.

However, high strength can have an opposite effect on erosion resistance in other cases. For example, in solution strengthened Cu alloy system, adding solutes Zn and Al in Cu do not increase $K_d$ (to a good approximation) but decrease $n_d$ [30]. Thus, $L$ value remains unchanged (since the effect of $K_d$ on $L$ is more dominant than that of $n_d$) while $\varepsilon_c$ decreases on the addition of Zn and Al [27]. The net result is an increase in erosion rate of Cu with solute addition.

Secondly, high ductility does not necessarily lead to good erosion resistance. For example, the ductility of commercially pure Ti is higher than that of the $Ti_3Al$ based alloys, but the alloys exhibit excellent erosion resistance over the pure metal. This is explained by the extremely high work hardening rates and very low $K$ values possessed by the Ti alloys [27]. The combined effect of $n_d$ and $K_d$ results in little change in $L$ but dramatically higher values of $\varepsilon_c$ and, consequently, lowers the erosion rates.

Summarily, the strain localisation model for erosion accounts for the erosion behaviour of a wide range of ductile metals. With the basic ideas from this model, one can understand why material strengthening using a variety of mechanisms often leads to lower erosion resistance for many alloy systems. This, however, presents a difficult situation for material selection in

resisting erosion since, for a monolithic alloy system, there is little room to improve the erosion resistance.

## 1.2 Erosion Behaviour of Brittle Materials

The erosion of brittle materials is a fracture-dominated event, compared to that of the ductile materials in which plastic deformation is prevailing. In the erosion of brittle materials, the force of the impacting particle causes localised cracking at the surface and the cracks, with subsequent impacts, propagate and link eventually together, resulting in material detachment from the surface. Consequently, brittle materials exhibit a very different manner in the variation of erosion loss with impact angle. Erosion loss for brittle materials tends to increase with increasing impact angle with maximum material loss occurring at $90^{o}$, while for ductile materials the erosion loss usually peaks at shallow angles (Fig. 1.13). In the erosion study of brittle materials, the conditions for onset of local fracture due to the contact of hard particles are of particular interest. This is because, if widespread surface fracture does not occur, or if the dominant type of cracking is less effective at removing material, the erosion rate of the brittle material will be much reduced.

Though erosion of brittle materials is a fracture-dominated event, plastic deformation also plays an important role in the process. This is reflected in two phenomena associated with erosion of brittle materials. In the first, it is demonstrated that the `brittle´ angular dependence (Fig. 1.13, curve (b)) is not inevitably seen in brittle materials, as the maximum erosion loss may shift from close to $90^{o}$ to a much lower angle when the erodent size is dramatically reduced [53]. This phenomenon corresponds to a genuine transition from brittle to ductile behaviour. The second phenomenon is the observation of a sharp decrease in erosion rate, or at least a discontinuity of slop in a plot of erosion rate versus impact velocity, when rounded erodent is used (Fig. 1.14). This transition is established because of a change in the extent, and to some degree the nature, of the surface deformation. Above the transition, erosion loss is proceeded in the form of large flaky fragments due to lateral fractures associated with particle impact sites, while below the transition, rounded particles cause no lateral fractures but plastic deformation and, consequently, the erosion loss is considerably lower [54].

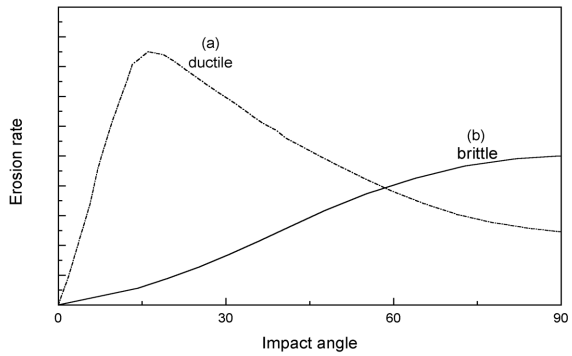


Fig. 1.13 Typical curves showing the different variation of erosion with impact angle: (a) for ductile metal, and (b) for brittle material.

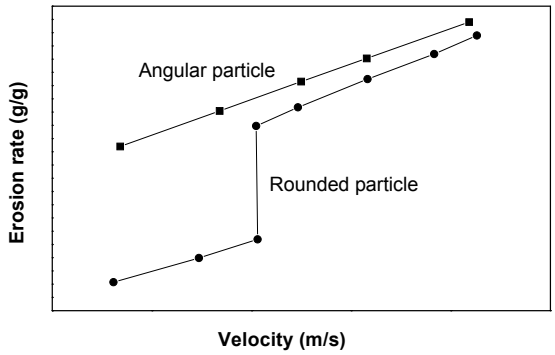


Fig. 1.14 Schematic drawing showing steady-state erosion rate against impact velocity for a brittle material impacted at a shallow angle by a hard particle of two different shapes: angular and rounded.

### 1.2.1 Theories on the Erosion of Brittle Materials

As erosion loss in brittle materials is proceeded by brittle fracture, theories have been developed to account for the crack systems formed at the impact sites. Two types of crack systems are important: *Hertzian crack*, associated with the impact of rounded particles and proceeded only by purely elastic deformation and, *Lateral crack*, caused by the contact of hard angular particles and proceeded by local plastic indentation and deformation of the surface [54]. The lateral crack system is of special interest in the erosion study of brittle materials, for the conditions of its formation are normally encountered in practice.

**Lateral crack**

The erosion of brittle materials by angular particles is viewed by many investigators as an elastic-plastic event, with the plastic deformation at the impact site being the prime driving force for the surface fracture that results in material loss [5, 55, 56]. Detailed examinations of impact sites in brittle materials indicate that a zone of intense plastic deformation that is beneath the

immediate area of contact forms during the impact of hard angular particles [57,58]. Furthermore, residual stresses associated with the plastic zone force small cracks, known as lateral cracks, to grow from the impact site. These cracks initially grow parallel to the target surface, and then curve towards and eventually intersect with the surface, resulting in loss of material.

Two elastic-plastic theories have been developed to explain the erosion of brittle materials by angular particles. Both of the theories are based on the assumption that lateral cracks grow in a quasi-static manner as a result of residual stresses introduced by the impact event. The two theories differ mainly in their assumed dependence of impact load on the kinetic and material parameters affecting to erosion. The theory developed by Evans et al. [56] includes dynamic stress wave effects in the calculation of impact load, $P$. From this theory, the expression for the erosion rate, $W$, can be expressed as

$$W \propto v_0^{3.2} R^{3.7} \rho^{1.3} K_c^{-1.3} H^{-1.25} \tag{1-27}$$

where $v_0$ is the initial particle velocity, $R$ and $\rho$ are the particle radius and density, respectively, $K_c$ is the target toughness and $H$ is the target hardness. The other theory is developed by Wiederhorn and Lawn [59], in which the kinetic energy of the particle is assumed to be absorbed completely by plastic flow when a particle impacts the surface. The following equation for the erosion rate is derived from this theory

$$W \propto v_0^{2.4} R^{3.7} \rho^{1.2} K_c^{-1.3} H^{-0.11} \tag{1-28}$$

It can be seen that the forms of the two theories are similar in that they express the erosion process of brittle materials by a power law dependence of erosion rate ($W$) on both particle ($v_0$, $R$, $\rho$) and target ($K_c$, $H$) properties. However, the exponents for velocity, particle density, and hardness differ in the two theories.

To assess the validity of equations (1-27) and (1-28), the theories are compared with experimental results from literature. In one study [5], it is demonstrated that the two theories are reasonably consistent with the experiment with regard to the exponents for velocity and particle size. While, a serial study on erosion of glass, however, suggests that the theories may well predict the influence of particle size on erosion, the predictions on velocity effect are poor. This is indicated by a wide range of velocity exponent (from 2.4 to 6) obtained in the related studies [60-63]. No systematic investigations have been made of the dependence of target properties $K_c$ and $H$, and the experimental results in the literature are lacking in consistence. In one study [56], it is shown that the dependence of $K_c$ and $H$ is greater than predicted by the theories. A subsequent study [64] has proved this finding and ascribed the greater dependence of $K_c$ and $H$ to

the effect of target microstructure and to the random nature of the particle impact process. The random nature of particle impact states the statistical effect of particle orientation during erosion and the ease with which cracks nucleate upon impact in the target surface. Observations in the study [64] indicate that cracks are often found to arrest during impact resulting in no material loss, unlike the prediction from the theories that once cracks nucleate, they are able to propagate to the target surface. In addition, the interaction of lateral cracks is affected by the grain size of the target. Compared to materials having large grain size, lateral cracks grow more difficulty in materials of fine grain size, since the cracks must interact with more grains during propagation. Investigations [65, 66] have also been carried out on the effect of erodent hardness ($H_p$) on the erosion rate. It has been found that the ratio of erodent to target hardness ($H_p/H_t$) has a stronger influence on the erosion of brittle materials than that of the target toughness, $K_c$, which varies with real crack size.

From the above analysis, it is clear that while both of the models provide a qualitative description of the erosion rate of brittle materials, neither is quantitatively correct. The reason seems to lie in the simplifying assumption made in both theories. It is apparent that the details of the microstructure and material interaction during impact affect the erosion in ways not fully accounted for by the theories.

**Hertzian crack**

A Herzian crack may form when a rounded particle impacts on a flat surface of a brittle solid. The conical-shaped crack (Fig. 1.15) is the result of very localised radial tensile stresses generated adjacent to the area of contact [66-69]. The variation of principal stresses and their trajectories in the surface of the brittle solid in contact with an impacting spherical particle are illustrated in Figure 1.16. Within the contact area (AA), the principal stresses are largely compressive and similar in magnitude, and the resulting large component of hydrostatic pressure within this region appears to preclude the possibility of Hertzian fractures initiating there. Outside AA, the radically directed stress $\sigma_1$ becomes tensile, reaching a maximum value at the circle of contact, and thereafter falls off slowly with radial distance. It is this component of the stress that is mainly responsible for the initiation of Hertzian cracks [68]. The “hoop-stress” $\sigma_2$ has a value equal but opposite to that of $\sigma_1$ outside of AA, and the stress $\sigma_3$ normal to the impacted surface drops to zero. Thus, the stress state outside the contact circle is one of pure shear and, therefore, cone crack initiates just outside the contact area and propagates into the material.

Studies on the erosion damage of brittle materials by rounded particle impact have concentrated on the strength degradation rather than material loss [67, 69, 70, 72]. One reason might be that stress relief through deformation processes such as plasticity and densification is very limited in the erosion by rounded particle, since an elastic contact between the impacting particle and the impacted surface is established. The characteristics of Hertzian crack indicate the elastic contact. In other words, severe strength degradation causing failure of components can

occur as a direct consequence of the formation and development of Hertzian cracks without necessarily involving significant material loss. On the other hand, it has been shown [71, 72] that Hertzian crack does not form until a critical load or velocity is exceeded. In this case, impact of rounded particle below a certain threshold velocity will cause insignificant strength degradation, and no material loss.

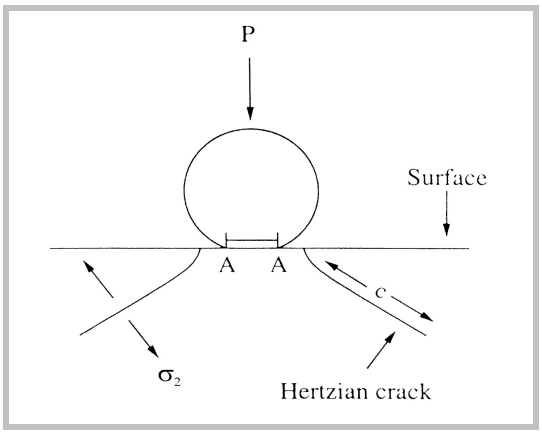


Fig. 1.15 Schematic diagram showing Hertzian crack formation on flat surface of brittle solid upon spherical particle impact.

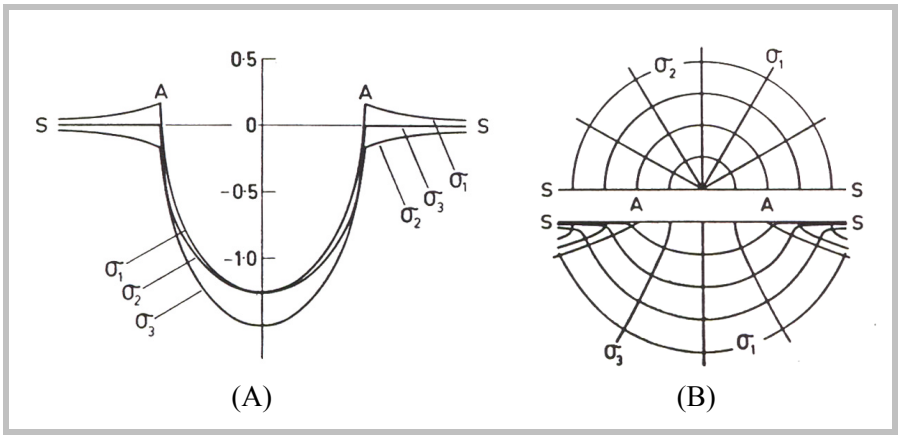


Fig. 1.16 (A) Variation of principal stresses in the surface of a semi-infinite brittle solid (SS) in contact with an impacting spherical particle. The stresses are measured along a line coincident with a diameter (a-a) of the contact circle. (B) Half-surface view (top) and side view (bottom) of stress trajectories in Hertzian stress field [68].

The damage morphology from rounded particle impact often shows more complicated pattern than the idealised Hertzian cone crack. In practice, although Hertzian cone cracks invariably form above the threshold impact, they are usually accompanied by secondary cracking more typical of angular particle impact as well as a general crushing of the surface in the contact area [72]. The main features of the complicated crack system are found similar to those in

comparative static loading test and, therefore, can be represented by a series of microphotographs of statically loading hard sphere on the surface of brittle solid [72]. Figure 1.17 demonstrates that the cracking pattern of polished glass changes from well-defined Hertzian cone cracks (Fig. 1.17, (A) and (B)) at low penetrations to the initiation and development of median and lateral cracks at high penetration (Fig. 1.17, (C) to (E)). On rapid unloading, the cone cracks bend back abruptly toward the surface, and a crushed zone constituted by a network of lateral and other interconnecting cracks is generated (Fig. 1.17, (E)).

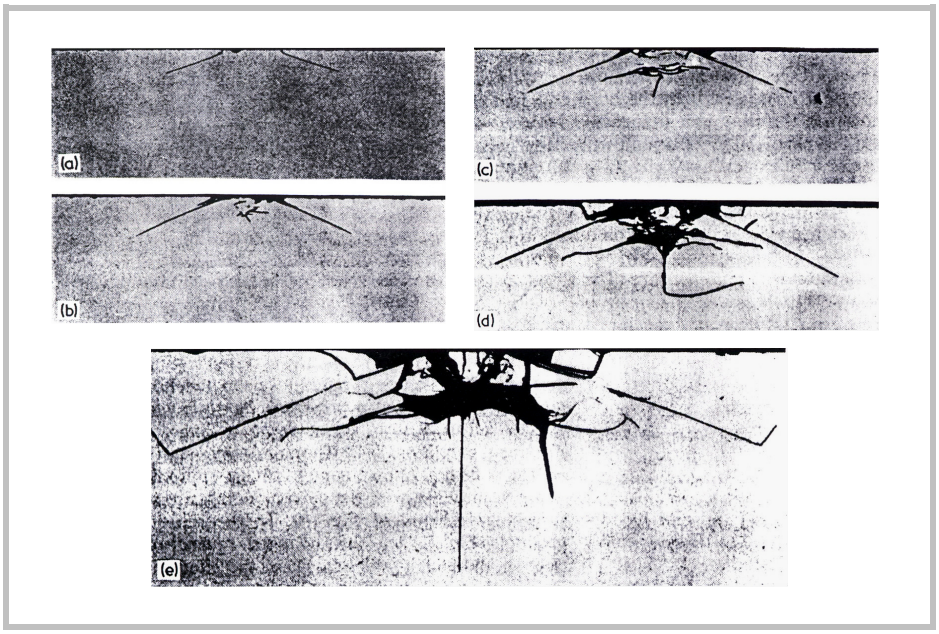


Fig. 1.17. Section-and etch profiles of crack patterns produced in soda-lime glass by WC sphere, r = 0.5 mm, at loads (A) 100N, (B) 140N, (C) 180, (D) 266N and (E) 500N. Width of field in (A) to (D) is 1.5mm, in (E) 2.5mm. Note transformation from characteristic “blunt” to “sharp” indenter patterns with increasing load [73].

This transition of crack pattern suggests that the rounded particle effectively “penetrates” the surface of the target at high velocity, and begins to behave much as an angular particle. The occurrence of the transition depends on the size and velocity of the rounded particle. Therefore, in practice a model of angular particle erosion may offer a satisfactory solution in estimating the erosion loss of brittle materials under the conditions of small particle impact at high speed, regardless of the erodent type involved. The observation of the transition can also be depicted graphically by constructing erosion maps, in which regimes of particle size and impact velocity over which different mechanisms of erosion dominate are presented.

### 1.2.2 Erosion Maps of Brittle Materials

The idea of an erosion map is based on the fact that transitions in wear rate and mechanisms are a common feature in the erosion of brittle materials. In such cases, a relatively small change in erosion conditions, such as impact velocity or size of the erodent, results in significant change in the mechanism of erosion. By selecting appropriate theoretical treatments for the onset of fracture and plastic flow, regimes over which a single erosion mechanism is dominant can be defined and illustrated graphically on `maps´ — plots of particle size against impact velocity [54].

In the case of normal impact of an elastic sphere on to a target material, two transitions may occur: from elastic to plastic deformation and from elastic deformation to Hertzian fracture. It has been found that the elastic-plastic transition is controlled by the target hardness, whereas the fracture transition is determined by the fracture toughness of the target [72]. In the case of normal impact of sharp rigid particle, only one transition, from plastic deformation to lateral fracture, will occur. Here, a modification in the theoretical treatment in determining the threshold velocity is needed when constructing the `map´ to account the situation when the sharp tip of the particle is rounded due to local crushing [74, 75]. The schematic plots in Fig. 1.18 demonstrate the regimes of particle size and normal impact velocity in which Hertzian or lateral cracks and plastic flow will occur in the target. A brief description of the regimes, cited from reference 53, is given below.

In figure 1.18 (A), spherical particles will cause Hertzian crack and plastic flow in the target when critical particle size or critical velocity is reached. In regime I, for small spherical particles and low impact velocities, the deformation is purely elastic, and any erosive wear is expected to be very small, associated with fatigue processes which may eventually lead to crack propagation under cyclic loading. For small particles ($d < d_{0H}$, the threshold value for onset Hertzian crack), an increase in velocity above $V_{*P}$ (critical velocity for initiation of plastic flow) will bring the system into regime II, in which plastic flow of the target occurs and material will be eroded by ductile processes. For particles larger than $d_{0H}$, increasing velocity shifts the system from regime I to regime III, in which erosion occurs by the formation and intersection of Hertzian cone cracks. In regime IV, conditions for both Hertzian fracture and plastic flow are simultaneously satisfied. Under this circumstance erosion will involve both fracture and plastic flow, while lateral fracture rather than Hertzian cracking is actually involved, as it was discussed earlier.

The situation of an angular particle impact is demonstrated in Fig 1.18 (B). In regime I, impinging particles will cause plastic indentation in the target but no lateral cracks, at least not by single impacts. In regime IV, the conditions for lateral crack by all particles, whatever their shape, are satisfied, and the target will be eroded by brittle processes. Regime II represents intermediate conditions, in which angular particles will cause lateral fracture but rounded ones will not. In this case, a strong dependence of erosion mechanism on particle shape would be

expected. Regime III represents a situation in which the conditions for lateral fracture by rounded particles are satisfied while those for angular particles are not. However, it is not clear whether this regime has physical significance, since it may be that for any practical materials the velocity within this regime will be below that needed to cause plastic flow of the target by rounded particles. In other word, no lateral cracks will be generated.

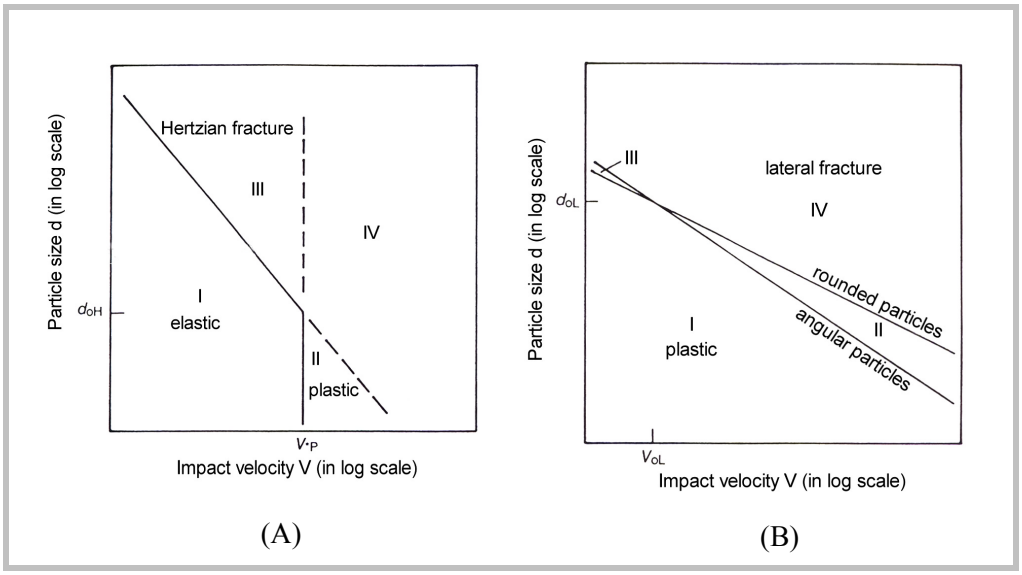


Fig. 1.18. Schematic plot showing regimes of particle size and normal impact velocity in which (A) spherical particles will cause Hertzian cracking and plastic flow, and (B) particles of sharp angular shape and/or rounded tip will cause plastic flow and lateral fracture (after ref. 54).

In summary, the regimes of particle size and impact velocity over which different wear mechanisms dominate provide useful insights into the erosion behaviour of brittle materials. It is acknowledged, however, that several important issues have not been addressed in this approach. For example, the effect of impact angles on the transitions and the influence of microstructural features such as grain size or porosity on the erosion behaviour of the target. In a more fully developed form, such an erosion map would not only indicate the dominant mechanism of erosion for any conditions, but also show contours of constant erosion rate within each regime, allowing absolute values of erosion rate to be predicted.

## 1.3 Erosion Test

In the study of solid particle erosion, it is normal practice to conduct measurements in the field by building up a pilot plant or carry out experiments in the laboratory. Often, it is found that accurate control of all the system variables is extremely difficult in such a plant. Laboratory tests

allow the system variables to be carefully controlled and, therefore, the effects of influencing parameters can be investigated. Among a range of erosion testers available, two kinds of tester, the gas-blast type and centrifugal accelerator type are the most widely used.

Studies have found that the erodent dynamics is an important factor to the erosion damage in solid particle erosion of materials [76-81], and interpretation of erosion results requires a thorough understanding of particle dynamics. It is also believed that the different characteristics of particle dynamics are the main reasons for poor comparability between the values of erosion results using the two erosion testers, even though a similar ranking of materials in terms of erosion resistance can be expected [79].

A short description of the principles of the gas-blast type and centrifugal accelerator type testers is presented below. Both of the testers are involved in the erosion tests in the present study.

### 1.3.1 Centrifugal Accelerator Erosion Tester

The centrifugal accelerator, or rotating disc accelerator erosion tester was originally developed by Kleis in 1956 [82], and subsequently modified by Söderberg et al. [81]. Recently, a new technique for measuring particle velocity in such an erosion tester has been developed [83].

The schematic diagram of the centrifugal accelerator erosion tester is presented in Fig. 1.19. In the diagram, the eroding particles are supplied onto the vibrating feeder through which an even amount of particles is continuously fed into the central hole of a rotating disc. The particles are accelerated through four radial ceramic channels by the centrifugal force and ejected with a velocity defined by the velocity of the disc periphery. The specimen holders are concentrically arranged with the disc on a ring, which is static or can be made to rotate slowly to avoid the effects of circumferential dose variations. The target seats can be individually adjusted to any impact angle.

The most significant advantage of the centrifugal accelerator tester is the capability for simultaneous testing of a number of materials so that identical erosion conditions is ensured. However, anomalies in the test results may occur when using this kind of tester, sometimes making result interpretation a difficult task.

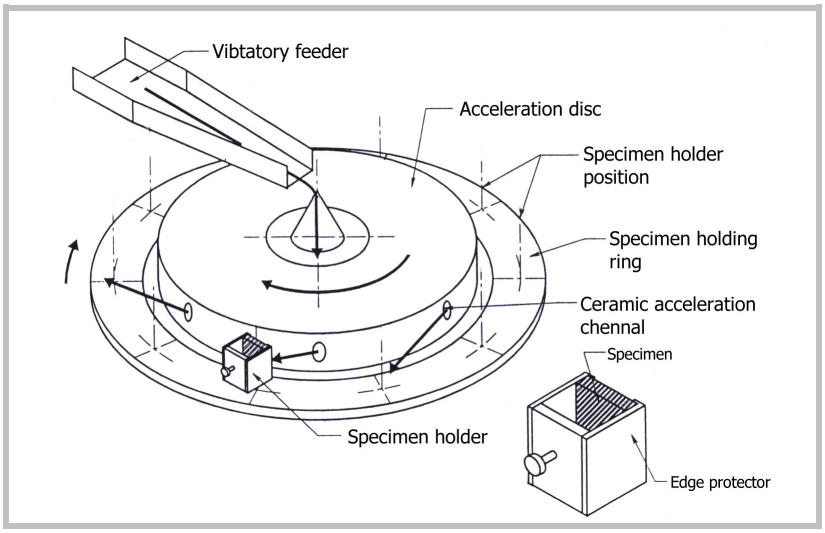


Fig. 1.19. Schematic diagram of the centrifugal accelerator erosion tester showing direction of disc rotation (after refer. 79).

The most significant anomaly with the centrifugal tester is the shape of the erosion rate vs. angle of impact curves. It is commonly accepted that such a curve for a ductile metal will exhibit a peak at approximately $30^o$ (refer to Fig. 1.1 and 1.2). However, recent studies have demonstrated that the peak may not occur within the range of impact angle of $10^o$ – $90^o$, and the erosion rate decreases continuously as the impact angle increases [79, 84, 85]. This is explained by the effect of biased particle spin on impact of differently oriented target surface [79]. In the erosion test using the centrifugal tester, particles may have a biased direction of spin about their centre of gravity when emerging from the rotating disc accelerator. The orientation of the vertically mounted specimen can have a marked effect on the erosion mechanisms. As indicated in Fig. 2.20, the spinning particles will always strike the anti-clockwise rotated target surfaces with topspin but will strike the clockwise rotated targets with backspin. According to Hutchings' theory, a particle with topspin will cause type *I* cutting and material remove by this type of cutting requires multiple impacts and relies predominately on deformation mechanisms [17]. From the same theory, a particle with backspin will cause type *II* cutting on the target surface. Compared to type *I* cutting, type *II* cutting is more aggressive, and the surface material can be removed upon each particle impact. Therefore, the anomaly in the observed curves of erosion rate vs. impact angle can be rationalised. When the specimen holder is clockwise rotated, type *II* cutting will be dominant and the erosion rate is high. Since the efficiency of type *II* cutting in removing material is higher at lower impact angles, the erosion rate increases continuously as the angle is reduced.

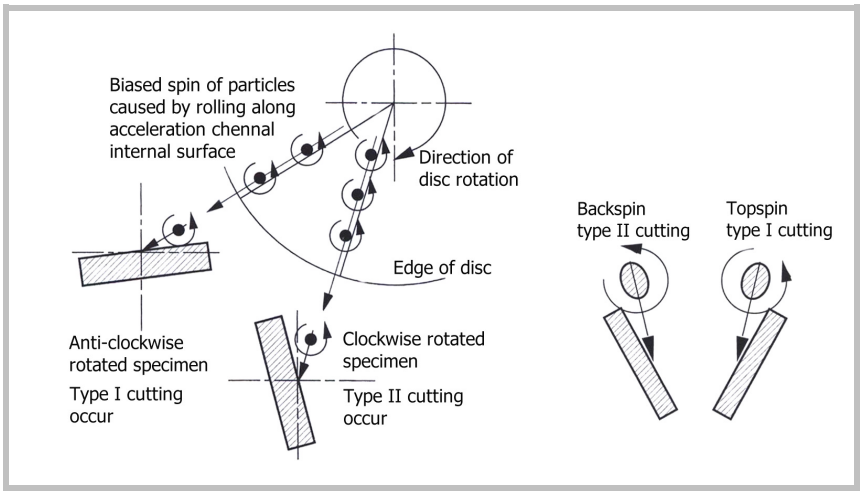


Fig. 1.20. Schematic diagram showing the effects of biased spin of particles on the type of cutting on the target surface (after refer. 79).

The velocity vectors of the impinging particles and hence the erosion process are also affected by dynamic momentum of particles in coupling with the gas and inter-particulate collisions. The dynamic momentum that a particle possesses in coupling with the gas indicates the tendency of particles to travel along the air streamlines after emerging from the accelerating disc and, therefore, missing the targets completely. This effect can be expressed using the following equation [86]:

$$\lambda = \frac{\rho_p d_p^2 U}{18 \mu d} \tag{1-29}$$

where $\lambda$ is the momentum equilibrium constant, $\rho_p$ is the particle density, $d_p$ is the particle diameter, $\mu$ is the fluid dynamic viscosity, $U$ is the gas jet velocity and $d$ is the nozzle diameter. In the study of particle flux divergence on impact of target surface using gas-blast tester, it is found [86] that if $\lambda > 10$ the particles are not affected by the gas flow around them to any degree. Similar particle stream behaviour has been assumed in the centrifugal type tester [79], though no systematic study has been carried out on this type of tester. Usually, the parameters of the erosion testers, for instance the low limit speed $U$ and the nozzle diameter $d$ are so chosen that, for most of the materials in test, the dynamic momentum effect is minimised.

Inter-particulate collisions are thought to be the main reason for the observed divergence of particle stream on impact and the inverse relation between the erosion rate and particle flux. In the vicinity of an eroding surface, there is a region where particles arriving at and departing from the surface can collide. The inter-particulate collisions cause more dispersed transfer of impinging energy to the eroding surface, and as a result, the quantity of erosion damage is

decreased. Meanwhile, the collisions also introduce a spread of speeds and angles of impingement to the eroding beam. Apparently, conditions are more favourable for collisions at high levels of flux. Therefore, the erosion rate may be reduced as the particle flux is increased. However, it should be mentioned that a limiting value of particle concentration in the particle beam or particle flux must be reached before inter-particulate collisions will have a significant role in the erosion process [81, 88].

In summary, the most significant advantage of centrifugal erosion testers is the capacity to test a number of materials simultaneously. On the other hand, this kind of tester suffers a major drawback in that it is difficult to assess the mass of erodent that strikes each target for several reasons. Firstly and principally, not all of the erosive particles will strike the surface of each target or indeed the sum of all the target surfaces, because of equipment setting. Secondly, it is obvious that a target at an oblique angle to the particle beam can not be stroked by as many particles as one that is placed perpendicular to the particle beam. Thirdly, the inter-particulate collision effect will produce a diverging plume of particles striking the target surface. Consequently, some of the particles will miss the affecting area on the target surface that is defined by the diameter of the radial channel. Finally, the effect of the biased particle spin on the erosion mechanism must be considered when interpreting and comparing experimental results.

### 1.3.2 Gas-blast Erosion Tester

In the gas-blast erosion tester, particles are accelerated in a gas stream along a nozzle before leaving the nozzle and striking a target (Fig. 1.21). This type of erosion tester was developed in the early 1960s, and has become popular in most western European countries and in the United States. Equipment of this type of tester is the subject of national standards ASTM G76-89 [87].

The major advantages of this kind of tester are the simple result analysis and short test duration within which the steady-state erosion of target can be reached. Besides, the equipment setting of this type of tester makes it capable of simulating high temperature and corrosive atmosphere erosion conditions that are normally encountered in many industrial processes. The disadvantages of the gas-blast erosion tester, compared to the centrifugal tester, include the difficulties in assessing particle velocity and high probability of adverse gas/particle interactions.

In the gas-blast erosion tester, the particle dose striking a target surface can be accurately determined, since the cross-section area of the particle beam is usually smaller than the target surface area. This makes the result analysis rather straightforward. However, as in the former case, divergence of particle beam will occur. That is, instead of the nominal angle and velocity set for the test, a particle beam with a distribution of trajectories and velocities is experienced, leading to errors in interpretation of the result.

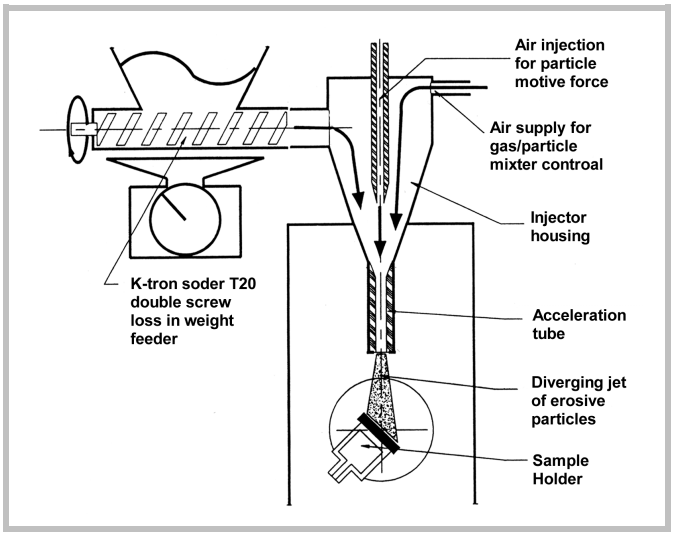


Fig. 1.21. Schematic drawing of the gas-blast type erosion tester (after refer. 79)

Studies [78, 80] have suggested that the divergence of a particle beam on impact of the target depends mainly on the nozzle bore roughness and the nature of the erodent particles, among other factors. As the particles travelling along the nozzle, they undergo many impacts with the wall and, as a result, they are accelerated discontinuously toward the exit. Such impacts would tend to reduce the final velocity below that predicted by the theoretical models. Apparently, the rougher the wall of the nozzle, the wider the exiting velocities of the particles will spread (Fig. 1.22). Furthermore, as the roughness increases, there will be a greater tendency for the particles to leave the nozzle at a wide angle to the axis of the nozzle, thus increasing the size of the stroked area on the target surface.

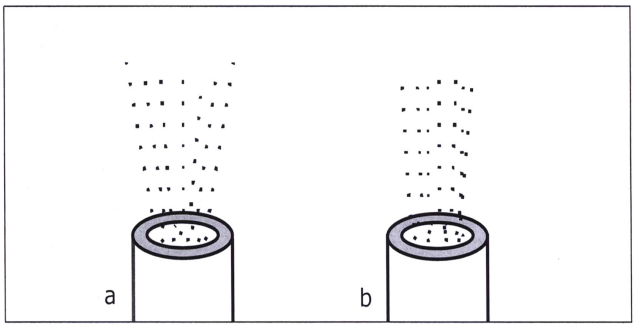


Fig. 1.22. Schematic drawing indicating the tracks of particles on exit from (a) a rough nozzle, and (b) a smooth nozzle.

To summarise the considerations in conducting an erosion test, it should be born in mind that the characteristics of erodent dynamics, along with other factors, are important criteria in

obtaining meaningful test results with good comparability and reproducibility. Because of the lack of the knowledge about particle dynamics, significant different erosion rates on same materials tested under nominally identical conditions are commonly seen in inter-laboratory tests.

## 1.4 High Temperature Oxidation Behaviour of Metals

The study of high temperature oxidation of metals requires a wide range of knowledge. A comprehensive coverage of this subject needs to address a broad range of phenomena, e.g. mass transport through oxide scales, evaporation of oxide or metallic species, the role of mechanical stress in oxidation and the important relationships between alloy composition and microstructure and oxidation.

The intention of this section is to provide a basic understanding of the subject of high temperature oxidation of metals. In order to keep this objective closely to the aim of this study, the high temperature oxidation behaviour of iron, chromium, and nickel, as well as their alloys is introduced. The major part of this section is constructed based on the information from an introductory book on high temperature oxidation of metals by Birks and Meier [89]. It is hoped that the knowledge on the oxidation behaviour of the selected alloys can provide useful insights into the initial state of the studied materials in this study at which erosion-oxidation occurs.

The high temperature oxidation behaviour of ceramics is complicated, involving many physical, chemical and metallurgical processes. However, considering the temperature range concerned in this study, the possible oxide layer on the related ceramics is expected to have little influence on their erosion behaviour. On the other hand, the associated changes in physical and mechanical property of the ceramics are of special interest.

### 1.4.1 Oxidation of Pure Iron, Chromium, and Nickel

Most of the metals in common engineering applications are unstable when exposed to the atmosphere at high temperature, and are subject to deterioration through oxidation. Oxidation of iron, chromium, and nickel represents three types of metal oxidation, which are important to the understanding of oxidation of metal alloys.

**Oxidation of iron**

A multi-layered scale growths on Fe when it oxidises in air at high temperature. Under a temperature below 570$^{o}$C, a two-layered scale is formed. Above 570$^{o}$C, a layer of FeO appears, and the oxide layer sequence in the scale will be FeO, $Fe_3O_4$, and $Fe_2O_3$, with the FeO next to the metal.

The formation of FeO has a significant role in the structure and properties of the overall scale on Fe. As a p-type metal deficit semiconductor that can exist over a wide range of stoichiometry, the FeO phase contains high cation vacancy concentrations and, therefore, the mobility of cations and electrons is extremely high. Consequently, this layer becomes very thick compared to the $Fe_3O_4$ and $Fe_2O_3$ layers. It has been shown that the relative thickness of FeO: $Fe_3O_4$: $Fe_2O_3$ are in the ratio of roughly 95:4:1 at 1000$^o$C [90]. As the thick FeO layer has a porous structure, metal adhesion is lost. Moreover, physical defects are induced in the outer scale by the stresses associated with the rapid growth of the FeO layer and, as a result, the penetration of gas molecules is enhanced. Therefore, exposed to atmosphere at high temperature (> 570$^o$C), Fe deteriorates rapidly and severely through oxidation.

**Oxidation of Chromium**

The oxidation of pure Cr is, in principle, a simple process since a single condensed oxide $Cr_2O_3$ is formed. However, under certain exposure conditions, this $Cr_2C_3$ layer can react with the oxygen forming volatile species causing modifications of the condensed layer.

The two most important modifications are scale thinning by $CrO_3$ evaporation, and scale buckling due to compressive stress development. At high temperature and high oxygen pressures, the formation of gaseous oxide $CrO_3$ becomes significant. The consequence is that the metal consumption is accelerated. This problem, which is more serious in rapidly flowing gases, is one of the major limitations in high temperature applications of $Cr_2O_3$-forming alloys and coatings. The observed scale buckling at high temperature oxidation is believed to be due to the prevailing inward transport of anions along the grain boundary of the polycrystalline $Cr_2O_3$ scale [91]. As a result, compressive stresses are generated during scale formation at the scale-metal interface correlated to the grain boundary region of the polycrystalline $Cr_2O_3$ scale.

**Oxidation of Nickel**

Ni forms only one oxide, NiO, under normal temperature and pressure conditions. NiO is a p-type semiconductor with cation deficit. The mechanism by which oxidation of Ni proceeds is, therefore, expected to involve simply the outward migration of cations and electrons forming a single phase scale. For high purity Ni this single layer scale is compact and adherent, giving rise to good oxidation resistance of Ni at high temperature. However, impurity in Ni can cause a large variation in the rate constant of the scale formation as well as in the scale structure. For example, in Ni with an impurity concentration as low as 0.1%, a fundamental change in the scale structure may occur. In such a case, a two-layered scale, both of NiO, with the out one compact and the inner one porous, is formed [92]. The impurity elements are believed to play a role in the increase in the mobility of cations in NiO. It is, therefore, understandable that in general impure Ni will oxidise more rapidly than pure Ni.

### 1.4.2 Oxidation of Alloys

Alloy oxidation is generally much more complicated than the oxidation of pure metals for many reasons. For example, the metal elements in the alloy will have different affinities to oxygen reflected by the different free energy of formation of the oxides. In addition, metals will have different diffusivities in the alloy, and the metal ions will have different mobility in the oxides. Moreover, the dissolution of oxygen into the alloy may result in internal oxidation — the process by which oxygen diffuses into an alloy, and cause sub-surface precipitation of the oxides of one or more alloy elements. To keep the content of this part close to the aim of this study, the high temperature oxidation of Fe-Cr and Ni-Cr alloy systems are briefed.

**Oxidation of the Ni-Cr alloy system**

In the oxidation of the Ni-Cr alloy system, the content of Cr has a crucial effect on the final scale and thus the oxidation resistance of the alloy. At low Cr contents, internal oxidation of Cr occurs forming $Cr_2O_3$ islands with a matrix of almost pure Ni [92]. The scale consists of an outer layer of NiO with an inner layer, sometimes porous, of NiO containing $NiCr_2O_4$ islands (Fig. 1.23). This inner layer provides additional cation vacancies, thus increasing the mobility of Ni in this region. As a result, together with the extra oxygen tied-up in $Cr_2O_3$ in the internal oxidation zone, a high oxidation rate is observed for the alloy compared to pure Ni.

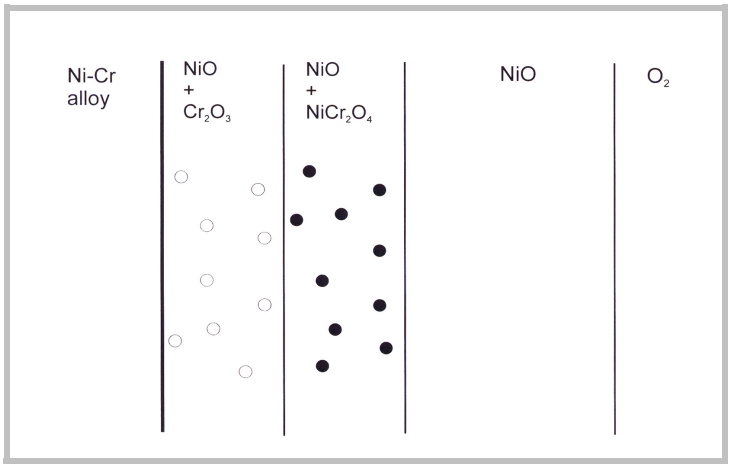


Fig. 1.23 Schematic diagram showing the oxidation morphology of Ni-Cr alloys of low Cr contents (after ref. 89).

As the Cr content of the Ni-Cr alloys is increased, the volume fraction of the $NiCr_2O_4$ similarly increases. This reduces the total flux of Ni through the scale since the $NiCr_2O_4$ islands act as diffusion blocks for outward migration of Ni, and the oxidation rate constant begins to fall. Eventually, as the Cr content increases further, the mode of oxidation changes, which leads to the formation of a complete external scale of $Cr_2O_3$. It is this scale that accounts for the excellent

oxidation resistance of many Ni-Cr alloys. However, there is a critical value of Cr content below which the protective effect of the $Cr_2O_3$ scale may not be permanent, although a complete external scale is formed. This is because the selective oxidation of Cr in forming the $Cr_2O_3$ scale may cause a depletion of Cr in the alloy immediate below the scale. Therefore, any rupture and mechanical damage of the scale will expose a low Cr alloy that will undergo internal oxidation and NiO layer formation with a corresponding high reaction rate. Because of this depletion effect, oxidation resistant alloys based on Ni-Cr system usually contain at least 18-20% Cr.

**Oxidation of the Fe-Cr alloy system**

The most famous alloy group in the Fe-Cr system is stainless steels of which the corrosion resistance of the alloys is directly related to the Cr concentration. For alloys of low Cr contents at high temperature, both Cr-rich and iron oxides form on the surface. The iron oxides, similar to those of pure iron, determine the structure and the properties of the overall scale. With increasing Cr content, some Cr will start to enter the solution of the FeO phase, forming $FeCr_2O_4$ islands, which act as obstacles that block the diffusion of $Fe^{2+}$ ions. As a result, the FeO layer becomes thinner relative to the $Fe_3O_4$ layer. On further increasing the Cr content, a scale of mixed spinel $Fe(Fe,Cr)_2O_4$ is produced, which causes a clear drop in the oxidation rate constant. Finally, when the Cr content is exceeded a critical value, an outer scale of $Cr_2O_3$ is formed reducing the rate constant dramatically. For most Fe-Cr alloys designed for heat resistance, the Cr content must exceed 20% in order to obtain a permanent protective scale. It is noticed that this critical value of Cr is much higher than the one required for an iron based alloy to become stainless for which a Cr content of 11% is usually adequate [93]. This is because a wide range of solid solutions can form by the $Fe_2O_3$ and $Cr_2O_3$ rhombohedral oxides at high temperature. Even with a high level of Cr, iron ions will dissolve in and diffuse rapidly through the $Cr_2O_3$ scale, and eventually an outer layer of fairly pure Fe oxides will result. Therefore, the Fe-Cr system is not a good system to use as the basis of high temperature oxidation resistant alloys for long-term exposures. The stainless steels designed for corrosion resistance to aqueous environments at moderate temperatures should not be regarded as oxidation resistant at high temperatures.

## 1.5 Metal Matrix Composites as Erosion Resistant Material

As it is introduced, erosion is a complex phenomenon, and erosion responses of engineering materials are determined by many factors. For ductile metals, no single mechanical property or a simple combination of a few mechanical properties can be relied on to predict the erosion rate for a given material. On the other hand, thermal-physical properties appear to be important. For brittle materials, it is common for a relatively small change in erosion conditions to result in significant changes in the erosion mechanisms, leading to transitions of erosion rate in large scale. Therefore, there is little room for improving the erosion resistance of a monolithic alloy.

In pursuing the aim of this study, metal matrix composites (MMC) are chosen as the candidate material. The scholarship on MMC suggests that for a given set of erosion conditions, a composite system may offer an opportunity of enhanced erosion resistance. Moreover, composite material can be tailored to suit different erosion environments.

Composites can be defined as material systems combing two or more dispersed phases of different materials, each of which maintains its own distinct volumetric region and properties. The motive for making composites is to create materials with a profile of properties not offered by any of the monolithic components. MMC is one group of this kind of material in which metals are used as the matrix. MMC can be classified into continuous fibre reinforced and discontinuously reinforced composites. In continuously reinforced MMCs, long continuous fibres or filaments are introduced into the metal matrices. In discontinuously reinforced composites, the reinforcements are of three types: whiskers, chopped fibres, or particulate.

In this study, particulate-reinforced MMCs are used in developing the new generation erosion-resistant material. A brief introduction of the properties of MMCs is presented to shed lights on the considerations of the material selection.

### 1.5.1 Mechanical and Physical Properties of MMCs

In general, an MMC system can have several advanced properties over the corresponding matrix alloy, such as: increased strength and stiffness, tailored thermal properties, weight reduction, elevated temperature service, and good radiation and wear resistance. By highlighting the dominant influence parameters that govern the final composite properties, the performance of MMCs can be understood.

**Deformation and failure of MMCs**

The deformation behaviour of a MMC is the result of the interaction between two inherently different classes of materials that are brought together. The matrix material usually shows an elastic-plastic behaviour when undergoing deformation, while the plasticity of the reinforcement is very low. A comprehensive coverage on MMC materials [94] has demonstrated that the mechanics of elastic deformation of MMCs is relatively easy to reveal, as one can treat it through an evaluation of the average stresses in each phase. This evaluation is still valid when dealing with plastic deformation, since the global behaviour of MMCs during the deformation is still governed by the state of average stresses, although in the matrix and reinforcement interfacial area the stress states can be greatly different to the global ones. However, average stress analysis is obviously not an adequate basis for the treatment of fracture and failure of MMCs, which depend on the local processes that control the initiation and propagation of a crack. Besides, the microstructural variables from the fabrication processes and the experimental variables have

exerted much more influence on the failure behaviour of MMCs than on the unreinforced alloys. This imparts more difficulties on the study of failure mechanisms of MMCs.

**Mechanical properties of MMCs**

The observed mechanical behaviour of a given MMC system is the consequence of the combined effects of all the influential factors, such as the properties of the matrix and reinforcement, reinforcement volume fraction, geometry and geometric arrangement, the characteristics of the interfacial area, and the fabrication method.

***Modulus of elasticity*** This property is one of the least sensitive properties to the composite microstructure, though variations in the elastic moduli among the particulate and whisker reinforced MMCs are common. This is mainly attributed to the difficulties in obtaining accurate measurements due to the short proportional regime on the engineering stress-strain curves of MMCs. The major controlling factors on modulus of elasticity are matrix and reinforcement modulus, reinforcement aspect ratio, volume fraction, and alignment [95-97]. In general, an MMC system exhibits higher modulus of elasticity over the monolithic matrix alloy.

***Shear modulus and Poisson's ratio*** The shear modulus and Poisson's ratio of MMCs are the two other properties that are least sensitive to composite microstructure. The major controlling factors on composite shear modulus and Poisson's ratio are similar to those on modulus of elasticity [95-97]. The higher elastic moduli give rise to an enhanced stiffness of MMCs, as the elastic loading is largely shared by the extremely stiff reinforcement. This is critical in the design of many engineering components, as to avoid excessive elastic deflection in service is commonly an important consideration.

***Strength*** The strength of MMCs depends in a complex manner on the composite microstructure [98]. The effects of residual stresses, non-linear and temperature dependent work hardening of the matrix, interface strength and load transfer between reinforcement and matrix, statistical parameters associated with the intrinsic strength of the reinforcement, as well as the variations in microstructural parameters all need to be considered.

The strength of an alloy, expressed in terms of yield (0.2% proof) stress or failure stress, can be substantially enhanced by the addition of reinforcement. However, this is not universally true compared to the stiffness enhancement. For example, when stronger or high work hardening rate matrix are used to make composites, the failure stresses are often lower than the relevant matrix materials. This perhaps comes from the highly constrained plastic flow in the vicinity of reinforcement resulting in premature fracture.

***Fracture Toughness*** The knowledge of fracture mechanics (particularly linear elastic fracture mechanics) has been shown to be inappropriate to characterising the fracture resistance of many MMC systems [99, 100]. This is due to the great sensitivity of composite fracture toughness to

local parameters that can very considerably, often in a poorly controlled manner. The toughness and ductility of MMCs are usually much lower than those of the unreinforced alloys because of the presence of the hard, brittle, and undeformable reinforcing phase.

***Fatigue and Creep Resistance*** Fatigue fracture of MMC materials is governed by the growth of very small microcracks. One of the important parameters concerning fatigue is $\Delta K$, the difference in stress intensity between the maximum and minimum loading. The performance of particulate reinforced MMCs in resisting fatigue cracking depends largely on the magnitude of $\Delta K$, the matrix fracture toughness, the intrinsic strength of the reinforcing particles and their alignment. Explanations of the fatigue behaviour of composites under low $\Delta K$ and high $\Delta K$ loading conditions have been proposed [101-103]. It is somewhat straightforward that the fatigue life of a MMC is lower than that of the corresponding matrix alloy.

On the other hand, the enhanced creep resistance is potentially one of the most significant areas of application of MMCs. Creep is a time-dependent deformation under a constant load. It is then not surprising that the addition of a hard reinforcement embedded in a softer matrix will give rise to an enhanced resistance to this kind of deformation. Moreover, this enhancement can be kept at an elevated temperature in some MMC systems.

**Thermal-physical properties of MMCs**

Thermal conductivity and coefficient of thermal expansion are the two thermal-physical properties that are usually considered in the application of MMCs.

***Thermal Conductivity*** The thermal conductivity of an MMC is a function of matrix and reinforcement thermal conductivity, reinforcement aspect ratio, orientation, and volume fraction. However, unlike elastic moduli, the sensitivity of this composite property to the reinforcement aspect ratio and volume fraction is less profound since the thermal conductivity values of matrix and reinforcement are usually similar. For the same reason the inhomogeneous distribution, or clustering of reinforcement, has little affect on the global thermal conductivity of MMC materials [104]. However, thermal resistance at the matrix/reinforcement interface due to presence of reaction layer or porosity can affect the thermal conductivity of MMCs.

***Coefficient of thermal expansion*** The coefficient of thermal expansion of MMC materials (CTE) is controlled by the volume fraction, aspect ratio, the CTE value and the alignment of the reinforcement. The low CTE of ceramics can be used to tailor the CTE of composites to match that of many different materials. This is useful for microelectronic devices and for components in optical platforms and laser mirrors. It should be mentioned that the composite CTE can also be influenced by the presence of an interfacial reaction layer. Depending upon the interfacial reaction products, either an increase or decrease in composite CTE can be expected.

In summary, MMCs have the potential to offer certain advanced mechanical and thermal-physical properties not achievable through minor additives or microstructure control over the conventional materials. However, uncertainties are high in the prediction of MMC properties, especially for particulate reinforced MMCs, since the phase geometry is usually unknown, the volume fraction of the reinforcement is inaccurate, and the reinforcement shape is difficult to characterise.

### 1.5.2 Corrosion Behaviour of MMC

Studies of the corrosion behaviour of MMCs are sparse compared to those devoted to the mechanical behaviour and processing methods. Metal matrix composites are typically designed for superior mechanical and physical properties, not for resistance to environmental degradation. However, in many cases, for example in marine environments, an adequate corrosion resistance is essential for successful application of MMCs. As a corrosive environment is likely involved during erosion attack, a general knowledge about the corrosion behaviour of MMCs is necessary.

In the study of corrosion of MMCs, the majority of the work has been concentrated on marine corrosion of aluminium-based MMCs [105-111], which are the only type that are widely available. Information on the corrosion behaviour of less common MMCs can also be found, but the volume of the literature is small compared to that related to aluminium-based composites.

From the fundamentals of corrosion engineering, it is apparent that the reinforcing phase in an MMC will act like a cathode to promote dissolution of the matrix alloy which becomes the anode, as it is usually more noble than the matrix materials. However, the actual roles of reinforcement in the corrosion of MMCs are more complicated. Under special conditions, reinforcement can even enhance the corrosion resistance of MMCs to certain types of corrosion attack.

**The role of reinforcement**

The role of reinforcement in the corrosion of MMCs depends on many factors. One of the important factors is the electrical conductivity, as it determines the way that the reinforcing phase contributes to the corrosion of MMCs. An adequate conductivity is necessary for a reinforcement to make a direct contribution to the corrosion of an MMC. In this case, the reinforcing phase is a noble conductor that serves as inert electrodes for proton and oxygen reduction. As a result, the metal matrix that is galvanically coupled to the noble conductor is corroded at an accelerated rate. A good example is the corrosion attack in graphite reinforced aluminium MMCs in chloride containing environments [105, 112, 113]. As a good conductor, the graphite serves as cathodic sites for oxygen or proton reduction causing severe corrosion of the matrix as the anode. Another example is the corrosion of SiC reinforced aluminium composites, one of the most popular MMCs that are widely available. SiC is a semiconductor,

but its conductivity can be somewhat high as the impurity level is increased. Consequently, significant galvanic corrosion between aluminium and SiC in aerated chloride containing environments has been found [113, 114].

The indirect contribution of the reinforcing phase to the corrosion of MMC is also important. The reinforcement can have an indirect effect on the corrosion of MMC in three ways [115]. First, the presence of reinforcement may accelerate the ageing behaviour with ageing precipitates nucleating at interfaces, grain boundaries, and matrix [116-118]. The precipitates enhance the dissolution of the matrix alloy as they are usually noble and then act as extra sites for cathodic reactions. A good example is the preferential attack at the SiC/matrix interface in SiC reinforced aluminium composites due to the presence of the intermetallic precipitate $CuAl_2$ in the vicinity of the SiC phase [106, 110, 111, 115]. Compared to SiC, $CuAl_2$ is a good conductor. Clear evidence has suggested that it is the $CuAl_2$ phase rather than the SiC reinforcement that plays a dominant role in the corrosion process. Second, the formation of reaction products and segregation of alloying elements at or along the reinforcement/matrix interface render the corrosion resistance of MMC lower. It has been reported that the occurrence of $Al_4C_3$ [107] at the interface of carbon fibre/aluminium and the formation of $MgAl_2O_4$ and $Mg_2Al_3$ at the $Al_2O_3$/Mg-added aluminium interface [105, 118] have a detrimental effect on the corrosion of MMC. Third, dislocation pileups near hard ceramic particle/matrix interfaces due to thermal mismatch and/or during fabrication processes may change localised corrosion characteristics. It has been found that in an $Al_2O_3$/Al composite the high dislocation density in composites enhances the solute diffusivity, one of the consequences is the increased possibility of Mg diffusing to the reinforcement/matrix interface, leading to a higher growth rate of detrimental intermetallic compounds [118].

The influence of geometry and geometrical arrangement of reinforcement can also have an influence on the corrosion of an MMC. For example, the reinforcement type can have an effect on the propagation of corrosion pits. It has been observed [107] that in MMC reinforced with continuous fibres, corrosion is generally channelled along the fibres to form pits deep within the material. While, the pit depths are similar to those in the respective unreinforced alloys when same material but in the form of short fibre or particulate is used as the reinforcement [106]. In another study [118], higher corrosion resistance is achieved in a SiC/Al 6013 composite when the homogeneity of the distribution of the reinforcement is improved.

**Corrosion types in MMCs**

Galvanic corrosion is the primary concern regarding the corrosion behaviour of MMCs. This is particularly true when an active metal such as aluminium or magnesium is galvanicly coupled to a noble conductor such as graphite fibre. Pitting also occurs in MMCs, especially in those reinforced with particulate reinforcements having limited conductivity [110, 111, 119]. The presence of reinforcing particles renders the passive film on the composite surface more

vulnerable to breakdown in chloride-containing environments, and pits are found preferentially at the interface regions. Moreover, the oxide film on the surface of an MMC can hardly be repassivated once the localised attack is initiated, as numerous microcrevice sites exist in the interface area.

The stress corrosion cracking (SCC) behaviour of particulate reinforced aluminium composites has also been demonstrated [116, 121, 122]. Though the general trend of MMC materials in against SCC shows a higher susceptibility compared to the equivalent monolithic alloys, some composites exhibit an improved resistance to SCC. This improvement has been attributed to a reduced crack tip strain rate due to the presence of reinforcing phase [123].

In principle, the corrosion behaviour of MMCs can be predicted by using the mixed potential theory. However, the corrosion behaviour of an actual MMC can be different from the predicted one, and this is more likely when the major constituents (matrix and reinforcement) are the only components considered in constructing the mixed electrode diagram [124, 125]. Figure 1.24 presents an example of dissimilarity between the theoretical polarisation curve and the experimental one.

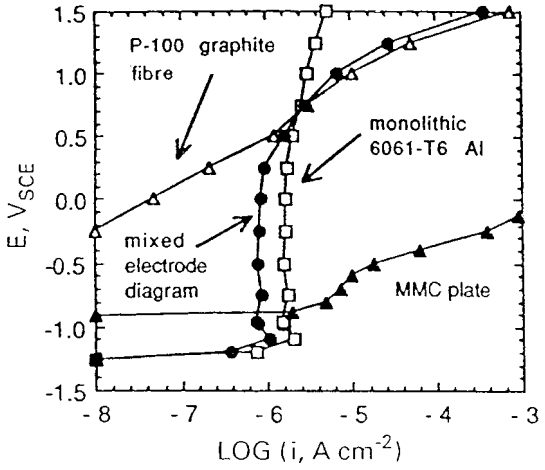


Fig. 1.24 Anodic polarisation curves of graphite fibre, monolithic aluminium, and 50 vol. % graphite/aluminium composite. The dissimilarity between the calculated composite curve and the measured one is dramatic [124].

Microstructural changes and contaminants in the MMC are the main reasons for the dissimilarity in polarisation behaviour. The contamination sources are, for example, segregation of alloying elements, formation of interphases and reaction products between the matrix and the reinforcement, and the processing related impurities. Therefore, although microstructural changes in the matrix of an MMC can be positive in terms of mechanical strengthening, they impart difficulties in predicting the corrosion behaviour of the composite.

### 1.5.3 Abrasive Wear and Erosion Performance of MMCs

Compared to erosion, in which a solid surface is damaged by free-moving particles, abrasion wear is the damage due to hard particles or hard protuberances that are forced against, and move along, a solid surface. The mechanisms by which materials are removed in the abrasion wear are better understood than that in erosion. This, perhaps, is due to the much lower strain rates in the material deformation during abrasion to that in erosion ($10^1$ $s^{-1}$ *vs*. $10^3$~$10^8$ $s^{-1}$, Fig. 1.6) and, therefore, material properties measured under static deformation conditions are more sensible when study abrasion wear. Clear correlation between material properties and abrasion wear resistance has been found in different types of material [126-130]. These properties include hardness, fracture toughness, elastic modulus, yielding strength, microstructure, crystal structure and composition.

**Abrasion wear of MMCs**

Achieving high wear resistance is one of the main motives in the development of MMCs, especially in the case of iron based and particulate reinforced MMCs. It is obvious that hard and well-embedded particles in a soft matrix will give rise to a higher wear resistance to a composite. Parameters affecting the abrasion wear resistance of MMCs include the hardness, shape, size, volume fraction and distribution of the reinforcement, the properties of the matrix, and the interfacial bonding between the two phases.

Reinforcing particles of high hardness value, sufficient fracture toughness and blocky shape are required for a composite to have good abrasion wear resistance. Depending on their hardness ratio to the matrix and the size ratio of the wear grooves to the average diameter of reinforcing particles, the damage patterns of the reinforcement can be different. The reinforcing particles may be dug out, cut off, cracked down, or pulled out from the matrix. High hardness value makes the reinforcing particles harder to cut. Toughness is to resist particle breakage. However, a blocky shape makes crack propagation in the particle more difficult.

Reinforcement volume fraction is another parameter affecting the wear resistance of MMCs. Unless spalling off the reinforcement particles occurs, most studies have shown that the abrasion wear resistance of MMCs increases with the increasing volume fraction of the reinforcement [131-135]. Otherwise, the wear rate of the composite starts to increase with the volume fraction when spalling off reinforcement particles become more evident.

Matrix microstructure has also a significant influence on the abrasion wear resistance of MMCs. The preliminary requirements for a matrix in a composite system are high hardness, good ductility, and large strain hardening capacity. These properties will limit the deformation occurring in the matrix and the extent of brittle fracture of the matrix will be limited and, therefore, the benefit of the embedded phase in resisting the wear attack is utilised.

**Erosion performance of MMCs**

In most of the cases, MMCs exhibit enhanced abrasive and sliding wear resistance over the unreinforced matrix alloys. Their erosion behaviour, however, appears more complicated. Studies of aluminium based composites, carbide-metal composites, and cermets have shown that the erosion resistance of the composites is often lower than that of the matrix alloys [136-141]. Whether the composites perform better than the unreinforced alloys or not depends on a number of parameters in complex manners. External parameters such as impact angle, impact speed, and erodent properties and such internal parameters as the mechanical strength of the matrix, the reinforcement content, and its distribution are all influencing factors on the erosion behaviour of composites.

Composites have showed improved erosion resistance over the unreinforced matrix alloys in shallow-impact-angle conditions [137, 139]. In one study [138], erosion tests are carried out on an Al/short-fibre $Al_2O_3$ composite, with the reinforcement content of 10, 20 and 30 vol%. SiC and $SiO_2$ are the erosive particles, and the impact speed is 65 m/s. The results show that both the composites and the unreinforced alloy exhibit a typical ductile erosion response under shallow-angle impact, and the erosion rates of the composites are lower than those of the unreinforced alloys. It is explained that the short fibre reinforcement has the effect of reducing the severity of the plastic deformation on the impacted surface, and this leads to the reduced erosion rates. When the impact angle increases to $90^o$, voids are found on the composite surfaces, indicating the direct removal of fibres from the surfaces. Under this condition, the composite erosion rates are much higher than those of the unreinforced alloys, since the removal of fibres leaves the surrounding matrix vulnerable to successive attack. Similar erosion behaviour is also found in other studies on particulate-reinforced composites, in which the reinforcements are found beneficial in protecting the surrounding matrix only in shallow-angle and fine erodent impact conditions [139, 142].

The type of erosive particle considerably affects the erosion behaviour of composites. In one study, the composites exhibit lower erosion resistance than that of unreinforced alloy, when eroded by angular SiC particles at all impact angle. However, the same composites show an improved erosion resistance when eroded by less angular $SiO_2$ particles and at a shallow angle [137]. This can be understood by analysing the operating mechanisms controlling the material wastage. In the case of erosion by angular SiC particles, gouging or cutting is the dominant mechanism of material loss, and the scale of the plastic deformation caused by individual particles is much large than the size of the reinforcement. Therefore, the reinforcement provides little resistance to particle penetration. Moreover, the break off of the reinforcement leaves the surrounding matrix more vulnerable to cut. Consequently, the composites show poorer erosion resistance than the unreinforced alloy. On the other hand, the less angular $SiO_2$ particles cause more plowing or less cutting on the sample surface. Since plowing of the surface causes repeated smearing of the deformed matrix alloy over the surface, cracks in the reinforcement and at

reinforcement-matrix interface are not exposed to the free surface for direct attack by subsequent impacts. This leads to a less wastage of the composites under shallow-angle impact.

The influence of erodent particle size on the erosion rate of composites has been found to correspond to the phenomenon of protection or shielding effect. This effect arises when the reinforcing particles in a composite act as a shield for the matrix material behind, while the erosion of the reinforcing particles is negligible [139]. It demonstrates that the occurrence of the shielding effect corresponds to the case where the mean free path ($\lambda$) between the reinforcing particles is much large than the damage (or crater) size produced by a single impact particle (Fig. 1.25). In addition, the presence of protruding particles (the reinforcing phase) on the worn surface can be treated as a sign of the protection effect. The shielding effect is reduced when the erosive particle size changes from fine, to coarse (Fig. 1.26). As a result, the erosion rate of the composites is increased and finally at normal impact angle, the composite resistance becomes poorer than that of the unreinforced matrix.

The argument of shielding effect indicates that it is the erosion responses of the reinforcing phase that determines the erosion behaviour of the composites. Furthermore, it suggests that an increase in erosion resistance of a composite can be expected only when the erosion of the reinforcing phase is in the low rate regime. When erosion of the hard reinforcing phase is in its high rate regime, the contribution of the reinforcement becomes detrimental and erosion resistance of the composite is consequently low. The enhanced strength that the composite may possess has little to do with its erosion performance. Besides, the interfacial bonding between the matrix and reinforcement must be strong so that during erosion the reinforcing particles remain well embedded long enough in the matrix to have the shielding effect functioned.

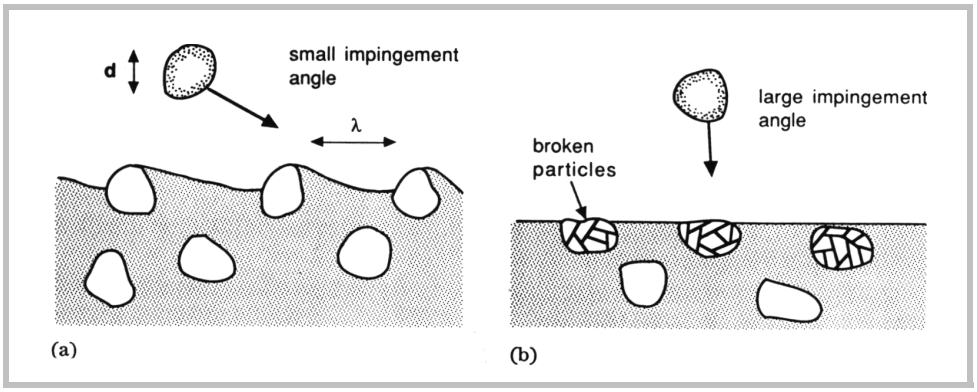


Fig. 1.25 Two basic erosion mechanisms for particulate-reinforced metal matrix. (a) Small impact angle results in a shielding effect because reinforcing particles give rise to protruding particles. (b) Large impact angle causes fracture of reinforcement particles, which eliminates the presence of protruding particles, and the entire surface is then gradual with the same erosion rate for the reinforcing particles and the matrix [139].

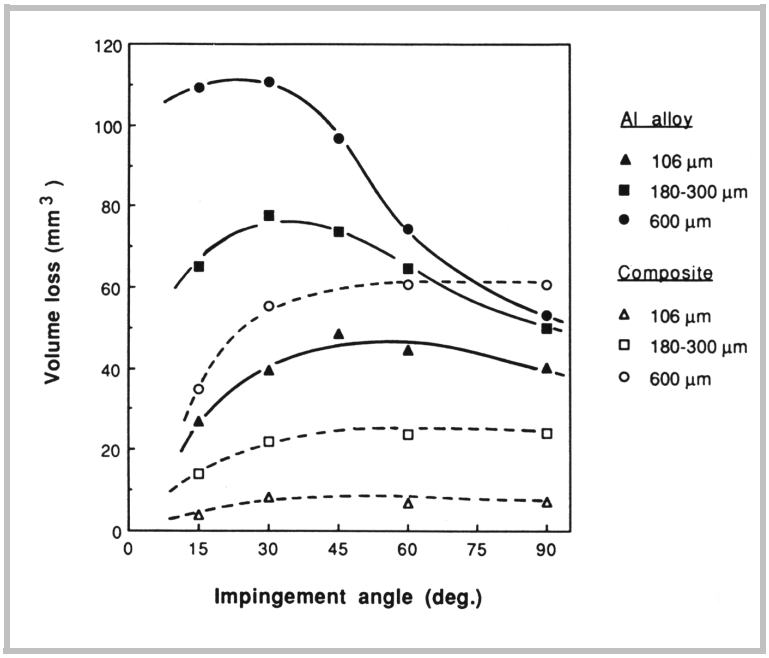


Fig. 1.26 Erosion wear of aluminium alloy (—) and Al/35 vol.% $Al_2O_3$ composites (----) as a function of impact angle of the slurry jet. The composites show higher erosion resistance than that of the alloy at all conditions, except when impacted by coarse erodent and at normal angle [139].

At this point, it becomes clear that a composite system may offer an opportunity of good erosion resistance, while successful design of composite requires good knowledge about the erosion behaviour of the hard reinforcing phase, and the situation of the interfacial bonding between the matrix and the reinforcement.

## 1.6 The Aim of the Study

The aim of the present study is to develop a new generation material for the energy industry. The application conditions require the new materials to have high resistance against solid particle erosion and the synergetic attack of erosion and corrosion, particularly high temperature oxidation. With the new generation materials, the efficiency of energy production processes will be improved.

In addition to the industrial motive, this study is also intended to explore the fundamentals of erosion as a physical phenomenon. It is obvious that a thorough understanding of erosion and erosion-corrosion mechanisms is the precondition to the material development. Moreover, it is expected that the knowledge and the first-hand experiences from laboratory study and field test can provide useful guidelines to the production method of the new materials and to the future study.

# 2. Experiment

The entire experiment was designed closely to service the aim of the study. The specified application conditions required the new materials to perform under high temperature, corrosive, and erosive atmospheres. Solid particle erosion, high temperature oxidation and the synergism of erosion and oxidation were the major reasons for material degradation.

The entire set of experiments can be divided stepwise into three stages: the preliminary stage, the material development stage, and the advanced stage. The tests in the preliminary stage were arranged to provide guiding information for the second stage study. The advanced stage was designed to test the findings and various ideas arising from the second stage. The implementation of the last stage of the tests is, to a large extent, unfinished at the moment. This paper focuses on introducing the experiments and interpreting the results accomplished in the material development stage. However, it should be understood that the major conclusions from the first stage were the important guidelines for the material selection and composite design in the second stage experiments.

## 2.1 Material Selection and Composite Design

Following the arguments in the introductory part, particulate reinforced metal matrix composites were selected to develop the new generation erosion resistant materials. In the material selection, two groups of alloy were considered as the matrices, while hard ceramics in the form of particulate were selected as reinforcements.

### 2.1.1 Selection of Matrix Materials

Two types of alloy, nickel-chromium superalloy and heat resistant steel were selected as the matrices. All of the raw materials were supplied in the form of powder, except one of the heat resistant steels that was in the form of cold-rolled bar.

The selection of the nickel-chromium superalloys was based on the broad usefulness of the alloys. In addition to the excellent resistance to both reducing and oxidising corrosive solutions, the nickel and chromium also work together in resisting oxidation, carbonisation, and other forms of high-temperature deterioration. Moreover, the alloys demonstrate good mechanical stability over a wide range of temperature. At cryogenic temperatures, the alloys do not become brittle. At moderate temperatures, the alloys sustain high level of tensile and fatigue strengths. At high temperatures, the alloys display excellent creep-rupture properties. In this study, two nickel-chromium superalloys — INCONEL 671 and NIMONIC 81 were selected. Under the high

temperature conditions in this study, the oxidation resistance of the selected superalloys was expected to be excellent.

Two heat-resistant steels — AVESTA 253MA and APM9935 were used in this study. AVESTA 253MA is an austenitic high temperature steel that exhibits high oxidation resistance and good weldability. It is used for furnace parts and accessories that are subjected to high temperatures (up to 1100°C) e.g. radiant tubes, sealing plates, and coolers. This grade also lends itself to use in automobile exhaust filter systems and other tubular applications subjected to high temperatures. APM9935 has a major chemical composition close to that of AVESTA 253MA, and hence was expected to behave similarly under the test conditions. The application temperature range of the selected stainless steels suggested that their oxidation resistance under the conditions in this study was sufficient. Since the powder form of AVESTA 253MA was not available, APM9935 in the form of powder was used as the matrix alloy in producing the heat-resistant steel composites. AVESTA 253MA in the form of cold-rolled bar was used as reference material in all of the erosion tests.

In the preliminary stage of study, stainless steel composites were also tested along with the superalloy and heat-resistant steel composites. They were, however, not included in the second stage experiment. From the results of the preliminary stage, it followed that the stainless steel composites experienced a relatively high rate of oxidisation at the temperature concerned. Their low temperature erosion resistance, on the other hand, was comparable and/or worse to that of the superalloy-based composites. In this paper, the erosion performance of the stainless steel composites is presented in the purpose to demonstrate the synergistic effect of erosion and oxidation. Two stainless steels — AISI 316L and DUPLOK 27, were used in the first stage experiment. AISI 316L, one of the most widely used austenitic stainless steel, has an excellent corrosion resistance, especially pitting and crevice resistance in chloride containing aqueous environments. DUPLOK 27 is a duplex stainless steel, and thus has a mixture of ferrite and austenite. As well as good corrosion resistance in aqueous environments, this stainless steel shows higher toughness and yielding strength than does the austenitic grade.

Table 2.1 and 2.2 present the major chemical compositions and selected physical and mechanical properties of the studied materials. The information in the tables is collected from different sources, and thus, should not be treated as absolute values of the materials. The figures in the tables are, therefore, for general reference only.

### 2.1.2 Selection of Reinforcements

Several ceramics in the form of particulate were selected as the reinforcements for the developing composites. High hardness, high elastic modulus, good chemical stability, and availability were the major considerations. Previous experience with metal matrix composites

was also important in the final selection. The major physical and mechanical properties of the ceramic reinforcements are listed in Table 2.3.

Table 2.1 Major chemical compositions of the studied materials

| | % Ni | % Cr | % Fe | % Mo | % Ti | % Cu | % C | % Mn | % Al | % Si |
|---|---|---|---|---|---|---|---|---|---|---|
| INCONEL 671 | Bal. | 48 | | | 0.3 | | 0.04 | | 0.35 | 0.1 |
| NIMONIC 81 | Bal. | 30 | | 0.3 | 1.8 | 0.2 | 0.05 | | 0.90 | 0.5 |
| AISI 316L | 14 | 17 | Bal. | 3.0 | | | 0.02 | 1.3 | | 0.7 |
| DUPLOK 27 | 7.0 | 26 | Bal. | 3.3 | | | 0.02 | 1.0 | | 0.4 |
| AVESTA 253MA | 11 | 21 | Bal. | | 2.4 | | 0.1 | 0.8 | 1.6 | 1.7 |
| APM9935 | 11 | 21 | Bal. | 0.2 | | | 0.09 | 0.6 | | 1.7 |

Table 2.2 Selected physical and mechanical properties of the studied materials

| | Density *g/cm³* | Hardness *HRB* | Young's Modulus *GPa* | Ultimate Tensile Strength *MPa* | CTE linear 20°C *µm/m×°C* | Thermal Conductivity *W/m×K* | Melting Point *°C* |
|---|---|---|---|---|---|---|---|
| INCONEL 671 | 8.02 | 95 | | 862 | 11.8 | | 1350 |
| NIMONIC 81 | 8.06 | | | 1050 | 11.1 | 10.9 | 1340 |
| AISI 316L | 7,92 | max. 95 | 200 | min. 485 | 16.5 | 14 | 1440 |
| DUPLOK 27 | 7.81 | | 200 | 800-1000 | 13.5 | 14 | |
| AVESTA 253MA | 7.80 | 88 | 200 | 600 | 17 | 15 | 1450 |
| APM9935 | 7.75 | 92 | 200 | 650-850 | | 15 | |

Note: The densities of the steels were calculated based on the chemical compositions given in Table 2.1.

Table 2.3 Physical and mechanical properties of the ceramics

| | Density *g/cm³* | Hardness *HVµ* | Young's Modulus *GPa* | CTE *µm/m×°C* | Thermal Conductivity *W/m×k* | Particle shape |
|---|---|---|---|---|---|---|
| $Al_2O_3$ | 3.94 | 3790 | 366 | 8.3 | 28 | Angular |
| $Cr_3C_2$ | 6.66 | 2280 | 380 | 10.3 | 33 | Angular |
| TiC | 4.93 | 3200 | 450 | 7.7 | 34 | Angular |

### 2.1.3 Composite Design and Processing

The composites were processed through a powder metallurgical route in which powders were mixed, filled into capsules, and consolidated. Where the raw powders had a wide range of size distribution, sieving was performed with regard to the considerations in the composite design.

**Particle size determination**

The current knowledge of powder metallurgy suggests that a fine particle size of metal powder is desired in producing high performance materials. Therefore, the matrix powders were sieved to remove coarse particles that were over 106 μm. The particle size of each matrix alloy is presented in Table 2.4.

Table 2.4 Particle size distribution of the matrix alloys

| | INCONEL 671 | NIMONIC 81 | APM 9935 | AISI 316L | DUPLOK 27 |
|---|---|---|---|---|---|
| Particle Size ($\mu m$) | 60 ~ 106 | 60 ~ 106 | < 106 | < 22 | < 106 |

The particle size of reinforcement has more delicate effects on the final properties of composites [94, 99-104, 131], while the size effect on the erosion of composites is little studied. This caused difficulties in the determination of the particle sizes of the reinforcements. Finally, two grades of $Cr_3C_2$, fine and coarse, one fine grade of TiC with narrow distribution range and one coarse grade of $Al_2O_3$ particles, were used to construct the composite materials. The reasons of using two grades of $Cr_3C_2$ are twofold: to improve the homogeneity of the reinforcement in the matrix by narrowing down the size distribution, and to test the effect of reinforcement mean particle size on the overall erosion of the composites. The original size distribution of the $Cr_3C_2$ particles was large enough so that sieving could be performed to obtain two grades of reinforcement from this material. The particle size distributions of the selected reinforcements are given in Table 2.5.

Table 2.5 Particle size distributions of the ceramic reinforcements

| | $Al_2O_3$ | $Cr_3C_2$ | TiC |
|---|---|---|---|
| Fine grade ($\mu m$) | | 10 ~ 45 | 20 ~ 30 |
| Coarse grade ($\mu m$) | 105 ~ 149 | 45 ~ 106 | |

**Composites design**

The volume percentage of reinforcement was the next parameter to be determined in design of the composites. Again, a wide literature survey provided an unclear impression of how the variation of volume percentage of the reinforcement would affect the erosion behaviour of a composite. Therefore, previous studies on abrasive wear of metal matrix composites were referred to in determining the volume percentages of the reinforcements. This was also the case in constructing the composite systems, i.e. which matrix alloy should joint to which ceramic reinforcement, although information from the literature did provide useful insights. It was hoped that the selected range of volume percentage was wide enough to reveal the possible transitions of mechanism in controlling the erosion processes of the composites.

Table 2.6 provides the details of the constitutional variables of the studies composites. The stainless steel composites, tested in the first stage study, are also presented. It should be remembered that more alloys and composite combinations than those presented in Table 2.6 were actually tested or are under testing in the whole study.

Table 2.6 Constitutional variables of the studies composites

| Matrix<br>*M* | Reinforcement<br>*R* | R Volume<br>*Vol. %* | Particle size of R<br>*μm* | Composite<br>*Code* |
|---|---|---|---|---|
| APM 9935 | $Cr_3C_2$ | 10 | 10 ~ 45 | APMCr1F |
| APM 9935 | $Cr_3C_2$ | 20 | 10 ~ 45 | APMCr2F |
| APM 9935 | $Cr_3C_2$ | 30 | 10 ~ 45 | APMCr3F |
| APM 9935 | $Cr_3C_2$ | 10 | 45 ~ 106 | APMCr1C |
| APM 9935 | $Cr_3C_2$ | 20 | 45 ~ 106 | APMCr2C |
| APM 9935 | $Cr_3C_2$ | 30 | 45 ~ 106 | APMCr3C |
| APM 9935 | $Al_2O_3$ | 20 | 105 ~ 149 | APMA2 |
| NIMONIC 81 | $Cr_3C_2$ | 10 | 10 ~ 45 | 81Cr1F |
| NIMONIC 81 | $Cr_3C_2$ | 20 | 10 ~ 45 | 81Cr2F |
| NIMONIC 81 | $Cr_3C_2$ | 30 | 10 ~ 45 | 81Cr3F |
| NIMONIC 81 | $Cr_3C_2$ | 10 | 45 ~ 106 | 81Cr1C |
| NIMONIC 81 | $Cr_3C_2$ | 20 | 45 ~ 106 | 81Cr2C |
| NIMONIC 81 | $Cr_3C_2$ | 30 | 45 ~ 106 | 81Cr3C |
| INCONEL 671 | $Cr_3C_2$ | 20 | 45 ~ 106 | 671Cr2C |
| INCONEL 671 | TiC | 20 | 20 ~ 30 | 671T2 |
| INCONEL 671 | $Al_2O_3$ | 20 | 105 ~ 149 | 671A2 |
| AISI 316L | $Al_2O_3$ | 35 | 105 ~ 149 | 316A35 |
| DUPLOK 27 | $Cr_3C_2$ | 35 | 10 ~ 45 | D27Cr35F |

**Composites processing**

The powder metallurgical route in processing the composites included several steps. First, powders of the matrix alloy and the corresponding reinforcement particles were mixed using a tumble mixer (TURBULA T2C, Maschinenfabrik W. A. Bachofen AG). In the mixing, the powders in the container underwent a complex three-dimensional movement. Optimal mixing was achieved by following an effective mixing procedure [143]. The powder mixtures were then transferred into capsules for consolidation.

Hot isostatic processing (HIPing) was used in the powder consolidation. This technique involves the simultaneous application of a high-pressure gas (usually inert) and an elevated temperature in a specially constructed vessel. Under the conditions of heat and pressure, internal pores and defects within the powder mixture collapse and are welded up. Using this technique, not only full but also uniform densification can be achieved, since the high pressure is developed with gas and thus, is isostatic [144]. The isostatic pressure arises from molecules or atoms of gas colliding with the surface of the object. These colliding atoms have the ability to reach all surfaces of the component, including re-entrant angles, and to act reliably and consistently independent of shape. On average, the numbers of gas atoms moving through unit area, and their velocities, are the same in all directions. Thus, the pressure on every surface of a component is the same and acts in a direction normal to the surface.

Table 2.7 Parameters of HIPing consolidation and heat treatment

| | HIPing* | | | Heat treatment (Solution annealing) | | |
|---|---|---|---|---|---|---|
| Composites | Temp. $^oC$ | Time *hrs* | Pressure *MPa* | Temp. $^o$C | Time hrs | Cooling |
| $Cr_3C_2$/ NIMONIC 81** | 1180 | 3 | 100 | 1100 | 8 | pressed air |
| $Cr_3C_2$/ INCONEL 671 | 1180 | 3 | 100 | 1075 | 1 | pressed air |
| $Cr_3C_2$/ APM 9935 | 1180 | 3 | 100 | 1180 | 1 | water |
| TiC/ INCONEL 671 | 1180 | 3 | 100 | 1075 | 1 | pressed air |
| $Al_2O_3$/ INCONEL 671 | 1180 | 3 | 100 | 1075 | 1 | pressed air |
| $Al_2O_3$/ APM 9935 | 1180 | 3 | 100 | 1075 | 1 | water |

* Diffusion bonding and air cooling.
** Ageing was performed at 700 $^o$C for 16 hours and then followed by pressured air cooling.

The HIPing parameters in this study were determined according to previous experience. After HIPing, the capsules were heat-treated to release the stresses developed during the cooling stage in the HIPing cycle. This was particularly necessary for the composites, since the thermal

mismatch between the matrix and the reinforcing phase could generate high levels of stress and, as a result, internal as well as surface related defects would form in the pre-test samples. For the steel composites, the heat treatment had an additional purpose, which was to ensure the matrices were free of sigma phase, which might precipitate in the high chromium steels in the cooling step of HIPing. Table 2.7 presents the HIPing parameters and the heat treatment procedures used in the second stage of the experiment.

## 2.2 Test Equipment

Two types of erosion tester were used in this study. A centrifugal erosion tester was used in the erosion tests at room temperature, and a gas-blast erosion tester was used for the high temperature erosion-oxidation tests.

### 2.2.1 Centrifugal Erosion Tester

The centrifugal erosion tester used in this study has a typical installation commonly found in the laboratory study of erosion. A vibrating feeder supplies the erosive particles into the central hole of a rotating disc (sand wheel) that has four radial channels made of carbon steel, through which the particles are accelerated by the centrifugal force and ejected with a velocity defined by the velocity of the disc periphery. The specimen holders are concentrically arranged with the disc on a ring that is fixed to the immobile parts of the equipment.

The principle of the tester is illustrated in Fig. 2.1. With this device, fifteen samples can be tested simultaneously at five different angles: $15^{o}$, $30^{o}$, $45^{o}$, $60^{o}$, and $90^{o}$. The speed of the erosive particles can be varied between 40 to 80 m/s. Finally, this device is designed for erosion tests at ambient temperature with dry erosive particles only.

### 2.2.2. Gas-blast Erosion Tester

The principle of the gas-blast test unit is illustrated in Fig. 2.2. The erosive particles are accelerated and heated in a gas stream along an acceleration tube before striking the target surface. During the test run, a computer-controlled unit measures and records data of the temperatures of the test atmosphere and the specimen surface at certain intervals. Simultaneously, the oxygen concentration of the test atmosphere is also monitored. The particle velocity calculations are based on the assumption that particles reach the velocity of the gas stream in the long acceleration tube before impinging on the specimen. The particle dose in the gas stream is controlled by adjusting the particle-feeding rate.

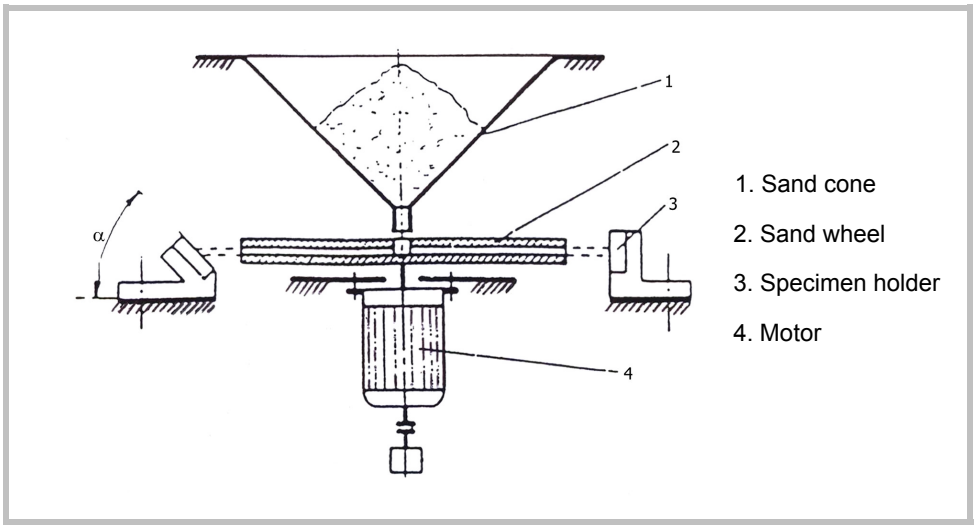


Fig. 2.1 Schematic drawing showing the principle of the centrifugal erosion tester [145].

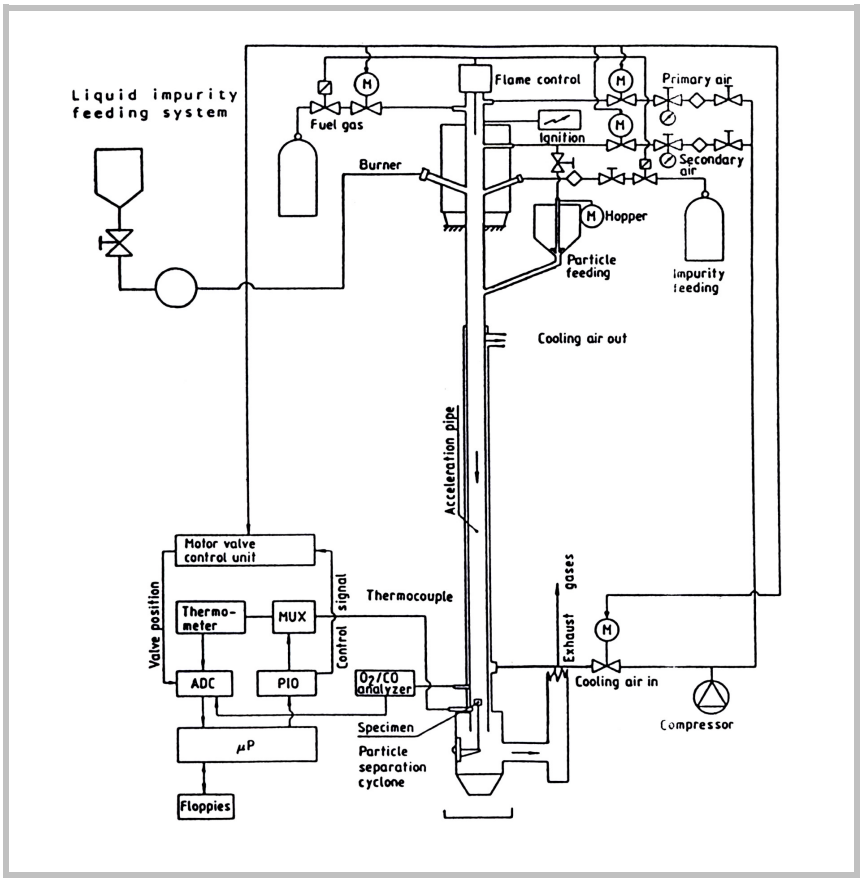


Fig. 2.2 Schematic drawing showing the principle of the gas-blast type of erosion test unit [146].

## 2.3 Implementation of Erosion Tests

The conditions of the erosion tests at room temperature are provided in Table 2.8. Using the centrifugal tester, fifteen specimens (25×15×4 mm) mounted at the same angle to the impinging particles were tested in each round.

Table 2.8 Parameters of the room-temperature erosion tests

| Temperature | Impact angle | Particle speed | Erodent | Particle dose |
|---|---|---|---|---|
| 25°C | 15°/ 30° / 60° | 40 m/s | $SiO_2$ (100 ~600 μm) | 30 kg |

Note: The Particle dose is the amount of erodent consumed in each round of test, and was 10 kg in the first stage and 30 kg in the second stage of tests.

The test conditions of the high temperature erosion-oxidation tests were considered to simulate as faithfully as possible the real application situations. In each set of test, four specimens (20×15×5 mm) of different materials were tested simultaneously. The test parameters are presented in Table 2.9.

Table 2.9 Parameters of the erosion-oxidation tests using the gas-blast tester

| Temperature | Oxygen | Impact angle | Particle feed rate | Particle speed | Erodent | Test duration |
|---|---|---|---|---|---|---|
| 850°C | 10% | 30° / 60° | 2.5 kg/h | 20 m/s | $SiO_2$ (100 ~ 600 μm) | 18 hours |

Note: The nominal particle feed rate was set at 2.5 kg/h, while large variations were experienced in the tests.

As can be seen, the impact angle was the only variable for a given material in the erosion-oxidation tests. However, considering all the combinations of matrices and reinforcements (referring to Table 2.6), the number of specimens to be tested was still large. The funding situation of this study as well as the large amount of work needed in processing the composites set a limit for a given material of only one test at each angle could be implemented. This, however, would leave the validity of the experimental results in doubt, since the repeatability of the data could not be assessed. To cope with this problem, specimens in each set of test were arranged so that there was always a reference sample mounted at the same place in the sample holder (Fig. 2.3). It was hoped that in this way, the relative erosion performance of all the other materials could be evaluated from the erosion data of the reference sample. Multiple specimens of the reference material were tested repeatedly under the nominal test conditions.

Before the tests, the specimens were wet grounded with sandpaper to 1200 grade and the surface areas were carefully measured. All specimens were weighted before and after the tests to an accuracy of 0.1 mg. Although the entire surface areas of the targets were supposed to expose to the impinging particles, it turned out that only part of the surface area of each specimen was actually subjected to the particle impingement in both of the tests (referring to Fig. 2.3 and 2.4). Therefore, the effected surface area of each specimen was measured after the tests to assess the real erosion situation.

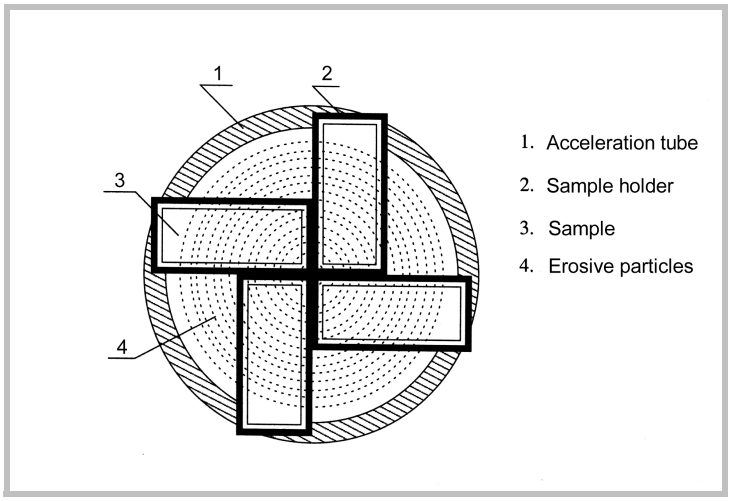


Fig. 2.3 Schematic diagram showing the sample arrangement in the specimen holder.

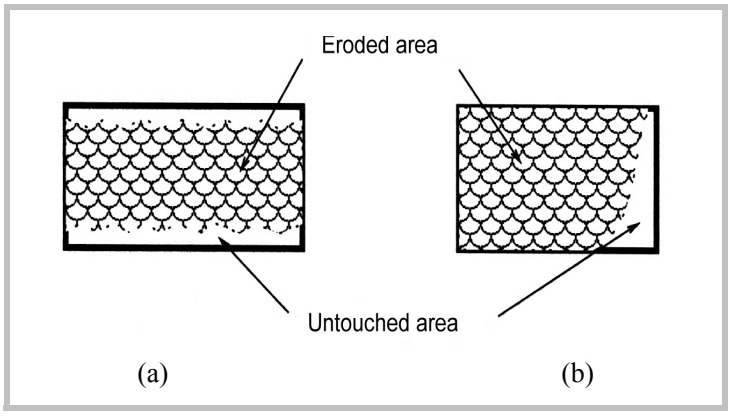


Fig. 2.4 Schematic diagram of sample geometry and typical pattern of the erosion affected surface area. (a) Room temperature erosion test and, (b) high temperature erosion-oxidation test.

# 3. Results

The test results from the second stage experiment include a large amount of data. In this paper, only part of the results will be treated. Furthermore, it will be found that the focus is placed on the interpretation of material behaviour in the tests involving a $60^o$ angle of impact.

However, the trends in the material performance under other impact angles will be mentioned when necessary to assist the discussions and support the conclusions to be reached in this paper. For the same purpose, some test results from the preliminary stage are also demonstrated.

## 3.1 Room Temperature Erosion Test

The composite materials together with the reinforcement-free matrix alloys were tested under three impact angles. For the reasons discussed earlier, the mass of erodent that struck on each target was not assessable since, in each set of tests, an unknown amount of erodent particles inevitably missed the target. Therefore, the erosion performance of the materials is represented in terms of volume removed from per unit surface area, assuming the erosion conditions were identical for each of the fifteen specimens.

The results of the erosion tests at $60^o$ angle of impact are presented in Fig. 3.1. Most of the data in the figure are the average of two measurements from duplicate samples under identical test conditions. It can be seen that the composite materials performed poorer than the reinforcement-free matrix alloys. The exceptional behaviour of the composite APMCr1C is likely an error resulting from, for instance, inappropriate specimen mounting that caused less erosive particles stroke on the surface. Among the composites, the superalloy based ones exhibited better erosion resistance than those based on heat-resistant steel, but the differences were marginal. As to the influence of the reinforcing phase, it showed that the erosion losses tended to increase as the volume percentage of reinforcement was increased, while $Cr_3C_2$ appeared to be less detrimental than the $Al_2O_3$ and TiC to the erosion of the composites.

The erosion behaviour of the stainless steel composites, investigated in the first stage of this study, exhibited a similar trend of material performance (Fig. 3.2). The test conditions were the same except that the particle dose that was 10 kg compared to 30 kg in the second stage of study.

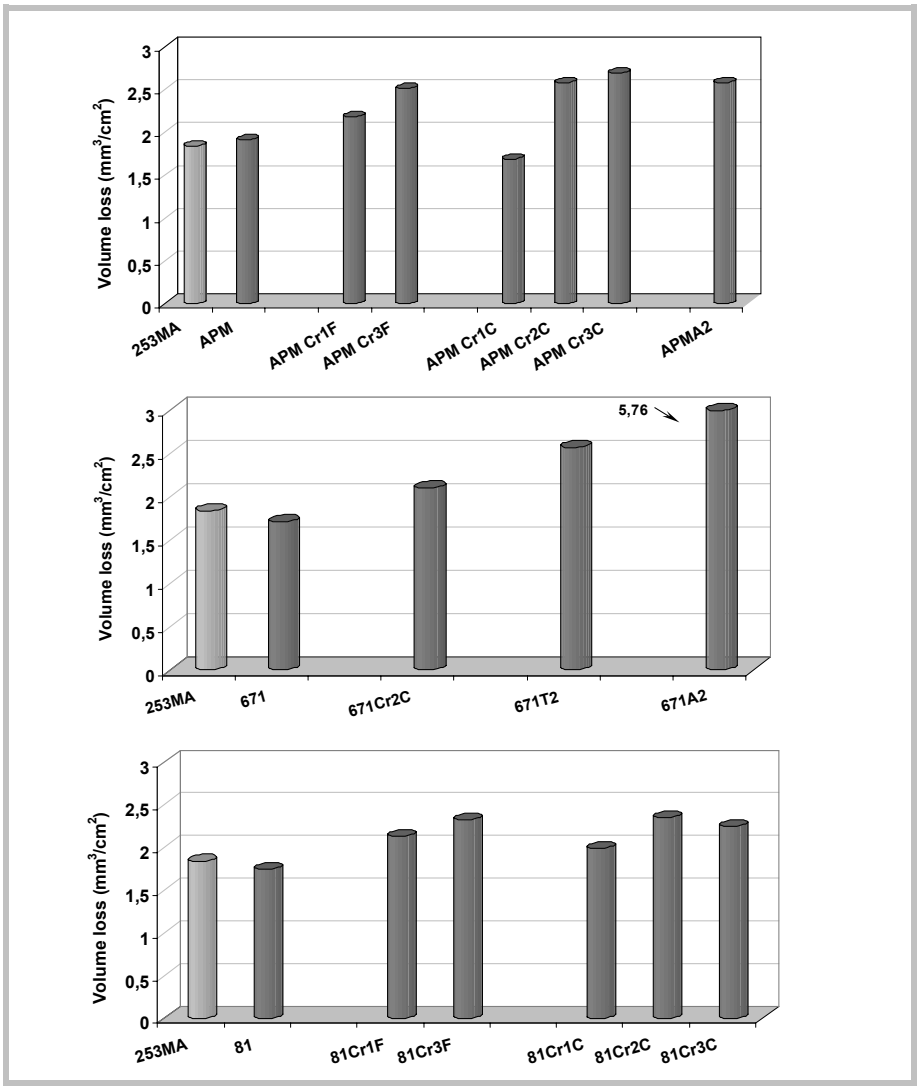


Fig. 3.1 Erosion losses of the studied materials at room temperature (centrifugal tester: $\alpha = 60^{o}$, particle dose = 30 kg).

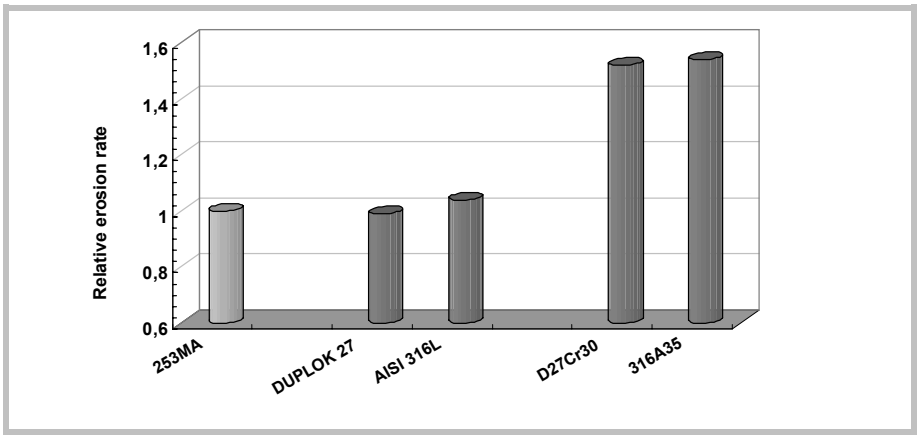


Fig. 3. 2 Relative erosion rate of the stainless steel composites at room temperature. The erosion loss of the reference material — AVESTA 253MA is set as unit (centrifugal tester: $\alpha = 60^{o}$, particle dose = 10 kg).

## 3.2 High Temperature Erosion-oxidation Test

The characteristics of the erosion data indicate a complex situation for analysis of results. This is demonstrated in Fig. 3.3, in which the particle dose and the corresponding erosion losses of the reference samples (AVESTA 253MA) are plotted. The *x*-axis is the set number in which a group of four specimens were tested. The reference samples were mounted at the same position in the specimen holder in each set of tests.

Two things are indicated in Fig. 3.3. First, it is seen that the particle dose was varied dramatically from set to set and, in many cases, was significantly larger than the nominal one — 45 kg, the setting value of the particle-feeding rate multiplying the test duration (Table 2.8). Second, it shows an abnormal relation between the erosion loss and the particle dose in that higher particle dose caused less material to be removed. This appears to conflict with the principle that under steady-state erosion, the erosion rate of a homogeneously structured material should be constant for a given set of test conditions. In other words, per unit erosive particle should remove a constant amount of material in steady state erosion. Only by holding to this principle can erosion rate be evaluated, and the erosion performance of different materials investigated.

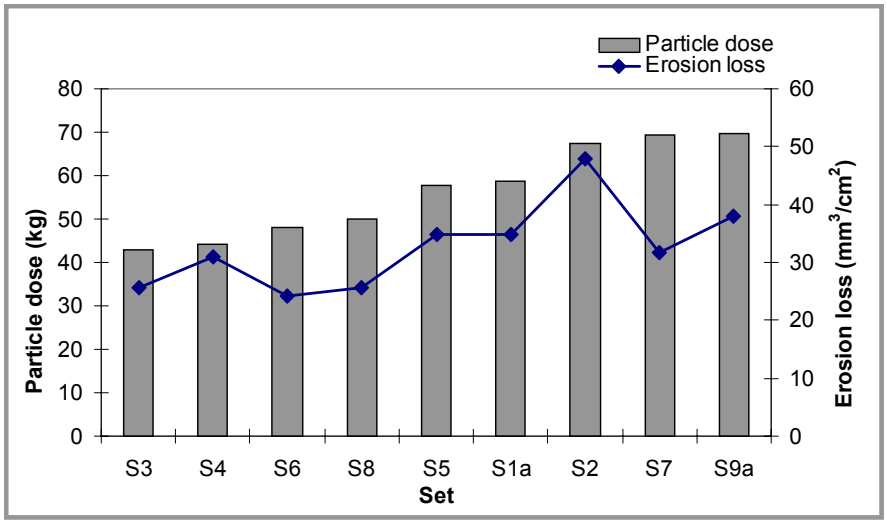


Fig. 3.3 Erosion-oxidation losses *vs*. particle doses for the reference material (gas-blast tester, $\alpha = 60^{o}$).

It has been observed [77, 78, 80] that an increase in particle flux about a threshold level may cause a reduction in the erosion rate in testing with the gas-blast type of tester. This is ascribed to the divergence of the particle beam and the "sheltering effect" of the interactions between the incoming and the rebounding particles. That is, when divergence occurs, instead of the nominal angle and velocity set for the test, a particle beam having a distribution of

trajectories and velocities is actually encountered. Moreover, an effective particle dose rather than the total particle dose should be considered when estimating the erosion rate. Therefore, the results in this study should not be treated as a violation to the principle of steady state erosion since the real erosion conditions appeared varied from set to set.

The experimental data suggest that divergence of particle beam occurred in the tests of the present study. However, the real situation of the divergence as well as the effective particle dose is not assessable. Therefore, the real erosion rates for each material can not be calculated. Under this circumstance, an effort to rationalise the experiment data is made first so that the experimental results are explainable.

### 3.2.1 Data Rationalisation

Fig. 3.3 implies that direct comparisons of erosion performance among materials tested in different sets may incur large errors since the real erosion conditions were varied from set to set. Thus, to make such comparisons valid, the test conditions of each set must be investigated. In doing so, an assumption is made first that if the erosion rates of two specimens of identical material in, for example, set A and set B are similar, the erosion conditions of the two sets are also thought to be similar. This is not necessarily true in a general sense since different combinations of test conditions may yield similar results. However, it was unlikely to be the case in this study since, obviously, the possible combinations in the variation of the test conditions were limited. It went on to assume that the conditional variations in the tests were accounted for mainly by, the variations of one factor, for example, the characteristics of the particle flow during the entire course of the test.

In order to assess the variations in test conditions, the erosion rate of the reference material in each set must be estimated first. This similarly appears to be difficult, as the exact amount of particles striking on the sample surface is unknown. However, since the purpose is to compare the erosion performance among the studied materials, the absolute values of the erosion rate are not necessary. Referring to Fig. 2.3, it appears that it is reasonable to assume that the amount of particles striking each specimen was somewhat under one quarter of the total dose in each set of tests. Using this particle dose for a given set of test, an *apparent erosion rate* for each material in the set can be calculated. Such a calculation for the reference material is presented in Fig. 3.4. It should be remembered that the reference specimen was mounted at the same position in the sample holder in each set of test.

As Fig. 3.4 shows, the apparent erosion rates of the reference samples in Sets 5, 7, 9, 11, and 13 were rather similar, as were the erosion rates of Sets 1 and 3. In Set 15, the erosion rate was much higher. Keeping in mind the assumption made earlier, this suggests that all the test pieces were subjected to roughly three sets of experimental conditions at $60^{o}$ angle of impact

(Table 3.1). However, the occurrence of each set of conditions was not controlled and was therefore random. However, the erosion performance of the materials within each set of conditions (A, B or C) can be directly compared using the values of the *apparent erosion rate*.

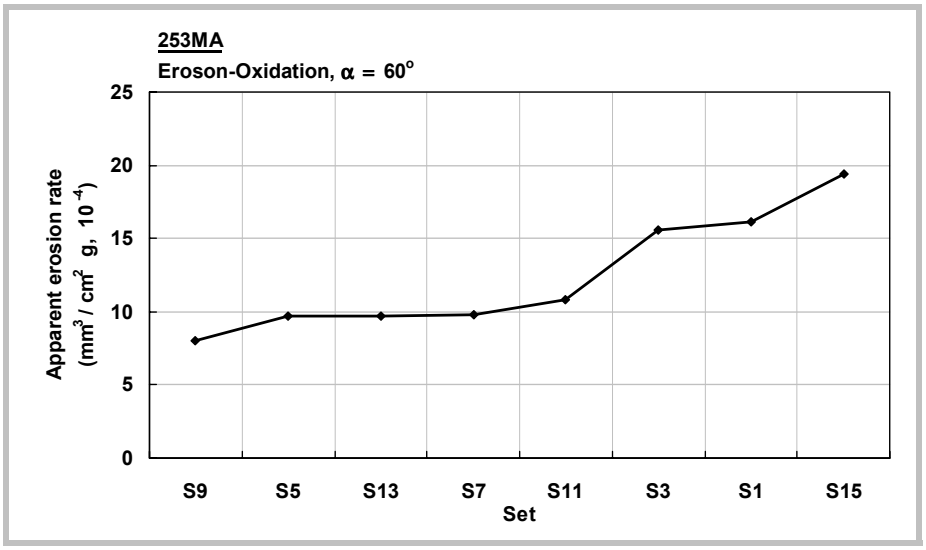


Fig. 3.4 Apparent erosion rate for the reference material, calculated using ¼ of the total dose consumed in the corresponding set (gas-blast tester, $\alpha = 60^{o}$).

Table 3.1 Classification of erosion-oxidation test conditions at $60^{o}$ angle of impact

| | **Condition A** | | | | | **Condition B** | | **Condition C** |
|---|---|---|---|---|---|---|---|---|
| | Set 5 | Set 7 | Set 9 | Set 11 | Set 13 | Set 1 | Set 3 | Set 15 |
| Apparent erosion rate *($mm^3/cm^2$ g, $\times 10^{-4}$)* | 9.7 | 9.8 | 8.0 | 10.8 | 9.7 | 16.1 | 15.6 | 19.4 |

Note: The values of the apparent erosion rates are taken from Fig. 4.4. The real erosion rates are somewhat higher than those given in the table.

The sample positions on the specimen holder were also found to have an observable influence on erosion losses. Notwithstanding the influence of specimen mounting, this suggests that the particle flux over the cross section of the particle beam was uneven. As a result, specimens at different positions (refer to Fig. 2.3) received different doses of erosive particle. To account for the positional effect, a position-factor is introduced. The positional factors are estimated by implementing extra sets of test in which four duplicated test pieces of the reference material were mounted at each of the positions in the sample holder.

The available data in estimating the positional factors include two sets of test at both $60^o$ and $30^o$ angle of impact in the second stage of the experiment, and two sets of test at $60^o$ in the first stage. The results showed that at the position *LL* (Fig. 3.5), the specimen suffered the severest erosion damages. The severity of erosion at the other positions was similar. The positional factors are then estimated and presented in Fig. 3.5. The factor for the position *UL* is set as unit, since this was the position at which the reference sample was mounted in each set of tests. It should be mentioned that the estimation of the positional factors is somewhat conservative, because of insufficient data available. Therefore, it is not realistic to expect the real material performance to be revealed after this treatment. However, this modification does bring the apparent erosion rates of the materials one step closer to the real figures, making the comparisons of material performance more sensible.

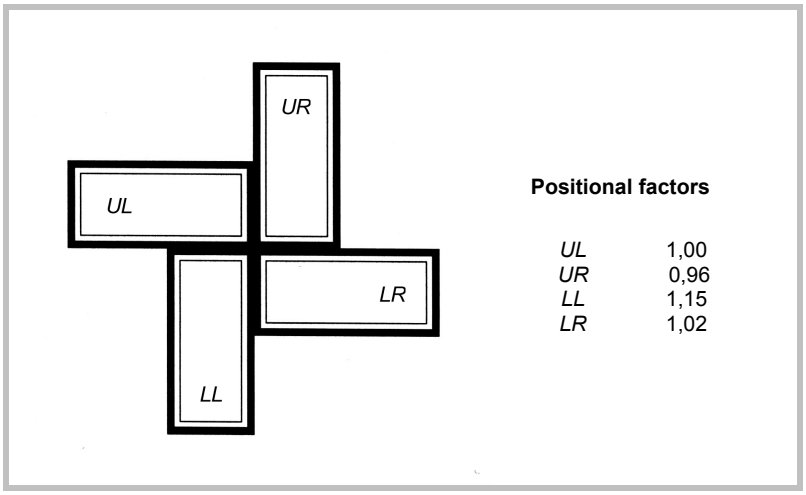


Fig. 3. 5 Positional factors indicating the severity of erosion at different places in the sample holder.

### 3.2.2 Erosion-oxidation Performance of the Studied Materials

The comparisons of erosion performance of the studied materials within each set of conditions (Table 3.1) are presented in Fig. 3.6. It is seen that the trends in the material performance are not consistent for different composite systems.

**$Cr_3C_2$, $Al_2O_3$/APM9935**

The erosion data of the steel-based composites (Fig. 3.6, (a)) indicate that all the reinforcement parameters had clear and significant effects on the erosion performance of the composites. As the volume percentage of the reinforcement increased, the erosion rates of the composites increased too. Composites reinforced with coarse $Cr_3C_2$ particles were overperformed those with fine $Cr_3C_2$ particles. With the exception of the composite with $Al_2O_3$ reinforcement, the overall erosion resistance of the composites was inferior to that of the reinforcement-free matrix alloy.

The good erosion resistance from the $Al_2O_3$ reinforced composites contrast with the results of the room temperature erosion tests, in which the $Al_2O_3$/steel composites were among the worst performing materials (Fig. 3.1 and 3.2).

**$Cr_3C_2$/NIMONIC 81**

Because of the uncontrollable variations of in the test conditions, this composite system was subjected to two sets of conditions (Condition A and B). The data show that the erosion rates of the composites scaled inversely to the volume percentage of the reinforcements, contrary to the behaviour of the steel composites (Fig. 3.6 (c) and (d) vs. (a)). The influence of reinforcement particle size to the erosion rate of the composites was also contrary to the trend of the steel composites. In this case, the composites reinforced with fine $Cr_3C_2$ particles seemed to perform better than those with the coarse ones.

**$Cr_3C_2$, TiC, $Al_2O_3$/INCONEL 671**

The results show again that the composite with $Al_2O_3$ reinforcement performed the best in resisting the erosion attack (Fig. 3.6, (c)). In addition, it appears that under the testing conditions TiC was not a good choice as the reinforcement in developing the erosion-oxidation resistant composites.

In comparison, the performance of the stainless steel composites is presented in Fig. 3.7. The tests were accomplished in the first stage study under similar conditions. It is seen that the relative erosion rate of the reinforcement-free stainless steel was significantly higher than the superalloy and the reference material. To the corresponding composites, the erosion rate was even higher. The data in the figure were rationalised following the same ideas.

## 3.3 Determination of Plastic Zone Size *L*

As introduced in the introduction part, the strain localisation theory is an attractive model in explaining the erosion phenomena of ductile materials. According to the theory, for a ductile material under steady state erosion, a uniform plastic zone beneath the eroding surface to a depth $L$ is formed (Fig. 1.12). Moreover, it demonstrates that the magnitude of $L^3$ appears valid in predicting qualitatively the relative erosion rate among a group of materials of same type [52].

Referring to Fig. 1.12, $L$ is determined using a practical method. The plastic zone size is defined as the depth at which the microhardness value equals the base value. In this study, the plastic zone analysis is carried out only on selected materials tested at a $60^o$ angle of impact.

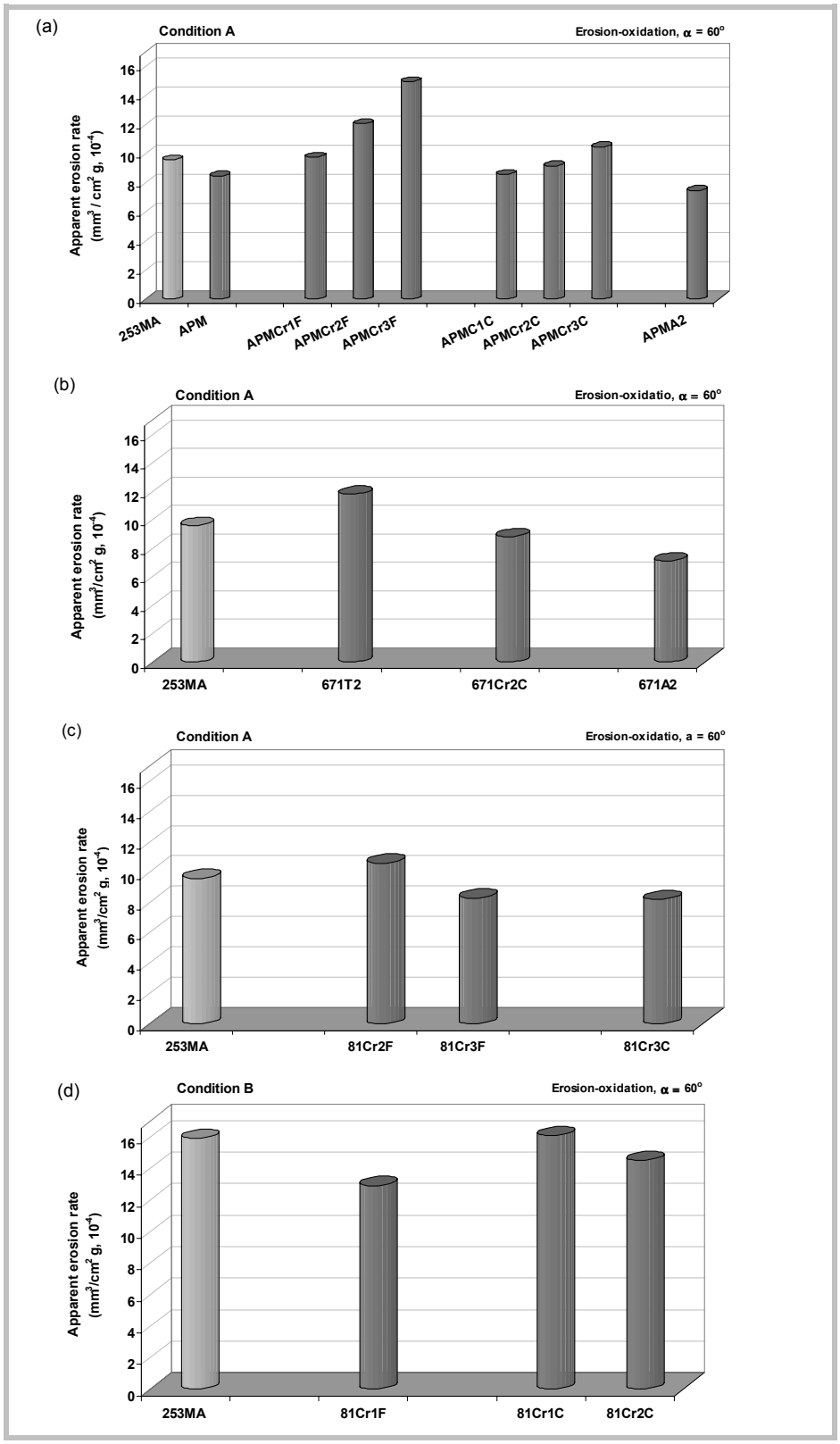


Fig. 3.6 Erosion losses of the studied materials in the high temperature erosion-oxidation test (gas-blast tester: 850°C, $v$ = 20 m/s, $\alpha = 60^{o}$,).

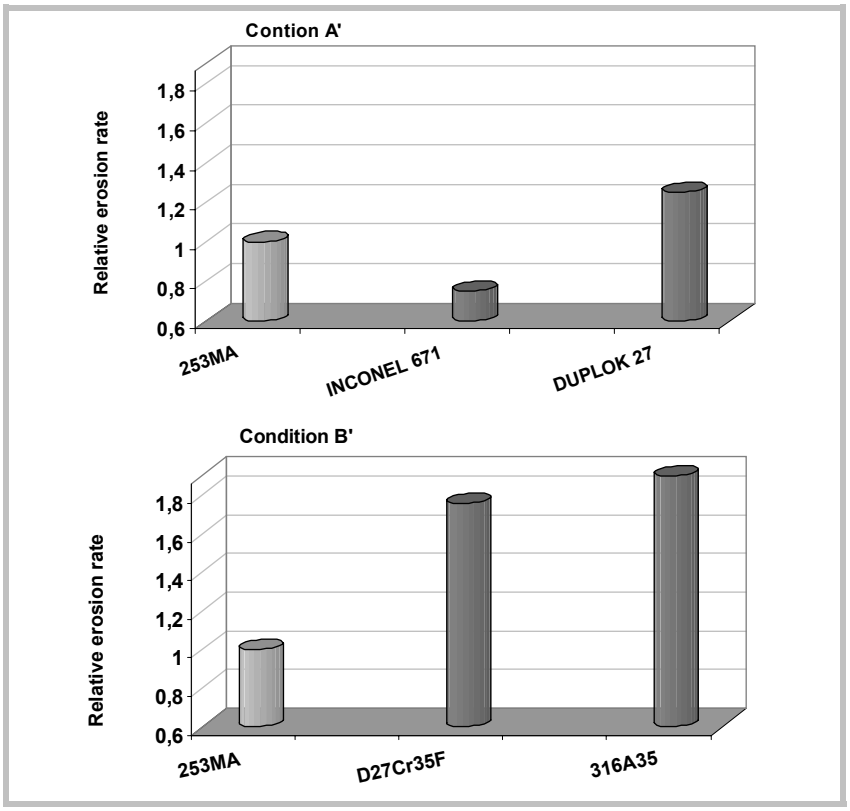


Fig. 3.7 Relative erosion rate of the stainless steel composites tested in the preliminary stage of the experiment. The erosion rate of the reference material is set as unit (gas-blast tester: 850°C, $v$ = 20 m/s, $\alpha = 60^{o}$).

### 3.3.1 Plastic Zone *L* — Room Temperature Erosion Test

The intention in selecting materials for plastic zone analysis is to collect the most indicative information to demonstrate the applicability of the localisation model in explaining, particularly, the erosion behaviour of the composites. Therefore, materials that exhibited good and bad erosion resistance are analysed along with the reference alloy.

**253MA**

The microhardness analysis indicates that a plastic zone was formed on the eroded surface of this alloy. As Fig. 3.8 (a) shows, the microhardness value drops dramatically over a short distance and then become rather constant.

**APM9935, $Al_2O_3$/APM9935**

Plastic zones were formed on the eroded surface of the reinforcement-free alloy and the $Al_2O_3$/APM9935 composite (Fig. 3.8 (b) and (c)). At the eroded surface and the unaffected bulk structure, the microhardness values of the composite are higher than that of the reinforcement-free alloy.

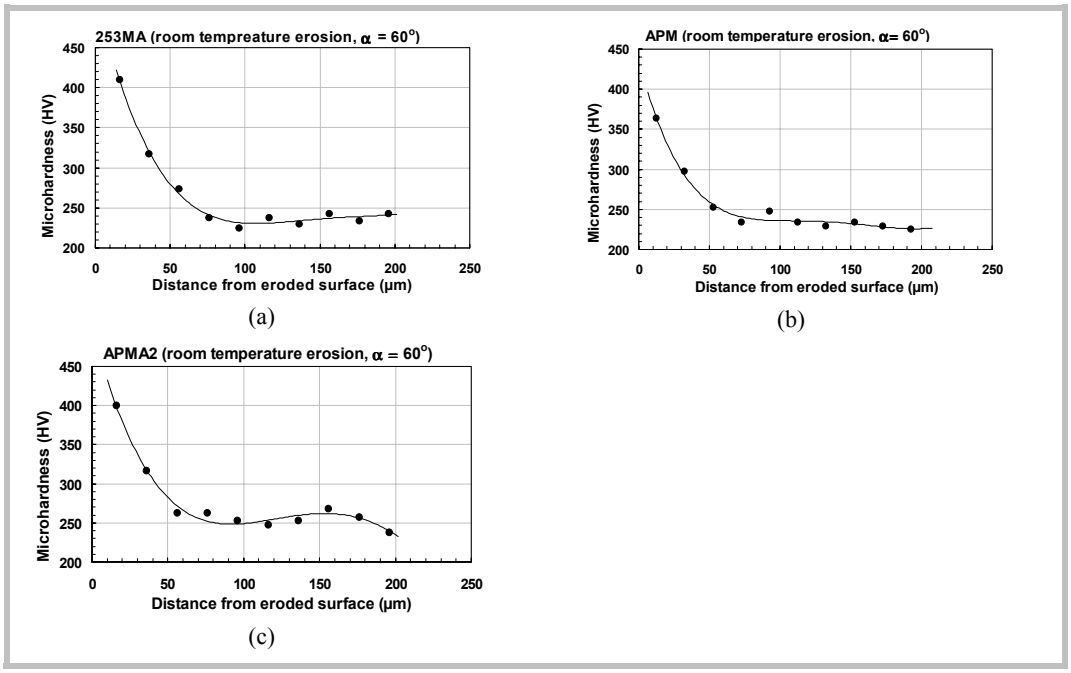


Fig. 3.8 Microhardness *vs.* distance down from the eroded surface of 253MA, APM9935 and $Al_2O_3$/APM9935 composite. The origin is set at the eroded surface (Load: 25 mg; Interval between points: 20μm; room temperature erosion test).

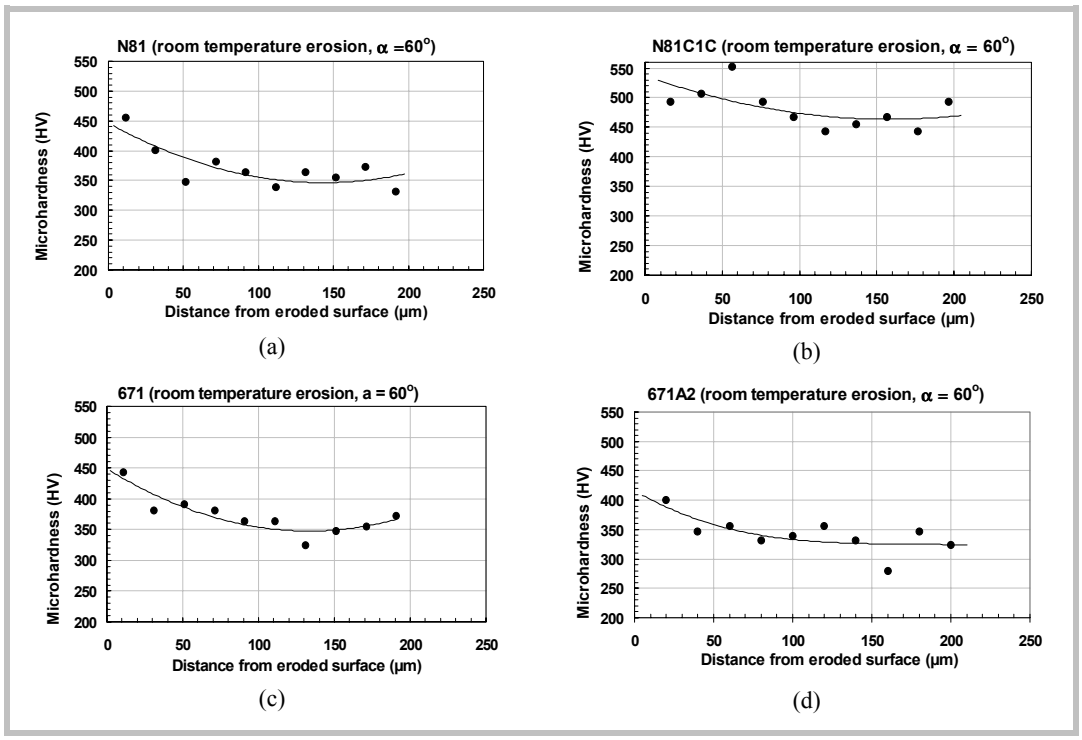


Fig. 3.9 Microhardness vs. distance down from the eroded surface the superalloys and superalloy composites. The origin is set at the eroded surface (Load: 25 mg; Interval between points: 20μm; room temperature erosion test).

**NIMONIC 81, $Cr_3C_2$/NIMONIC 81**

A plastic zone on the surface of the superalloy matrix alloy was formed, but the gradient of microhardness value was much lower (Fig. 3.9 (a)). No plastic zones could be clearly defined on the surfaces of the superalloy composites reinforced with 10 vol.% coarse $Cr_3C_2$, which had a relatively high erosion resistance in this composite system (Fig. 3.9 (b)).

**INCONEL 671, $Al_2O_3$/INCONEL 671**

The microhardness of the reinforcement-free superalloy changed in a similar fashion as the NIMONIC 81. As the figure shows, a plastic zone formed on the eroded surface of the superalloy composite reinforced with $Al_2O_3$, but the gradient of the hardness value was much lower than that in the $Al_2O_3$/steel composite (Fig. 3.9 (d) *vs*. Fig. 3.8 (c)).

In summary, the microhardness measurements indicate that a plastic zone was formed on the eroded surfaces of the heat resistant steels and the $Al_2O_3$/steel composites. However, on the surfaces of the reinforcement-free superalloys as well as the $Al_2O_3$/superalloy composites, the gradient of microhardness values through the plastic zone was much lower. Regarding the superalloy composites reinforced with 10 vol. % coarse $Cr_3C_2$, it is impossible to identify such a zone on the eroded surface. The estimated values of the plastic zone size are presented in Table 3.2.

Table 3.2 Plastic zone size L (room temperature erosion test)

| | Plastic zone size L ($\mu m$) |
|---|---|
| 253MA | 95 |
| APM9935 | 90 |
| APMA2 | 100 |
| INCONEL 671 | 80 |
| 671A2 | 105 |
| NIMONIC 81 | 75 |

Note: *L* was estimated from two or more measurements of each material.

### 3.3.2 Plastic Zone *L* — High Temperature Erosion-oxidation Test

The same idea was followed in selecting materials for microhardness measurements under the high temperature erosion-oxidation test. In this case, the aim was to test the applicability of the localisation model in explaining the erosion-oxidation behaviour of the studied composites.

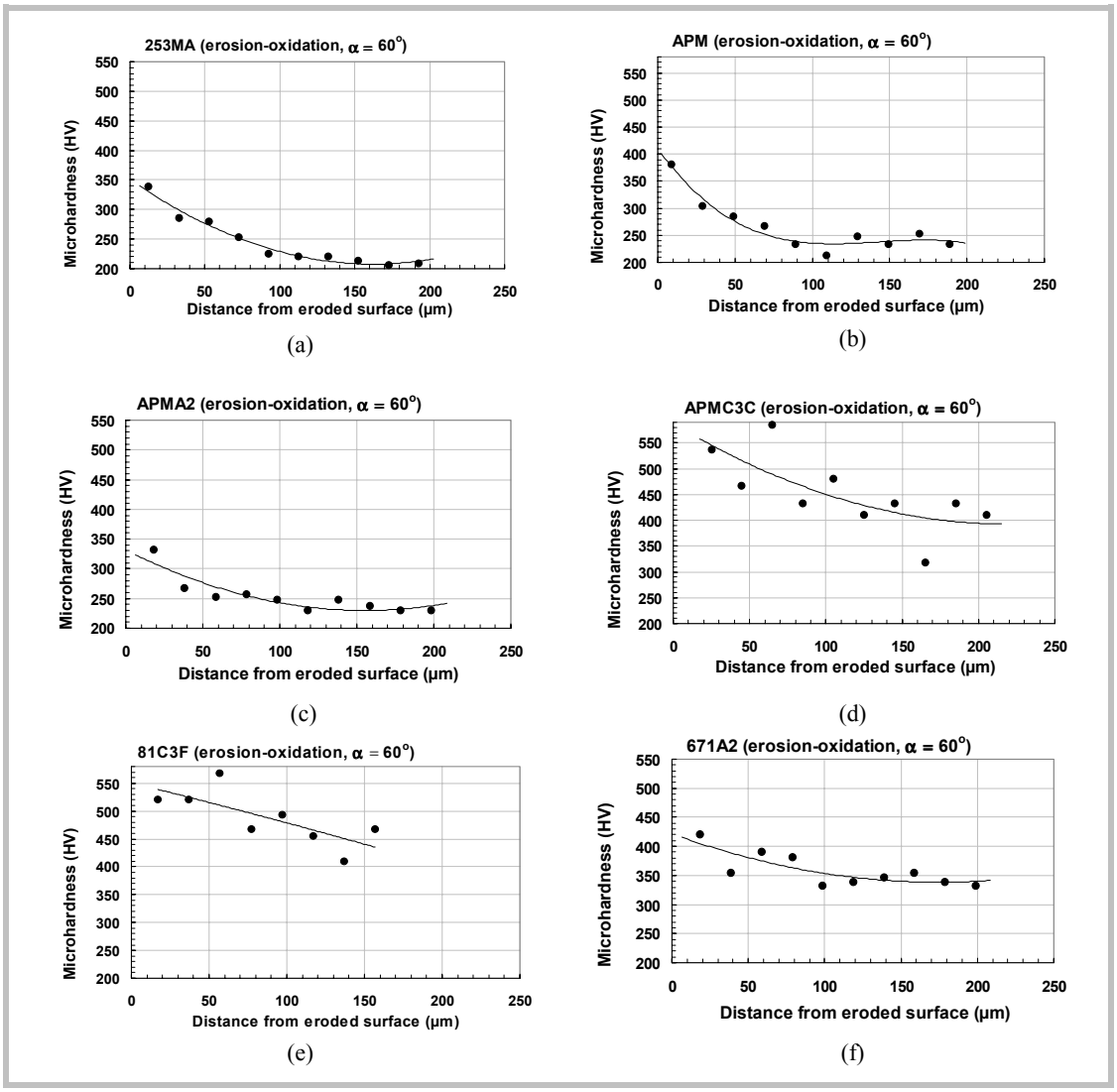


Fig. 3.10 Microhardness *vs*. distance down from the eroded surface of selected materials. The origin is set at the eroded surface (Load: 25 mg; Interval between points: 20μm; high temperature erosion-oxidation test).

**253MA**

Fig. 3.10 shows that the peak value of the microhardness at the surface as well as the bulk value are lower than the results of the room temperature erosion test (Fig. 3.8 (a) *vs*. Fig. 3.10 (a)). Another feature of the microhardness curve is the smoother transition of the hardness values through the plastic zone.

**APM9935, $Al_2O_3$, $Cr_3C_2$/APM9935**

The microhardness curve of the reinforcement-free alloy has a similar shape to that in the former case. Regarding the related composites, however, the variations of the microhardness values suggest that it is unclear if such a zone was formed in the steel composites that were reinforced with 30 vol. % coarse $Cr_3C_2$ (Fig. 3.10 (c) and (d)).

**Superalloy composites**

As in the case of the room temperature erosion test, no plastic zones could be clearly defined on the surfaces of the $Cr_3C_2$/superalloy composites. The situation of the reinforcement-free alloys was not assessable since no valid erosion-oxidation tests were conducted on the superalloys.

In general, there is a trend that under erosion-oxidation conditions, the gradient of microhardness values through the plastic zone becomes smoother if such a zone can be identified. The estimated values of *L* are presented in Table 3.3.

Table 3.3 Plastic zone size L (high temperature erosion-oxidation test)

| | Plastic zone size *L* ($\mu m$) |
|---|---|
| 253MA | 125 |
| APM9935 | 100 |
| APMA2 | 115 |
| 671A2 | 100 |

Note: *L* was estimated from two measurements of 253MA, and from only one measurement of APM9935;

# 4. Discussion

The trends in the material performance indicate that in the erosion test and at a $60^{o}$ angle of impact the composite materials were inferior to the corresponding matrix alloys in resisting the erosion attack. However, under the same impact angle, certain composites exhibited enhanced erosion resistance compared to that of the reference material in the erosion-oxidation test. The major conditional differences in the two tests were the temperature and the velocity of the impingement particles. In addition, the experiment results indicate no consistent correlation between erosion performance and alloy hardness in both of the tests, in agree with the findings in other studies [30-32].

To reveal the erosion mechanisms behind the material performance, the topographic features of the eroded surface on selected materials are demonstrated first. Then, on the cross-sectioned samples, the erosion responses of the reinforcing phases are investigated. Finally, the deformation situation at the sub-surface layers is examined, and the applicability of the strain localisation model in comparing the erosion performance of the studied materials is assessed.

## 4.1 Correlation Between Topographic Features and Erosion Performance

The eroded surfaces of the studied materials were investigated with a scanning electron microscopy (SEM). With SEM observations, the types of erosion loss of the representative materials were classified.

### 4.1.1 Room Temperature Erosion Test

SEM observation reveals that for the matrix alloys (Fig. 4.1) ploughing and type-*I* cutting were the major mechanisms for the material remove under the erosion test conditions. In Fig. 4.1, it is clear that the eroded surfaces are featured with cutting scars and craters with the extruded lips flattened by the successive impacts on the sides. The characteristics of the eroded surface suggest that severe plastic deformation occurred and materials were displaced first before being removed. The embedded erosive particles (Fig. 4.1 (a), (c) and (e)), found over the entire eroded surface, indicate the soft and ductile nature of the alloys. The topographic features for all of the matrix alloys are similar, as is the case with their erosion performance.

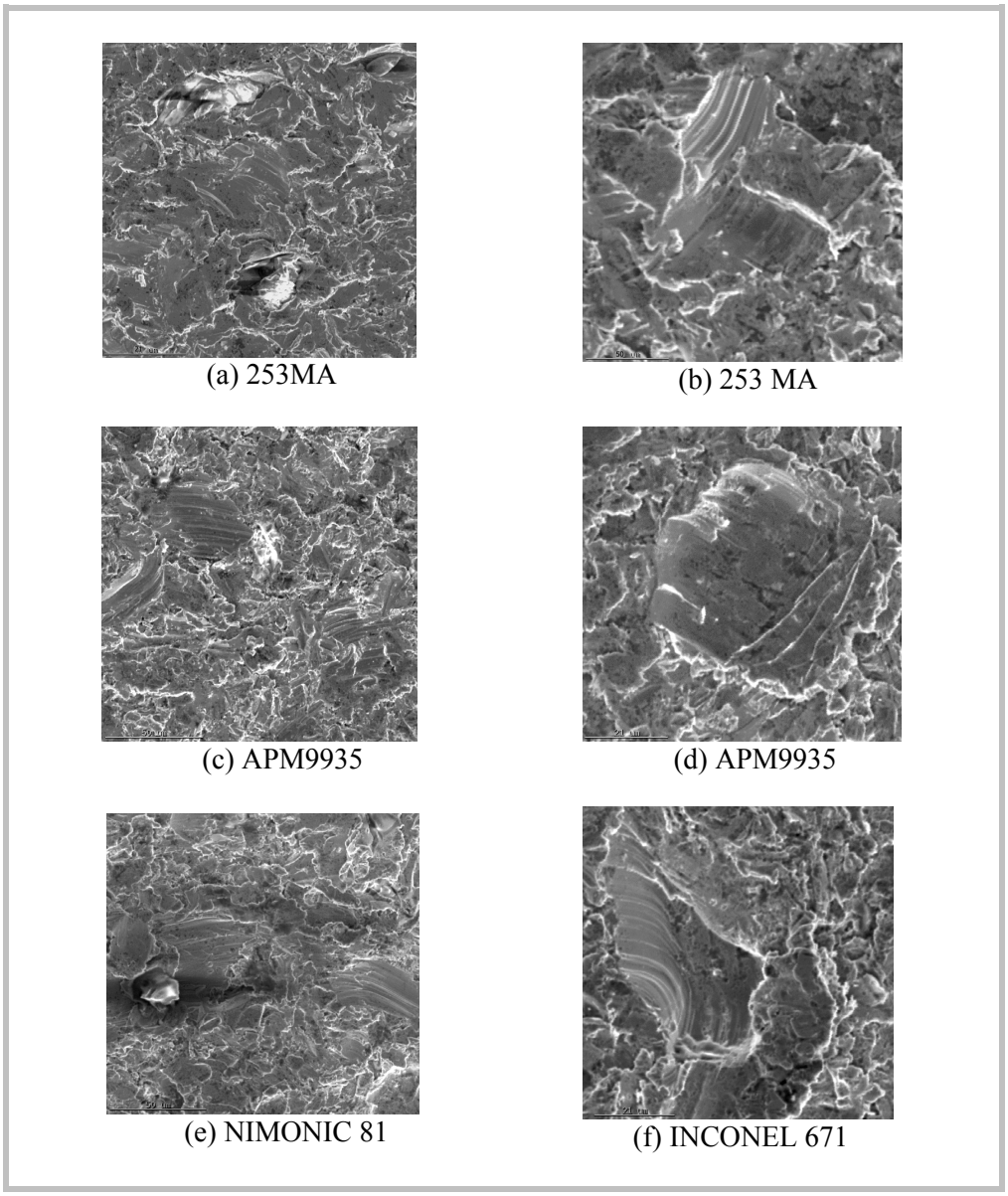


Fig. 4.1 Typical features of eroded surfaces of the reinforcement-free alloys showing the soft and ductile nature of the alloys under erosion (room temperature erosion test: $v$ = 40 m/s, $\alpha = 60^{o}$).

The typical features of the eroded surface of the composites are presented in Fig. 4.2. In general, the composite surfaces were much more damaged than the surface of the reinforcement-free alloys. While the alloy surfaces look more smeared (Fig. 4.1), the surfaces of the composite were crushed, especially at the interfacial areas around the reinforcement particles (Fig.4.2).

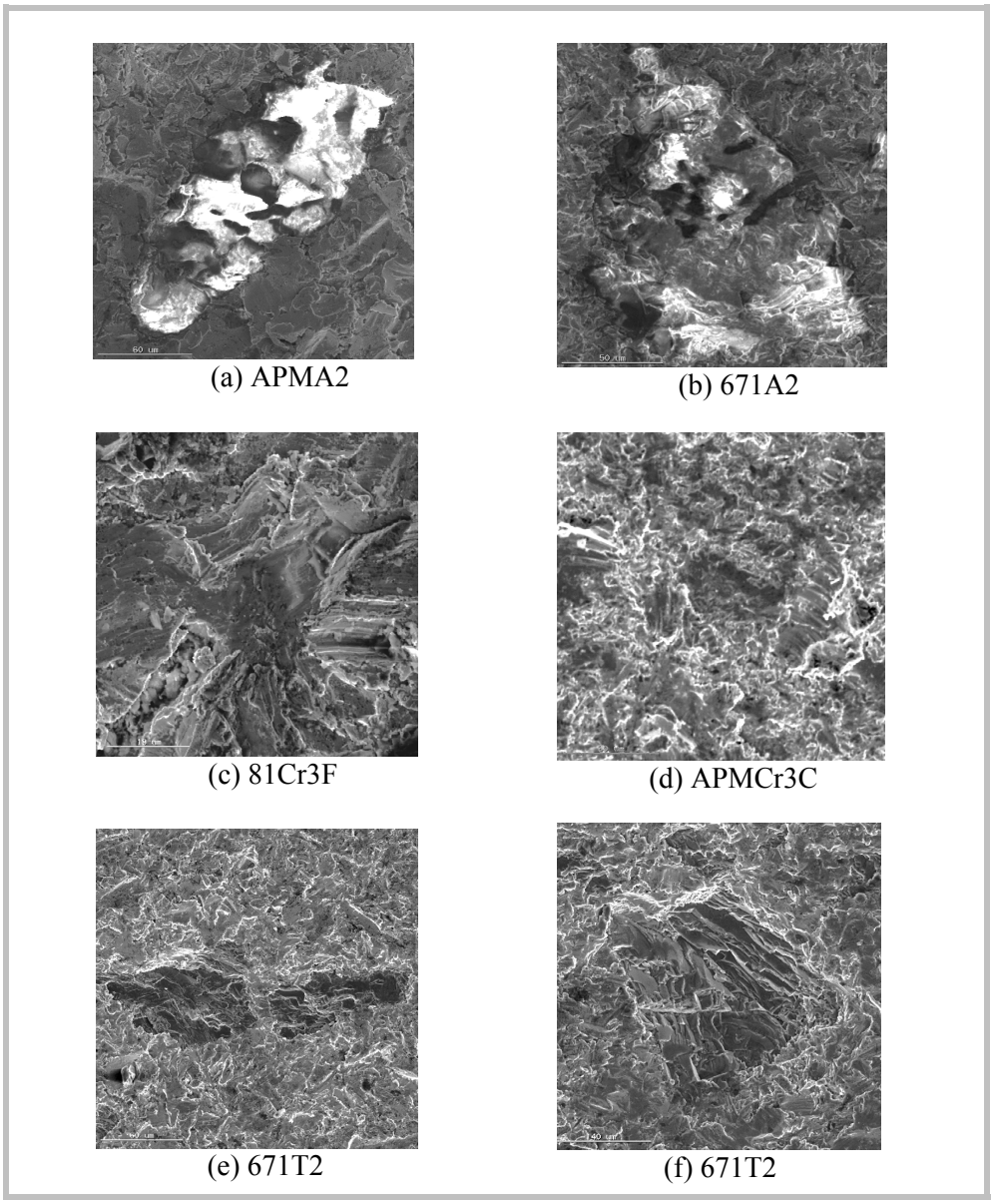


Fig. 4.2 Typical features of eroded surfaces of the composite materials showing severe erosion damage particularly at the matrix/reinforcement interfacial region (room temperature erosion test: $v$ = 40 m/s, $\alpha = 60^{o}$).

The topographic features indicate that the erosion losses of the composites were controlled, mainly, by the damage patterns of the ceramic reinforcements. It is clear that the force of the impacting particle was sufficient to cause widespread fracture of the reinforcing particles at the surface. The broken reinforcing particles were easily removed, leaving the surrounded matrix materials vulnerable to the subsquent impacts. This detrimental effect of the reinforcing phases explains the poor erosion performance of the composites under the erosion test conditions. The impact force was so high that it is likely that a single impact could cause massive breakdown of a reinforcement particle at the surface. This is seen from the SEM observations at the boundary regions between the eroded and the unaffected areas (referring to Fig. 2.4). As Fig. 4.3 shows,

even the impacts of stray particles could cause severe damage to the reinforcing phases, while the surrounding matrix areas were little affected.

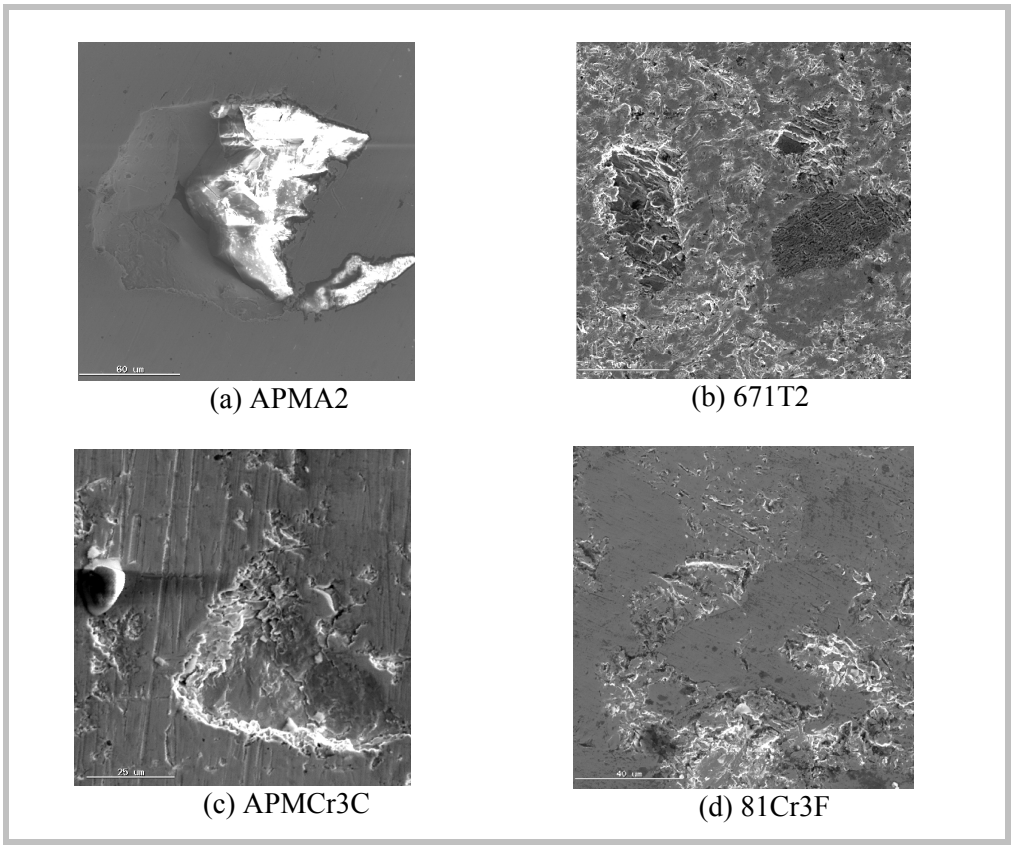


Fig. 4.3 Damage of reinforcement phases by the impacts of stray eroding particles at the boundary regions between eroded and unaffected areas. The $Al_2O_3$ particles are rather brittle comparing to the TiC and $Cr_3C_2$ ones (room temperature erosion test: $v$ = 40 m/s, $\alpha = 60^o$).

The erosion pattern of the reinforcing phases underlines the relative erosion resistance among the composites. Fig. 4.2 and 4.3 demonstrates that the breakdown of the $Al_2O_3$ particles was in a pure brittle manner and the bonding with the matrices appeared rather weak. As a result, the erosion performance of the $Al_2O_3$ reinforced composites was poor. The erosion damage of the TiC particles proceeded in a similar way, but the cracks seemed to experience, to certain extent, difficulties in propagation. Therefore, small pieces of TiC particles at surface were removed upon impacts, and it is likely that plastic deformation occurred before the final detachment. As a result, composites reinforced with TiC performed better than those with $Al_2O_3$ (Fig. 3.1).

The erosion pattern of the $Cr_3C_2$ reinforcing phase was complex, as signs show clearly that plastic deformation occurred and played a role in the course of the material remove (Fig. 4.2, (c), (d)). This ductile behaviour may have a positive effect on the erosion of the composites

depending on the composite system, comparing the erosion behaviour of the INCONEL 671 based composites to that of the APM9935 based ones. The erosion responses of the $Cr_3C_2$ reinforcement depended, to a large extent, on its chemical stability as well as the bonding situation at the matrix/reinforcement interfacial area. An interesting phenomenon is demonstrated in Fig. 4.3 (c) and (d). The figures show that in an APMCr3C composite, a $Cr_3C_2$ particle was knocked off and the interfacial areas were damaged by the impact of stray eroding particles (Fig. 4.3 (c)). However, in the case of 81Cr3F composite, the interfacial areas as well as the bulk $Cr_3C_2$ particle remained sound under the attack of stray eroding particles (Fig. 4.3 (d)). This will be discussed in more detail when the cross-sectioned samples are examined.

### 4.1.2 High Temperature Erosion-oxidation Test

SEM observation on the eroded surfaces indicates that oxidation occurred on all of the tested materials to different level. However, in general, the topographic features are similar to those in the room temperature erosion test.

Fig. 4.4 shows typical features of the eroded surface of the APM9935 matrix alloy. Craters, cutting scars, and embedded impingement particles are found over the entire surfaces, indicating the ductile nature of the erosion process of this alloy. However, debris of oxidised material at surface is visible on the surface. Compared to the superalloys, it is argued that the steel alloys became particularly soft under the testing temperature so that the surface was roughened severely by the impingement particles. The heavily strained ridges, or pushed-up materials, underwent higher-rate oxidation than those at the valley because of the high surface-to-volume ratio. Here, it should be emphasised that this higher-rate oxidation does not necessarily, though possible, suggest a change in the oxidation kinetics under the impact, and the oxidation mechanisms are believed not changed. The highly oxidised materials were then forged flat upon successive impacts and detached easily in large pieces because of loose connection to the underlying material. Therefore, the steel alloys experienced higher material losses under the erosion-oxidation conditions than they had in the erosion test.

The $Al_2O_3$ reinforced composites, the worst performing in the erosion test, were the best performing materials under the erosion-oxidation conditions (Fig. 3.6). It can be seen that the $Al_2O_3$ particles stood well after multiple impacts with no massive breakdown (Fig. 4.5). Materials at the interfacial areas were not especially vulnerable to the impact attack and were removed evenly.

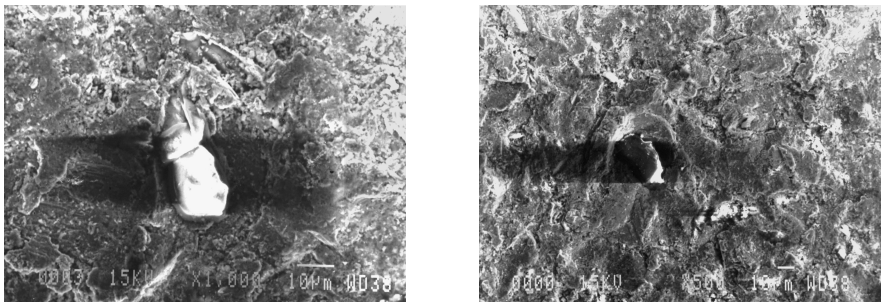

(a) APM9935 (b) APM9935

Fig. 4.4 Topographic features of eroded surface of the APM9935 matrix alloy. The embedded $SiO_2$ particles in the middle of the pictures indicate the ductile nature of the alloy at the testing temperature (high temperature erosion-oxidation test: 850°C, $v$ = 20 m/s, $\alpha = 60^{o}$).

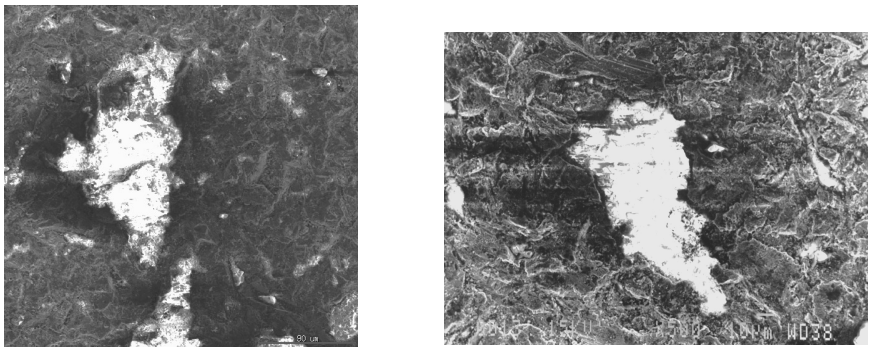

(a) APMA2 (b) 671A2

Fig. 4.5 Topographic features of eroded surface of the $Al_2O_3$ reinforced composites indicate no massive breakdown of the reinforcement particles (high temperature erosion-oxidation test: 850°C, $v$ = 20 m/s, $\alpha = 60^{o}$).

This is contrary to the situations in the room temperature erosion test (Fig. 4.5 *vs*. Fig. 4.2 (a), (b)). It is argued that there are three reasons for this change. Firstly, the impinging particles in the erosion-oxidation test possessed much less energy than in the erosion test, as the velocity dropped from 40 to 20 m/s. The reduced impact energy became insufficient to induce massive breakdown of the $Al_2O_3$ particles. Secondly, the high temperature involved in the test enhanced the bonding strength between the $Al_2O_3$ particles and the matrix alloy, leading to a more efficient transfer of impact energy to the surrounding matrix. Thirdly, the high-temperature strength and toughness of the matrix alloy was enhanced because of the presence of the reinforcement, and consequently the magnitude of surface roughening in the matrix regions was reduced. Considering the foregoing analysis, this indirect contribution to the erosion of composites was positive. The last two arguments will be tested when the cross-sectioned test pieces are analysed.

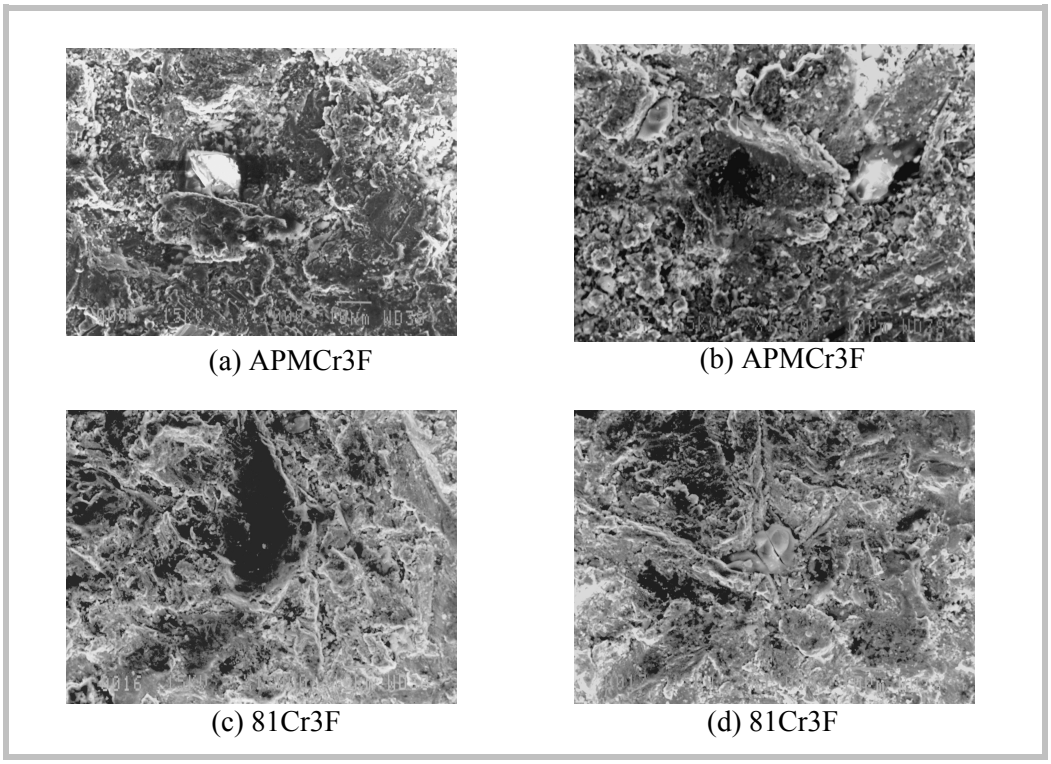


Fig. 4.6 Topographic features of eroded surface of the $Cr_3C_2$ reinforced composites showing severe damage at the reinforcement concentrated area (high temperature erosion-oxidation test: 850°C, $v$ = 20 m/s, $\alpha = 60^o$).

The erosion trend of the $Cr_3C_2$ reinforced composites is not consistent in different composite systems (Fig. 3.6). In the case of steel composites, topographic observation indicates no signs of protecting effects [139] from the $Cr_3C_2$ reinforcement, but suggests a worsened situation of surface damage due to the presence of the reinforcement (Fig. 4.6 (a) and (b)). This is to say that the positive effect of the reinforcing phase in reducing the magnitude of surface roughening was overshadowed by the massive breakdown of the reinforcement itself. Consequently, the erosion rates of the steel/$Cr_3C_2$ composites were higher than that of the matrix alloy and scaled with the reinforcement concentration.

On the other hand, some of the composites exhibited enhanced erosion resistance than that of the reference alloy (Fig. 3.6 (c), (d)). Moreover, this enhancement was only achieved when the volume percentage of the reinforcement was high. Unlike the situation in the erosion test, this suggests that under the erosion-oxidation conditions the breakdown of the $Cr_3C_2$ particles was no longer the dominant mechanism in controlling the overall erosion of the $Cr_3C_2$/superalloy composites. To better understand the erosion mechanisms in this composite system, the cross-sectioned specimens are examined to demonstrate the erosion responses of the reinforcing phase and the deformation situations at sub-surfaces.

## 4.2 Erosion Responses of Reinforcing Phases and Sub-surface Deformation

It is demonstrated that the erosion responses of reinforcing phases are critical for the overall erosion performance of composite material [139]. While topographic observations provide general information on the erosion responses of reinforcing phase, more indicative information can be obtained by examining the cross-sectioned surface of eroded samples. Moreover, the deformation situation at sub-surfaces can be revealed by means of microhardness measurement of the cross-sectioned samples. This yields to an important parameter, the plastic zone size ($L$) with which, according to the strain localisation model [25-27], the relative erosion resistance of materials of the same type can be compared.

### 4.2.1 Erosion Responses of Reinforcing Phase and Sub-surface Deformation — Room Temperature Erosion Test

The topographic features of the eroded surface suggest that the erosion losses of the composites were controlled, mainly, by the damage patterns of the reinforcement particles. This is backed by a SEM examination of the cross-sectioned specimens.

Fig. 4.7 shows the typical features of the cross-sectioned sample of the $Al_2O_3$ reinforced composites. It is clear that the reinforcement particles were crushed and detached from the surfaces. The sites of the reinforcement particles became concave regions, and the surrounding matrix alloy suffered accelerated erosion loss. Investigation of the interface between the steel matrix and the $Al_2O_3$ particles using energy dispersion spectroscopy (EDS) reveals that the interfacial areas were free of new phases (Fig. 4.8). This was expected since $Al_2O_3$ is completely inert in iron [147]. However, the EDS analysis suggests that the matrix and the reinforcing phase were soluble though nonreactive, since a diffusion-type layer of about 1μm in thickness was developed at the interface (Fig. 5.8). This type of thin layer has been reported to be beneficial to the bonding strength of a metal/ceramic interface [143, 148-150]. In this study, the bonding between the matrix and the reinforcement was sound, although the $Al_2O_3$ particles at the surfaces appears brittle and thus vulnerable to the impact of the erodent (Fig. 4.7).

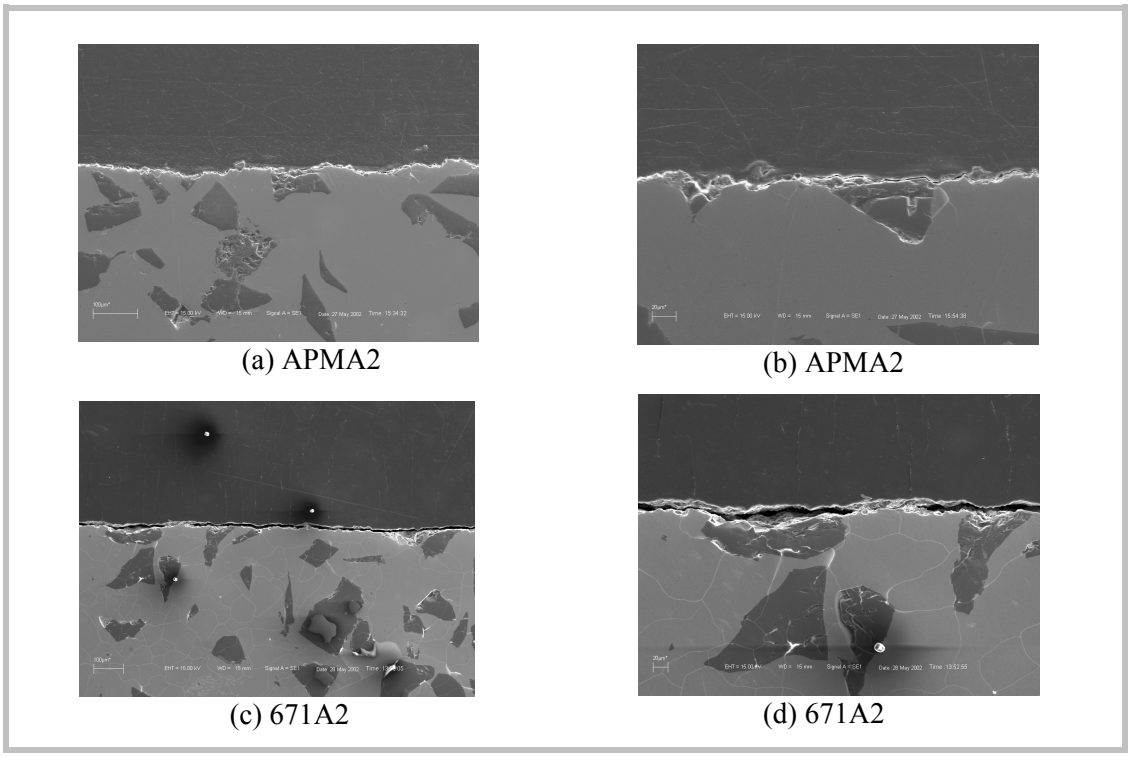


Fig. 4.7 Typical features of cross-sectioned specimens of $Al_2O_3$ reinforced composites indicating the erosion responses of the reinforcing phase (room temperature erosion test: $v = 40$ m/s, $\alpha = 60^o$).

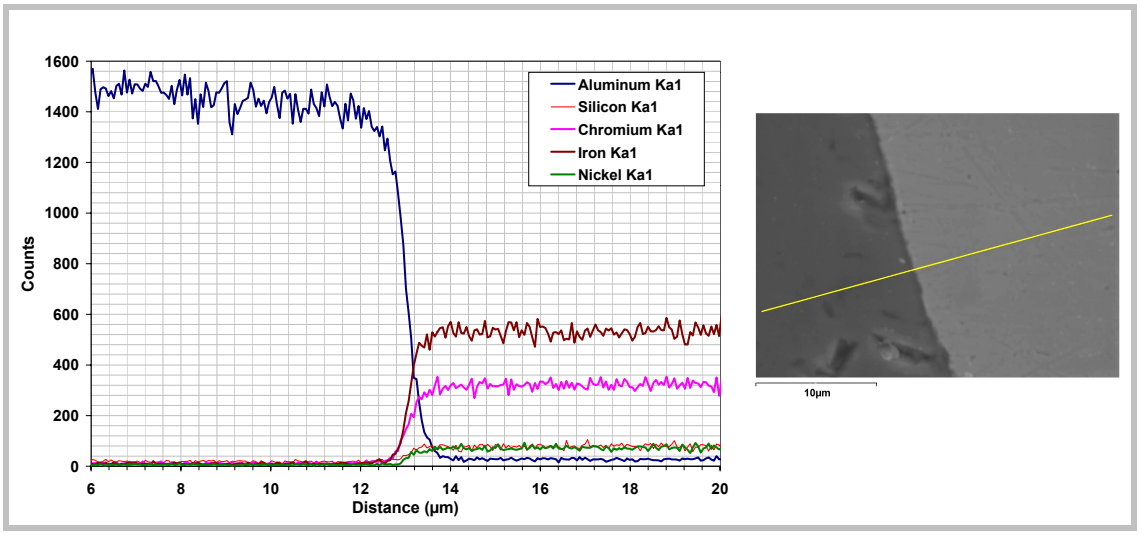


Fig. 4.8 Line scan using EDS showing the situation of interfacial area in an APMA2 composite (room temperature erosion test: $v = 40$ m/s, $\alpha = 60^o$).

The SEM observations on cross-sectioned specimens also support the idea that the damage pattern of the reinforcing particles determined the relative erosion resistance among the composites. Fig. 4.9 demonstrates the typical features of cross-sectioned samples of the $Cr_3C_2$ and TiC reinforced composites. In the steel composites, the detrimental effect of the $Cr_3C_2$ reinforcement was as poor as that of the $Al_2O_3$ (Fig. 4.7 (a), (b) *vs*. Fig. 4.9 (a), (b)). The particles suffered massive breakdown and were removed in large pieces, leading to high erosion rates (Fig. 4.9 (a), (b)). On the other hand, the $Cr_3C_2$ and TiC particles in the superalloy composites were chipped off in small pieces. Meanwhile, signs of plastic deformation occurring in the course of material removal are observable in the superalloy-based composites (Fig. 4.9 (c), (d)).

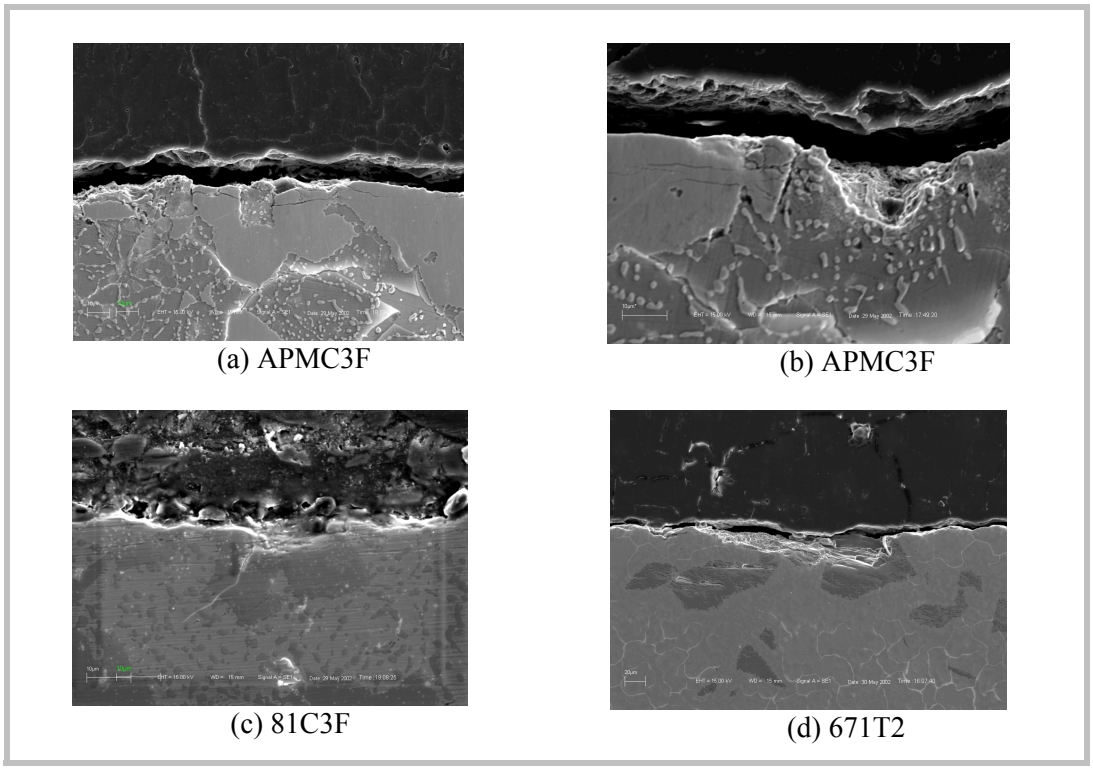


Fig. 4.9 Typical features of cross-sectioned samples of $Cr_3C_2$ and TiC reinforced composites indicating the erosion responses of the reinforcing phase in different composite systems (room temperature erosion test: $v$ = 40 m/s, $\alpha = 60^o$).

To understand the behaviour of the $Cr_3C_2$ particles in different composite systems, EDS analysis was carried out on the metal/ceramic interfaces. In Fig. 4.10, one can see that in the $Cr_3C_2$/steel composite, dissolution of the reinforcement particles occurred at the metal/ceramic interface. The interfacial layer is not a pure diffusion-type layer, which is featured with planar front as in the case of the $Al_2O_3$/steel composite (Fig. 4.8). This dissolution might have several effects, for example lowering the interface strength, reducing the load bearing capacity of the reinforcement, and decreasing the toughness and strength of the surrounding matrix. The

consequence was high erosion rates of both the reinforcement and the matrix. In the case of $Cr_3C_2$/superalloy composites, a diffusion-type interface with a planar front was developed (Fig. 4.10 (b)). The sound interface strength is believed to be the reason for the higher erosion resistance of the $Cr_3C_2$/superalloy composites than the $Cr_3C_2$/steel as well as the TiC/superalloy composites.

The poor performance of the TiC/superalloy can also be understood from the EDS analysis (Fig. 4.10 (c)). It is clear that a new phase, possibly an intermetallic compound consisting of Ni and Ti, was developed at the places where Ni in the two-phase superalloy was in contact with the TiC particles. The entire interfacial region was somewhat thick (over 2.5μm) and therefore, the bonding was weak. Moreover, the intermetallic compound (about 0.5 μm in thickness) might be especially vulnerable to the erosion attack because of its brittle nature.

However, it should be reminded that under erosion test conditions, the reinforcing phases in general provided no protection to the matrix alloys, and consequently the overall erosion performance of the composites was poor. The ceramic reinforcements were actually the more vulnerable targets and underwent high rates of erosion loss in all of the composite systems.

The deformation situation at the sub-surfaces of selected materials was investigated by measuring the plastic zone size $L$, following the idea of strain localisation. For the reinforcement-free alloys, $L$ appears to be a useful parameter in revealing the relative erosion resistance among the materials of same type. It shows that the two superalloys had similar erosion rates, amd $L$ values (refer to Fig. 3.1 and Table 3.2). The same situation is also found for the two heat-resistant steels. Here, it should point out that a direct comparison of erosion resistance between the superalloys and the steels according to $L$ may not be valid, though shorter $L$ seems to be associated with lower erosion rates. This is because that $L$ alone can be relied on to predict qualitatively the erosion resistance of materials only if $\varepsilon_c$ is constant (Equation (1-23)). For different alloy systems, $\varepsilon_c$ is most probable different. Besides, $L$ also varies with impact angle and tends to become shorter at lower angle [41, 47]. In this study, the angle effect on the development of the plastic zone seems more evident in the superalloys since, compared to the steels, the gradient of the hardness values through the plastic zone was much lower.

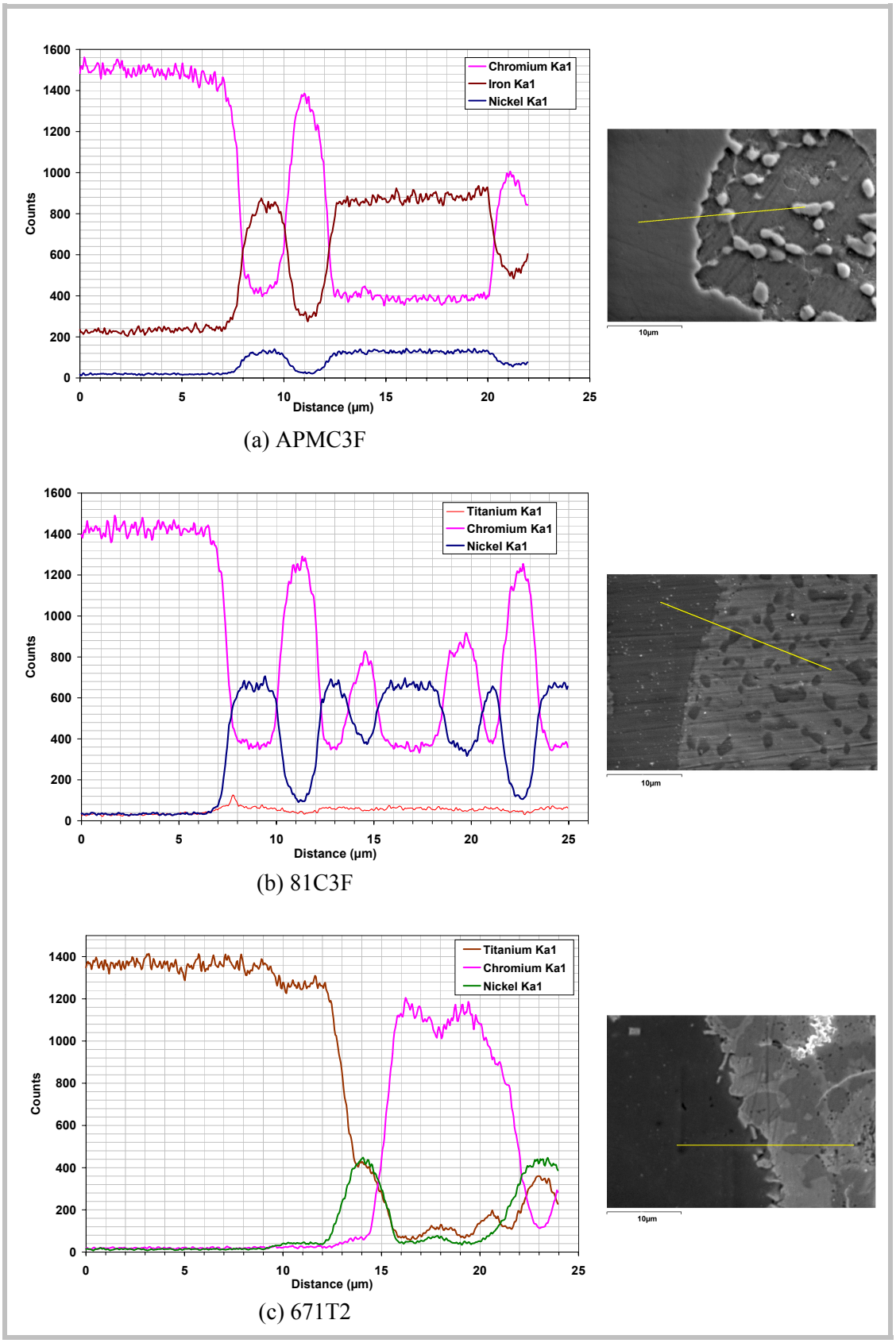


Fig. 4.10. Line scan using EDS showing the situation at the interfacial area in the steel and superalloy composites (room temperature erosion test: $v = 40$ m/s, $\alpha = 60^{o}$).

On the other hand, it is not clear if $L$ is a valid parameter in predicting composite erosion rate. In the case of $Al_2O_3$ reinforced composites, $L$ values are higher than those of the corresponding matrix alloy, as are erosion losses. However, this increase may come from the influence of residual strain in the composite on the erosion induced plastic zone on which the two deformations are superimposed. In general, it may be argued that for a composite, the magnitude of $L$ should be determined principally by the $L$ of the corresponding matrix alloy, but the interference of the reinforcing phase will have an influence on the final value. This is because the development of this plastic zone in ductile metals is the result of plastic deformation under adiabatic and high strain-rate conditions, and strengthening mechanisms have little effect on it. In cases where the role of the reinforcing phase is more complicated in the mechanical behaviour of the composite due to, for instance, interface reaction, uneven distribution, or premature fracture, the plastic zone may not be identifiable. This is the case for the $Cr_3C_2$/composites in this study.

In practice, to measure the erosion induced plastic zone in composites, the regions must be selected carefully so that the indentation is far from the reinforcing phase. This is particularly difficult when the reinforcement concentration is high. It is also advisable that a low measuring load and short intervals should be used. Finally, it should be kept in mind that sample preparation could also have a strong influence on the measured value of $L$.

### 4.2.2 Erosion Responses of Reinforcing Phase and Sub-surface Deformation — High Temperature Erosion-oxidation Test

The SEM examination of cross-sectioned samples indicates a clear link between the erosion responses of the reinforcing phases and the overall erosion performance of the composites in the high temperature erosion-oxidation test. The examination also suggests that the impact of the erosive particles did not change the oxidation mechanisms of the matrix alloys, and, therefore, had little effects on the erosion behaviour of the composites

As Fig. 4.11 shows, the reinforcing phase in the $Al_2O_3$ reinforced composites stood well after the erosion attack with no massive breakdown. The protruding $Al_2O_3$ particles on the eroded surfaces, a unique feature contrary to the situations in the erosion test, acted as shelters that effectively reduced erosion damages in the matrix regions (Fig. 4.11 *vs*. Fig. 4.7). This beneficial effect of the $Al_2O_3$ reinforcing phase is brought about by the change of erosion mechanism under different test conditions. As is demonstrated in the introductory part, transitions in erosion rate and mechanisms are a common feature of the erosion of brittle materials. In such cases, a relatively small change in erosion conditions results in significant change in the erosion mechanism. Referring to Fig. 1.18 (b), it is believed that under the erosion-oxidation test conditions the dominant mechanism for the $Al_2O_3$ reinforcement was changed

from lateral fracture to plastic deformation, as the impact velocity dropped from 40 to 20 m/s. Consequently, the erosion rate of the $Al_2O_3$ was much lower.

The situation at the interface region in the $Al_2O_3$ based composites was similar to that in the room temperature erosion test. Comparing Fig. 4.12 with 4.8, one can see that under erosion-oxidation conditions, the interface region remained clean and the interface layer remained thin. EDS analysis indicates that the diffusion layer developed in the erosion-oxidation test was slightly thicker. At this point, it is not clear whether the bonding strength was improved. However, it may still be claimed that at high temperature, the bonding strength could be enhanced by improving the interface homogeneity and reducing the residual stress at the interfacial area. As a result, the impact energy could be transferred more efficiently to the ductile matrix, reducing the possibility of immediate breakdown of the $Al_2O_3$ particles.

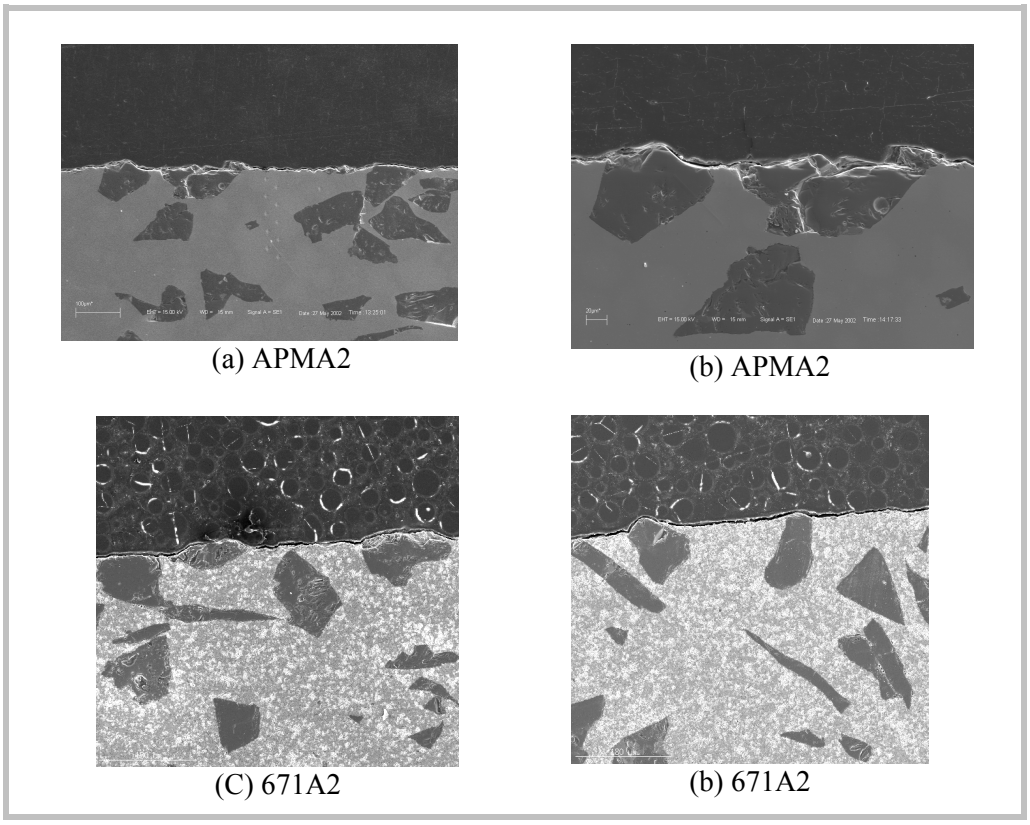


Fig. 4.11 Typical features of cross-sectioned samples of $Al_2O_3$ reinforced composites indicating the protection effect of the reinforcing phase in resisting the erosion attack (high temperature erosion-oxidation test: $T^oC = 850$, $v = 20$ m/s, $\alpha = 60^o$).

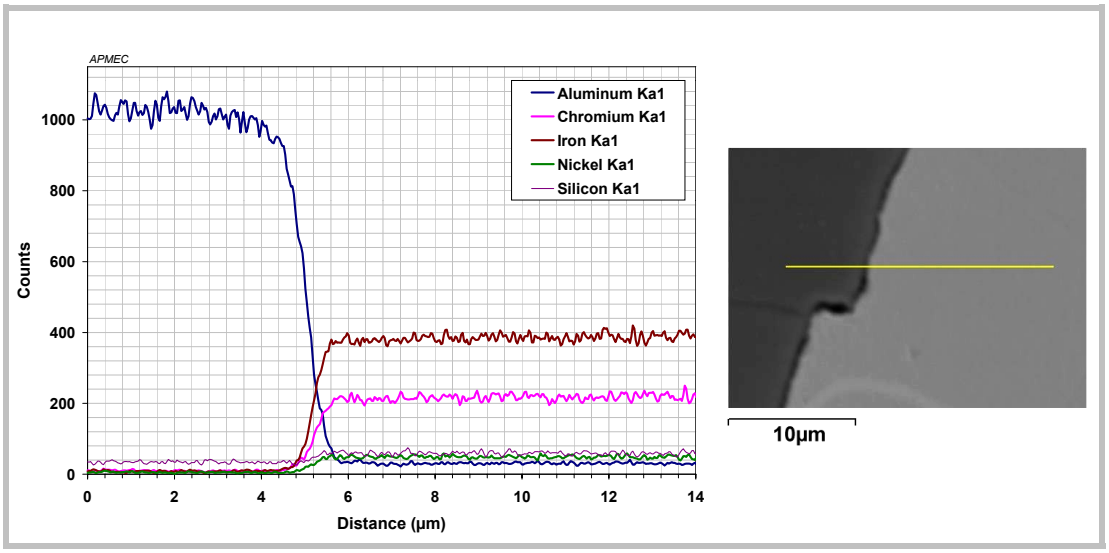


Fig. 4.12 Line scan using EDS showing the situation of interface area in a APMA2 composite (high temperature erosion-oxidation test: T°C = 850, $v$ = 20 m/s, $\alpha$ = 60°).

The effect of surface-roughening reduction by the reinforcement to the erosion of composite is also demonstrated in the SEM observation on cross-sectioned samples. This indirect and positive contribution is considered more significant under the high temperature oxidising conditions. This is because if the magnitude of surface roughening can be reduced the oxidation rate of the matrix at the surface will be lower, as will be the erosion rate. In Fig. 4.13, one can see that the surface of the reinforcement-free APM9935 alloy was so soft that the erodent particles ($SiO_2$) could be embedded easily into the sub-surface layer. The highly strained, oxidised, and roughened surface layer was porous and, therefore, could be easily removed. On the other hand, the eroded surface of the $Al_2O_3$/APM9935 composites was comparatively even and solid (Fig. 4.11 (a), (b)). This becomes more evident in the case of $Al_2O_3$/superalloy composites (Fig. 4.11 (c), (d)).

The erosion responses of the $Cr_3C_2$ reinforcement were not consistent in different composite systems. For the $Cr_3C_2$/steel composites, the erosion response is somewhat similar to the situation in the room temperature test (Fig. 4.14 (a), (b) *vs*. Fig. 4.9 (a), (b)), suggesting similar erosion mechanisms in both tests. In other words, the impacts were still powerful enough to cause massive breakdown of the $Cr_3C_2$ particles, although the velocity was only half that in the erosion tests. Therefore, the erosion rates of the composites were higher than that of the matrix alloy and scaled with the volume percentage of the $Cr_3C_2$. The beneficial effect of the $Cr_3C_2$ particles in reducing the surface roughening was again overshadowed by the massive breakdown of the reinforcing phase itself.

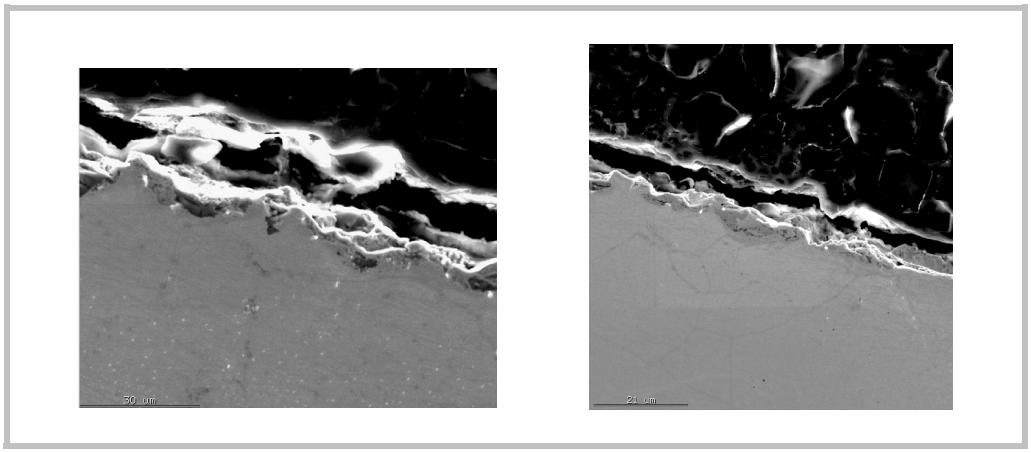

Fig. 4.13 SEM observation of cross-sectioned samples of the APM9935 heat-resistant steel showing the roughened surface and the embedment of erodent particles (high temperature erosion-oxidation test: T$^{o}$C = 850, $v$ = 20 m/s, $\alpha$ = 60$^{o}$).

The role of the $Cr_3C_2$ reinforcement in the erosion of the $Cr_3C_2$/NIMONIC 81 composites appears more complicated. Here, it is assumed that the erosion rate of the reinforcement-free NIMONIC 81 alloy is lower but close to that of the reference steel, since no valid measurement of this superalloy was made. Under this assumption, the comparison of composite erosion rates with that of the reference alloy suggests that the reinforcing phase seemed detrimental at low concentration but might become beneficial at higher concentrations (Fig. 3.6 (c) and (d)). Therefore, the erosion performance of the $Cr_3C_2$/NIMONIC 81 composites should be the results of competitive operation of the two mechanisms: surface-roughening reduction of the reinforcing phase and massive breakdown of the reinforcing phase itself. If such were the case, the magnitude of the breakdown of the $Cr_3C_2$ particles would be low under the erosion-oxidation conditions, since so far the benefit of surface-roughening reduction has been always overshadowed by the detriment of massive breakdown. In Fig. 4.14, one can see that the $Cr_3C_2$ particles in the superalloy composite are more ductile and tougher than the ones in the steel composite (Fig. 4.14 (a), (b) *vs*. (c), (d)). In addition, signs of plastic deformation during the erosion events are observable (Fig. 4.14 (c) and (d)). To reveal the reasons for the different behaviour of the $Cr_3C_2$ phase, EDS analysis was arranged to investigate the situations at the metal/ceramic interface.

The EDS analysis indicates that the situation at the metal/ceramic interface in the $Cr_3C_2$ reinforced composites was similar in both of the tests (Fig. 4.15 *vs*. 4.10). As in the erosion test, the dissolution of the $Cr_3C_2$ particle into the steel matrix was severe (Fig. 4.15 (a)), and this dissolution was detrimental to the erosion resistance of the composites, as discussed earlier. On the other hand, a layer of diffusion-type was developed at the metal/ceramic interface in the $Cr_3C_2$/superalloy composites (Fig. 4.15 (b)). Comparing Fig. 4.15 (a) with (b), one can see that the diffusion-type layer at the $Cr_3C_2$/superalloy interface was thicker than the layer of unknown

type at the $Cr_3C_2$/steel interface. This diffusion layer is believed to contribute to the tougher behaviour of the $Cr_3C_2$ particles in the superalloy composites.

The poor erosion resistance of the TiC/superalloy composites can also be explained by analysing the bonding at the metal/ceramic interface. Compared to the situation in the erosion test, the region of a new phase, possibly an intermetallic compound of Ni and Ti, was widened under the erosion-oxidation conditions (Fig. 4.16 *vs*. 4.10 (c)). Further study with SEM suggests that the new phase was brittle with weak bonding between the bulk TiC particle and the matrix (Fig. 4.17). This is particularly true at the places where the TiC particles were in contact with the Cr phase of the two-phase matrix alloy, since the interdiffusion rate between Cr and Ti was low compared to that between Ni and Ti (Fig. 4.16).

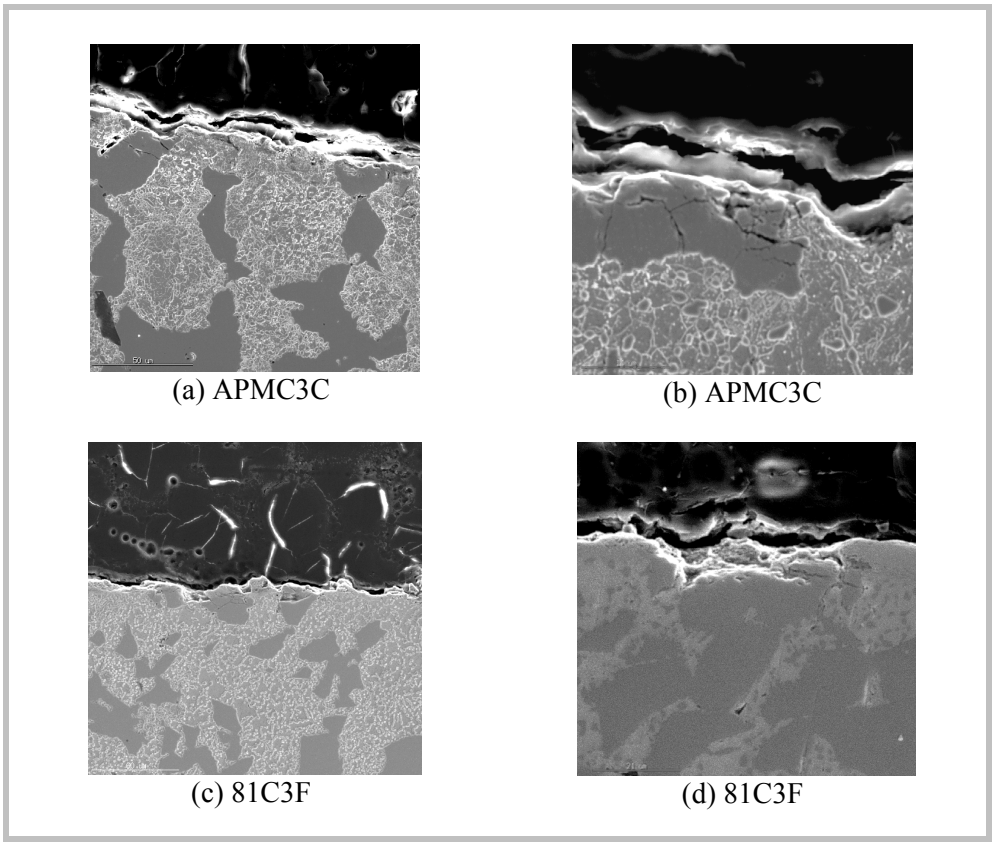


Fig. 4.14 Typical features of cross-sectioned samples of $Cr_3C_2$ reinforced composites indicating the erosion responses of the reinforcing phase (high temperature erosion-oxidation test: $T^oC = 850$, $v = 20$ m/s, $\alpha = 60^o$).

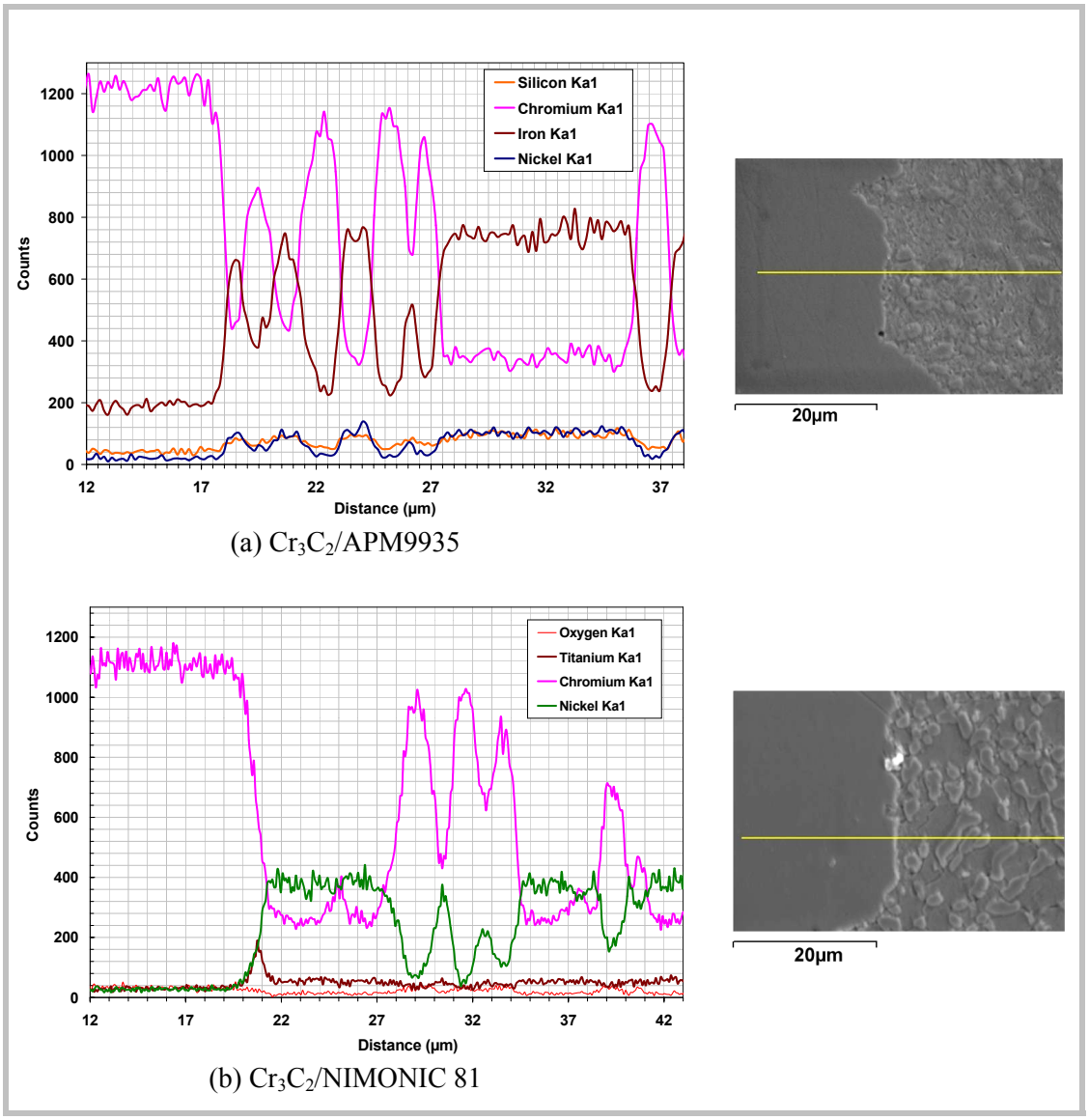


Fig. 4. 15 Line scan using EDS showing the situation at the interface area in the $Cr_3C_2$ reinforced steel and superalloy composites (high temperature erosion-oxidation test: $T^oC = 850$, $v = 20$ m/s, $\alpha = 60^o$).

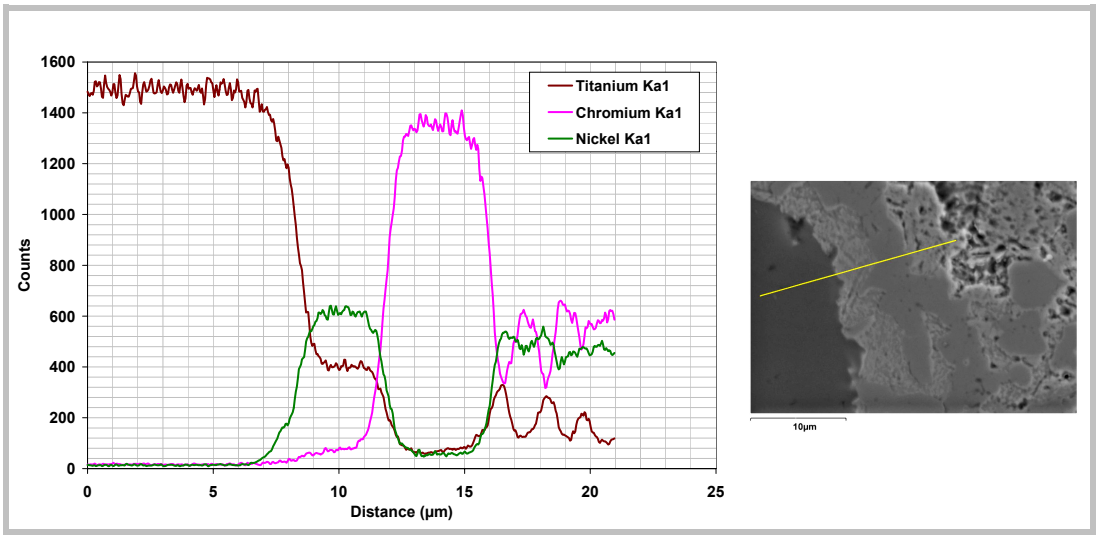


Fig. 4.16 Line-scan using EDS showing the situation of interface area in a TiC/INCONEL 671 composite. A thick layer of intermetallic compound consisting of Ti and Ni was produced at the regions where the TiC particle was in contact with Ni phase in the two-phase alloy (high temperature erosion-oxidation test: T°C = 850, $v$ = 20 m/s, $\alpha = 60^{o}$).

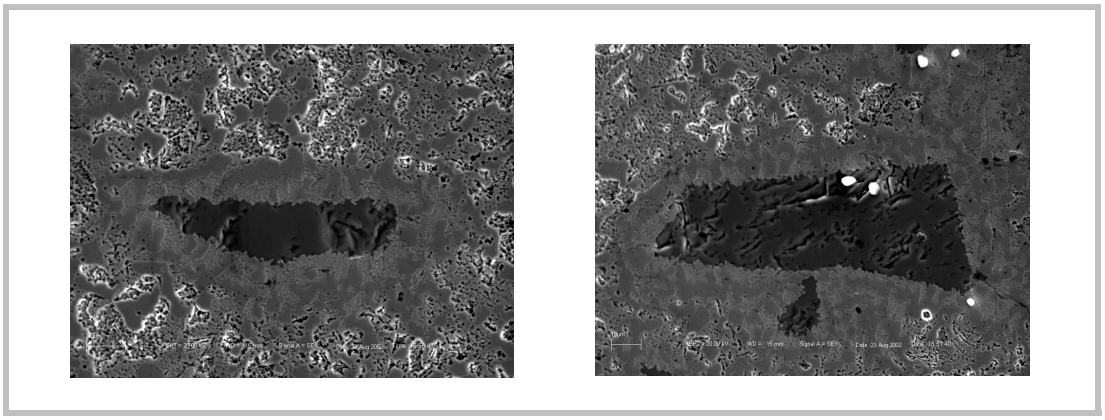

Fig. 4.17 SEM observation indicating the interfacial reaction at metal/ceramic interface in a TiC/INCONEL 671 composite. A thick layer of intermetallic compound consisting of Ti and Ni was produced at the regions where the TiC particle was in contact with Ni phase in the two-phase matrix. While, debonding was observable at the places where the TiC was in contact with the Cr phase (high temperature erosion-oxidation test: T°C = 850, $v$ = 20 m/s, $\alpha = 60^{o}$).

The plastic zone size $L$ was also measured on selected materials tested under the erosion-oxidation conditions. As in the case of the erosion test, such a zone could be identified only on the eroded surface of the steel alloys and the $Al_2O_3$ reinforced composites. However, $L$ appears to be a valid parameter in predicting the relative erosion resistance only for the steel alloys. Comparing the erosion performance of 253MA and APM9935, one can see that higher resistance corresponds to shorter $L$ (refer to Fig. 3.6 (a) and Table 3.3).

*L* appears not to be a valid parameter in predicting the relative erosion resistance of composite to the corresponding matrix alloy under the erosion-oxidation conditions. The $Al_2O_3$/APM9935 composite had a larger *L* compared to that of the reinforcement-free matrix, but exhibited clearly higher erosion resistance. Besides the residual strain argument, the high temperature involved might have an annealing effect on the plastic straining at the sample surface, and this effect was more pronounced with the reinforcement-free matrix than with the composite.

## 4.3 Erosion-oxidation Behaviour of Stainless Steel Based Composites

The erosion-oxidation resistance of stainless steel reinforced composites, namely, $Al_2O_3$/AISI 316 and $C_3C_2$/Duploc 27, were investigated in the first stage of the study. The poor performance of these composite systems caused their elimination from further studies. From the forgoing discussion, it is clear that high bonding strength at the metal/ceramic interface, good chemical stability of the reinforcement and sufficient matrix strength and toughness at high-temperature are desired for good erosion-oxidation resistance of composites. Here, the erosion-oxidation behaviour of the stainless steel composites provides supporting information for these ideas.

The most significant features on the eroded surface of the $Al_2O_3$/AISI 316 composite are the severe roughness in the matrix region and the remaining thick oxidising layer. Fig. 4.18 demonstrates a series of EDS analysis in a reinforcement-free area at the eroded surface of the $Al_2O_3$/AISI 316 composite.

The first analysis (Fig. 4.18 (a)) shows a freshly exposed ridge of the matrix alloy at which high oxidation rate and easy material remove can be expected. The second and third analyses (Fig. 4.18 (b), (c)) were carried out in the nearby and erosive particle doped area. It is clear that the matrix alloy had a low strength at high temperature as the $SiO_2$ particles, large or small, could be deeply embedded into the matrix. The formation of a thick oxide layer and its easy detachment would obviously be the next event. The structure of the oxide was not investigated but the EDS analysis indicates that it consisted of Fe and Cr. This is in accord with the common knowledge of high temperature oxidation of Fe-Cr alloy for which the Cr concentration is under 20% [89].

On the contrary, no detectable oxide layer could be found by EDS on the specimen surface of all the materials in the second stage of the study. Therefore, the low strength and high oxidation rate at high temperature contributed to the poor erosion-oxidation resistance of the $Al_2O_3$/AISI 316 composite, even though the bonding at the metal/ceramic interface was sound.

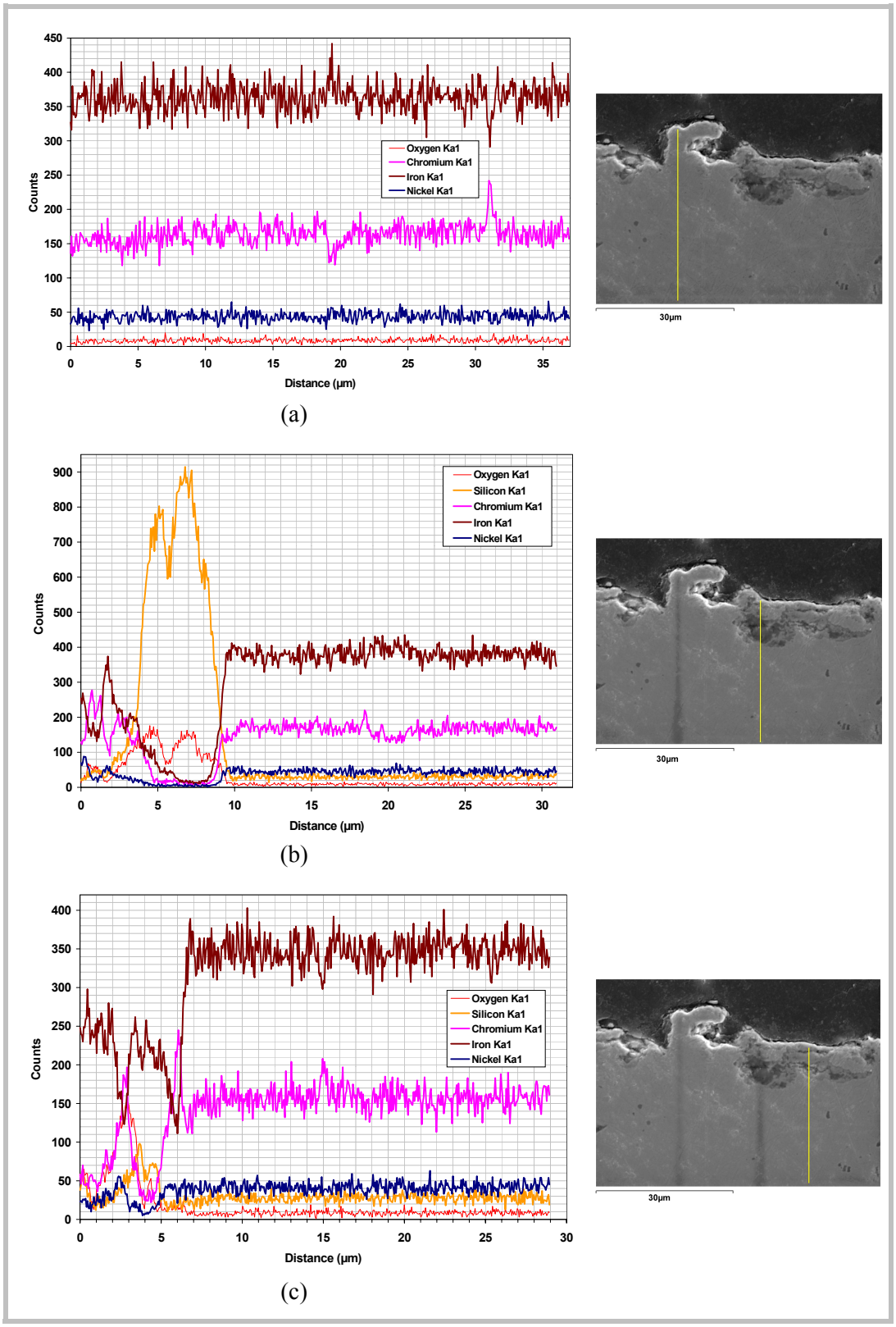


Fig. 4. 18 A series of EDS analysis indicating surface roughening and oxidising at the reinforcement-free area in the $Al_2O_3$/AISI 316 composite tested in the first stage study (high temperature erosion-oxidation test: T°C = 850, $v$ = 20 m/s, $\alpha$ = 60°).

In the case of the $Cr_3C_2$/D27 composite, decomposition of the matrix and reaction of the reinforcement are the most significant features. Figure 4.19 presents a EDS analysis cross a $Cr_3C_2$ particle. It is clear that reaction of the reinforcement particle with the matrix alloy occurred at the interfacial region, leading to a compositional modification of the reinforcing phase. In a separate study, it has been shown that such a modification may occur during the HIPing process [151]. Therefore, the situation only worsened under the high temperature erosion-oxidation conditions. The SEM observation demonstrates the interface reaction and the severe damage at the eroded surface (Fig. 4.20). The erosion impact caused not only material remove at the surface but also cracking in the sub-surface layers. The cracks, parallel to the eroded surface, went through the $Cr_3C_2$ particles and continued into the matrix, which became brittle because of decomposition.

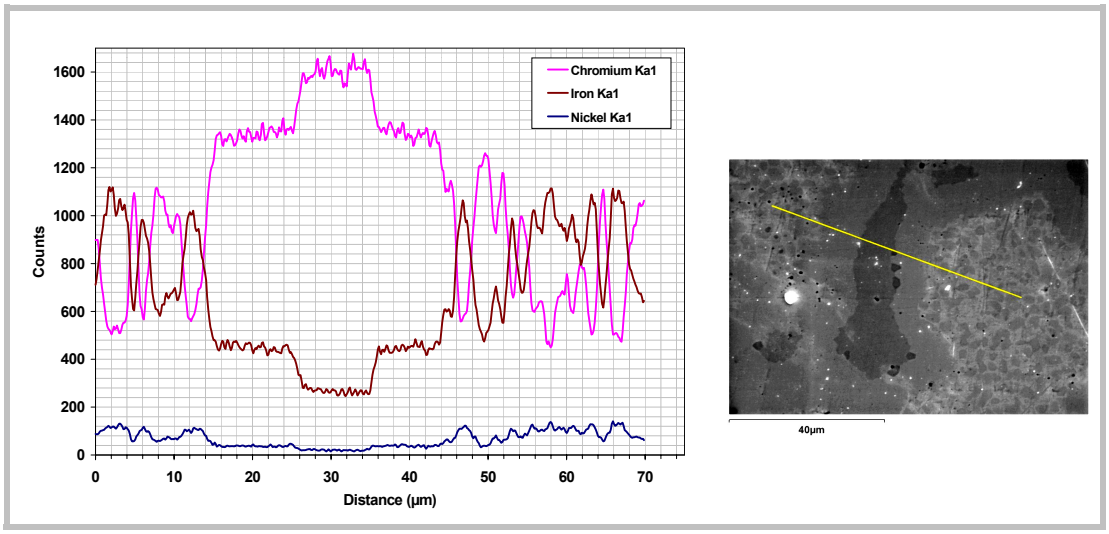


Fig. 5. 19 EDS analysis indicating interfacial reaction and matrix decomposition in the $Cr_3C_2$/D27 composite tested in the first stage study (high temperature erosion-oxidation test: T°C = 850, $v$ = 20 m/s, $\alpha$ = 60°).

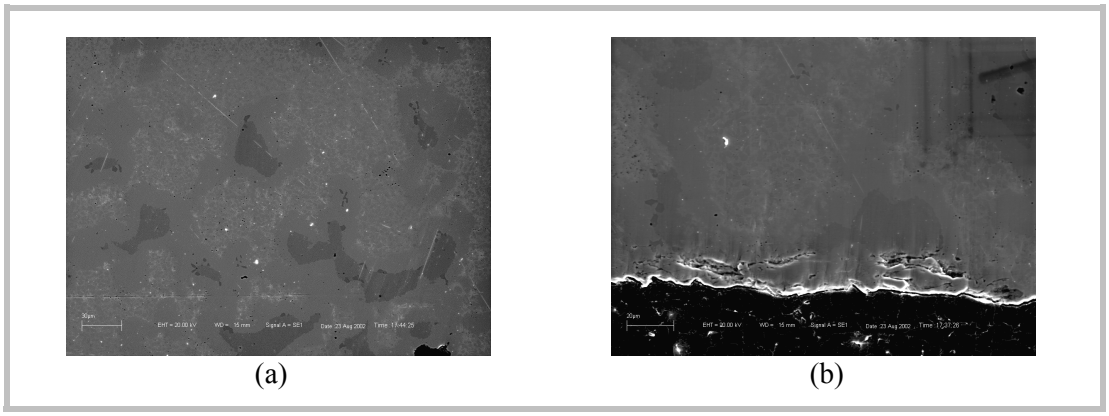


Fig. 4. 20 SEM observation of (a) reaction between the matrix and the reinforcement, and (b) sub-surface cracking in a $Cr_3C_2$/D27 composite tested in the first stage study (high temperature erosion-oxidation test: T°C = 850, $v$ = 20 m/s, $\alpha$ = 60°).

## 4.4 Summary

The forgoing discussion on the experimental results presents a general picture of the erosion and erosion-oxidation of MMC materials. Under room temperature erosion conditions, the erosion rate of the composites was determined mainly by the erosion response of the reinforcing phase. The erosion response of the reinforcement was also critical in the erosion-oxidation test. However, in addition to sound bonding at the metal/ceramic interface, high oxidation resistance and good high-temperature strength of matrix were also desired for a composite system to resist erosion-oxidation. While the strain localisation model can well explain the erosion of ductile metals as a physical phenomenon, its applicability to MMCs has not been proved in this study. However, it seems that the analysing method needs to be modified for a full test of this model.

It has been demonstrated in the study that composite materials exhibited unexceptionally inferior erosion resistance to their reinforcement-free matrices under the room temperature erosion conditions. This, however, should not be treated as a general trend of MMCs in against erosive attack. The erosion of MMCs is determined by not only the internal parameters of the composites, but also external factors involving all parameters of erosion. To improve the erosion resistance of MMC materials, the considerations are twofold: improve the intrinsic properties of the composites, and select better composite system to encounter harder erosive conditions

While this work is focused on the second stage study and a $60^{o}$ angle of impact, the understanding of erosion mechanisms of MMCs is enhanced by the material performance under other impact angles as well as in the first and third stage study.

The results from the first and second stage study demonstrate a trend whereby, as the impact angle changed from $60^{o}$ to $30^{o}$ and $15^{o}$, more composites performed batter than the corresponding matrix alloys in the erosion test. The lowered impact angle had two effects: lowering the erosion rate of the brittle reinforcement while increasing the rate of the ductile matrix (refer to Fig. 1.13). Apparently, the former was dominant, which supports the idea that the erosion performance of composites depends on the erosion responses of the reinforcing phase. Besides, the impact energy was also reduced with the decreasing impact angle, which led to less possibility of breakdown of the reinforcement particles and, therefore, better composite performance.

Regarding the erosion-oxidation behaviour of the composites, the preliminary results from a field test, in the third stage study, suggest that erosion degradation can become negligible if the impact energy is sufficiently low and the matrix oxidation rate is minimal. In the related erosion-oxidation test, the average particle velocity of impact was under 10 m/s, the oxygen concentration was 3-5% and the temperature was $750^{o}$C. Compared to those in the second stage study (Table 2.9), these conditions were considerably less severe. In the field test, a static oxidation test paralleled to the erosion test was conducted using duplicated specimens in a

similar atmosphere under 850$^{o}$C. Analysis of the results from the two tests demonstrates that the erosive losses of two superalloy composites, namely TiC/INCONEL 671 and $Cr_3C_2$/NIMONIC 81, were negligible. The thickness losses in the erosion test were actually lower than those recorded from the static oxidation test, suggesting that the mechanism of material degradation was pure oxidation. On the other hand, the static oxidation loss of a steel composite, $Al_2O_3$/AISI 316, was dramatically higher than that of the superalloy composites. This high level of thickness loss was more than doubled in the erosion test, suggesting that the mechanism of material degradation for the steel composite is erosion enhanced oxidation.

The applicability of the strain localisation model in ranking erosion resistance of ductile metals is promising. However, the validity of such an application on MMC materials is unclear. On the other hand, some MMCs have shown potential to offer good erosion resistance under certain erosion conditions. Therefore, it is of great interest for engineering applications that a simple testing procedure can be relied on for preliminary material selection in dealing with erosion and/or erosion-oxidation problems. It is postulated that conduction of single impact tests at an angle of 90$^{o}$ using a specially designed device may offer a solution. In such a test, the plastic zone is well established and, therefore, the plastic zone size ($L$) can be precisely defined.

Finally, it is clear that better testing arrangements are necessary in the further study in order to have more reproducible results. A new test device that is capable to produce a much more focused erosive beam on the surface of a single test piece has been constructed, and new tests with shortened test duration will be arranged. In practice, this means that more tests can be implemented, and more statistically sound results can be achieved.

# 5. Conclusions

Room temperature erosion and high temperature erosion-oxidation tests were implemented on heat-resistant steels, superalloys, and on the corresponding composites. An understanding of erosion as a physical phenomenon has been established, from which discussion of the experimental results is carried out. The following conclusions are reached from this study.

Under room temperature erosion conditions, the composites were inferior to the related reinforcement-free matrix alloys in resisting erosion attack. This is ascribed to the easy removal of broken reinforcement particles in large scale, leaving the surrounding matrix alloy vulnerable to successive impacts. The relative erosion resistance of the composites depended on the erosion pattern of the reinforcements. In the case of the $Al_2O_3$ reinforced composites, the massive breakdown of the $Al_2O_3$ particles was in a pure brittle manner, and consequently the erosion resistance of the composites was very poor. In the case of the $Cr_3C_2$ and TiC reinforced composites, the reinforcement particles were chipped off in small pieces with signs of plastic deformation occurring in the course of material removal. This led to higher composite erosion resistance. As the breakdown of the reinforcing phases was the dominant event in the erosion, the bonding situation at the metal/ceramic interface seemed unimportant.

Under high temperature erosion-oxidation conditions, certain composites exhibited higher resistance than the reference material. The worst performing $Al_2O_3$ composites in the erosion test became the best performing ones in the erosion-oxidation test. This was because the reduced impact energy in this test was insufficient to induce massive breakdown of the reinforcement, and the $Al_2O_3$ reinforcement was in a low rate erosion regime. In addition, the bonding strength was found improved under the test conditions. Moreover, a thin interface layer of diffusion type with a planer front is shown beneficial to the bonding strength. The protruding $Al_2O_3$ particles on the eroded surface represent a unique feature of the beneficial effect of reinforcement by which the overall erosion resistance of the composite is enhanced.

On the other hand, in the erosion-oxidation test, interfacial reactions at the TiC/matrix interface and reinforcement dissolution at the $Cr_3C_2$/matrix interface became more significant in the related composites, rendered the reinforcement strength and matrix toughness poor. As a result, the reinforcements offered no protection to the matrix alloys but were detrimental to the overall resistance of the composites.

Besides the bonding strength and chemical stability of the reinforcement, matrix strength at high temperature became more important under erosion-oxidation conditions. This is because under same erosion conditions, the eroded surface of a high strength alloy will be less roughened and consequently the oxidation rate will be low since the surface-to-volume ratio is low. At this point, the strengthening effect of reinforcement, especially at elevated temperatures, is of potential benefit to the composite erosion. In this study, the relatively high erosion resistance of

the NIMONIC 81 composite with 30 vol% $Cr_3C_2$ can be partially ascribed to its high temperature strength.

Based on the idea of strain localisation in erosion of ductile metals, the practical method of ranking materials in resisting erosion is promising with regard to ductile alloys. For alloys of identical type, lower $L$ indicates in general a better erosion resistance. As for the MMC materials in this study, $L$ can not be properly identified on the eroded surface. However, with modified measuring procedure to account for the effects of matrix/reinforcement interaction, it is believed that $L$ can be well defined and, therefore, the erosion performance of MMC materials can be compared.

## References


1. R. A. C. Mayville, A. K. Rao and R. P. Wilson, Jr.: Durable component development progress for the Cooper-Bessamer coal-fueled diesel engine, *ICE-Vol. 14, Coal-Fueled Diesel Engines*, ASME, New York, 1991.
2. Iain Finnie: Some reflections on the past and future of erosion, *Wear*, 1995, vol. 186-187, pp. 1-10.
3. C. M. Preece and N. H. Macmillan, in: *Erosion*, R. A. Huggins et al. eds., *Ann. Re. Mater. Sci.*, Annual Reviews Inc., Palo Alto, CA, 1977, pp. 95-121.
4. W. F. Adler: Assessment of the state of knowledge pertaining to solid particle erosion, *Report No. CR 79-680*, 30 June 1979, US Army Research Office Control DAA C29-77-C-0039.
5. A. W. Ruff and S. M. Wiederhorn: Erosion by solid particle impact, in: Treatise on Materials Science and Technology, C. M. Preece ed., Academic Press, New York, 1979, Vol. 16, pp. 69-126.
6. G. P. Tilly, in: *Erosion caused by impact of solid particles in wear*, D. Scott ed., Treaties on Material Science and Technology, Vol. 13, Academic Press, 1979.
7. W. F. Adler ed., *Erosion: Prevention and Useful Applications*, ASTM STP664, 1979.
8. P. Shewman and G. Sundararajan, in: *The erosion of metals*, Annual Review of Material Science, R. A. Huggins et al. eds., Annual Reviews Ins., Palo Alto, CA, 1983, pp. 301-318.
9. S. M. Wiederhorn and B. H. Hockey: Effect of material parameters on the erosion resistance of brittle materials, *J. Mater. Sci.,* 1983, vol. 18, pp. 766-780.
10. J. E. Ritter (ed.): *Erosion of Ceramic Materials*, Trans. Tech. Publications, Zurich, Switzerland, 1992.
11. J. G. A. Bitter: A study of erosion phenomena: Part I, *Wear*, 1963, vol. 6, pp. 5-21.
12. J. G. A. Bitter: A study of erosion phenomena: Part II, *Wear*, 1963, vol. 6, pp. 169-190.
13. I. Finnie, A. Levy and D. H. McFadden, in: *Erosion: Prevention and Useful Applications*, W. F. Adler ed., ASTM STP664, 1979, pp. 36-58.
14. I. Finnie and D. H. McFadden: On the velocity dependence of the erosion of ductile metals by solid particles at low angles of incidence, *Wear*, 1978, vol. 48, pp. 181-190.
15. I. Finnie and J. Wolak and Y. H. Kabil: Erosion of metals by solid particles, *J. Mater.*, 1967, vol. 12, pp. 682-700.
16. L. L. Brass: *The Effects of Microstructure of Ductile Alloys on Solid Particle Erosion*, MS Thesis in Materials Science and Engineering, University of California, Berkeley, Calif., June 1977.
17. I. M. Hutchings, in: *Erosion: Prevention and Useful Applications*, W. F. Adler ed., ASTM STP664, 1979, pp. 59-76.
18. I. M. Hutchings, R. E. Winter and J. E. Field: Solid particle erosion of metals: the removal of surface material by spherical projectiles, *Proc. Roy. Soc. London*, 1976, vol. A348, pp. 379-392.

19. I. M. Hutchings: Deformation of Metal Surfaces by the Oblique Impact of Square Plates, *Int. J. mech. Sci.*, 1977, vol. 19, pp. 45-52.

20. I. M. Hutchings: A model for the erosion of metals by spherical particles at normal incidence, *Wear*, 1981, vol. 70, pp. 269-81.

21. S. B. Ratner and E. E. Styller: Characteristics of impact friction and wear of polymeric materials, *Wear*, 1981, vol. 73, pp. 213-34.

22. P. S. Follansbee, G. B. Sinclair and J. C. Williams: Modelling of low velocity particulate erosion in ductile materials by spherical particles, *Wear*, 74 1982, vol. 74, pp. 107-22.

23. S. Jahanmir: The mechanics of subsurface change in solid particle erosion, *Wear*, 1980, vol. 61, pp. 309-24.

24. R. Brown, E. J. Jun and J. W. Edington: Erosion of α-Fe by spherical glass particles, *Wear*, 1981, vol. 70, pp. 347-63.

25. G. Sundararajan: An analysis of the localisation of deformation and weight loss during single-particle normal impact, *Wear*, 1982, vol. 84, pp. 217-35.

26. G. Sundararajan and P. G. Shewmon: A new model for the erosion or metals at normal incident, *Wear*, 1983, vol. 84, pp. 237-58.

27. G. Sundararajan: The solid particle erosion of metallic materials: the rationalisation of the influence of material variables, *Wear,* 1995, vol. 186-187, pp. 129-44.

28. S. Trilok, S. N. Tiwari and G. Sundararajan: Room temperature erosion behaviour of 304, 316 and 410 stainless steels, *Wear,* 1991, vol. 145, pp. 77-100.

29. K. P. Balan, A. V. Reddy, V. Joshi and G. Sundararajan: The influence of microstructure on the erosion behaviour of cast irons, *Wear*, 1991, vol. 145, pp. 283-96.

30. M. Roy, Y. Tirupataiah and G. Sundararajan: Effect of particle shape on the erosion of Cu and its alloys, *Mater. Sci. Eng*., 1993, vol. A165, pp. 51-63.

31. M. Roy, Y. Tirupataiah and G. Sundararajan: Influence of solid solution and dispersion strengthening mechanisms on room temperature erosion behaviour of Nickel,. *Mater. Sci. Tech.*, 1995, vol. 11, pp. 791-97.

32. M. Roy, M. Subramaniyam and G. Sundararajan: Room temperature erosion behaviour of a precipitation hardened stainless steel, *Tribol. Int*., 1992, vol. 25, pp. 271-280.

33. S. Srinivasan, R. O. Scattergood and R. Warren: Erosion of fibre-reinforced Al-4 pct Cu composites, *Metall. Trans*., 1988, vol. 19A, pp. 1785-93.

34. I. M. Hutchings, Strain rate effects in microparticle impact, *J. Phys. D: Appl. Phys*., 1977, vol. 10, pp. L179-84.

35. Y. Tirupataiah, G. Sundararajan, A dynamic indentation technique for the characterization of the high strain rate plastic flow behaviour of ductile metals and alloys, *J. Mech. Phys. Solids*, 1991, vol. 39, pp. 243-271.

36. J. D. Campbell: Dynamic plasticity: macroscopic and microscopic aspects, *Mater. Sci. Eng*., 1973, vol. 12, pp. 3-21.

37. A. V. Reddy and G. Sundararajan: The influence of grain size on the erosion rate of metals, *Metall. Trans*., 1987, vol. 18A, pp. 1043-52.

38. M. Naim and S. Bahadur: Effect of microstructure and mechanical properties on the erosion of 18Ni (250) maraging steel, *Wear*, 1986, vol. 112 , pp. 217-34.

39. L. P. McCabe, G. A. Sargent and H. Conrad: Effect of microstructure on the erosion of steel by solid particles, *Wear*, 1985, vol. 105, pp. 257-77.

40. A. V. Levy: Platelet mechanism of erosion of ductile metals, *Wear*, 1986, vol. 108, pp. 1-22.

41. G. Sundararajan: The depth of plastic deformation beneath eroded surface: the influence of impact angle and velocity, particle shape and material properties, *Wear*, 1991, vol. 149, pp. 129-53.

42. H. O'Neill: *The Hardness of Metals and Alloys*, Chapmen & Hall, London, 1967.

43. C. H. Lee, S. Masaki and S. Kobayashi: Analysis of ball indentation, *Int. J. Mech. Sci*., 1972, vol. 14, pp. 417-426.

44. Y. Tirupataiah and G. Sundararajan: A comprehensive analysis of the static indentation process, *Mater. Sci. Eng*., 1987, vol. 91, pp. 169-180.

45. G. Sundararajan and P. G. Shewmon: The use of dynamic impact experiments in the determination of the strain rate sensitivity of metals and alloys, *Acta metall*., 1983, vol. 31, pp. 101-09.

46. D. Tabor, *The hardness of Metals*, Clarendon, Oxford, 1951.

47. G. Sundararajan: A comprehensive model for the solid particle erosion of ductile metals, *Wear*, 1991, vol. 149, pp. 111-27.

48. A. G. Atkins and D. Tabor: *J. Mech. Phys. Solids*, 1965, vol. 13, pp. 149-153.

49. A. V. Reddy, and G. Sundararajan: The effect of stacking fault energy on the erosion behaviour of copper alloys at oblique impact, *Wear*, 1985, vol. 103, pp. 133-48.

50. M. Roy, Y. Tirupataiah and G. Sundararajan: Influence of solid solution and dispersion strengthening mechanisms on room temperature erosion behaviour of nickel, *Mater. Sci. Tech.*, 1995, vol.11, pp. 791-97.

51. G. Sundararajan: The differential effect of the hardness of metallic materials on their erosion and abrasion resistance, *Wear*, 1993, vol. 162-164, pp. 773-81.

52. T. Singh, S. N. Tiwari and G. Sundararajan: Room temperature erosion behaviour of 304, 316 and 410 stainless steels, *Wear*, 1991, vol. 145, pp. 77-100.

53. G. L. Shldon and I. Finnie: On the ductile behavior of nominally brittle materials during erosive cutting, *J. Eng. Ind*. 1966, vol. 88B, pp. 387-392.

54. I. M. Hutchings: Ductile-brittle transitions and wear maps for the erosion and abrasion of brittle materials, *J. Phys. D: Appl. Phys.*, 1992, vol. 25, pp. A212-21.

55. A. G. Evans: in *Treatise on Materials Science and Technology*, C. M. Preece ed., Academic Press, New York, 1979, Vol. 16, pp. 1-67.

56. A. G. Evans, M. E. Gulden and M. E. Rosenblatt: Impact damage in brittle materials in the elastic-plastic response regime, *Proc. Roy. Soc. London*, 1978, vol. 361A, pp. 343-365.

57. B. J. Hockey and B. R. Lawn: Electron microscopy of microcracking about indentations in aluminum oxide and silicon carbide, *J. Mater. Sci*. 1975, vol. 10, pp. 1275-1284.

58. B. R. Lawn, B. J. Hockey and S. M. Wiederhorn: Atomically sharp cracks in brittle solids: an electron microscopy study, *J. Mater. Sci*. 1980, vol. 15, pp. 1207-1223.

59. S. M. Wiederhorn and B. R. Lawn: Strength degradation of glass impacted with sharp particles: I, Annealed surfaces, *J. Amer.Ceram. Soc*., 1979, vol. 62, pp. 66-70.

60. M. A. Verspui: Modelling abrasive process of glass, Ph.D thesis, Technische Universitieit Eindhoven,

61. P. J. Slikkerver, P. C. P. Bouten, F. H. in't Veld and H. Scholten: Erosion and damage by sharp particles, *Wear*, 1998, vol. 217, pp. 237-250.'

62. I. Finnie, J. Wolak and Y. Kabel: Erosion of metals by solid particles, *J. Mater*, 1967, vol. 2(3), pp. 682-700.

63. M. Buijs and J. M. Pamans: Erosion of glass by alumina particles, *Wear*, 1995, vol. 184, pp. 61-65.

64. S. M. Wiederhorn and B. J. Hockey: Effect of material parameters on the erosion resistance of brittle materials, *J. Mater. Sci.*, 1983, vol. 18, pp. 766-780.

65. S. Sernuvasan and R. O. Scattergood: Effect of erodent hardness on erosion of brittle materials, *Wear*, 1988, vol. 128, pp. 139-152.

66. Z. Feng and A Ball: The erosion of four materials using seven erodents — towards an understanding, *Wear*, 1999, vol. 233-235, pp. 674-684.

67. A. G. Evans, Strength degradation by projectile impacts, *J. Amer.Ceram. Soc*., 1973, vol. 56, pp. 405-409.

68. B. R. Lawn: Hertzian fracture in single crystals with the diamond structure, *J. Appl. Phys.,* 1968, vol. 39, pp. 4824-4836.

69. C. G. Knight, M. V. Swan and M. M. Chaudhri: Impact of small steel sphere on glass surfaces, *J. Mater. Sci.*, 1977, vol. 12, pp. 1573-1586.

70. M. M. Chaudhri and S. M. Walley: Damage to glass surfaces by the impact of small glass and steel spheres, *Phil. Magaz*., 1978, vol. A37, pp. 153-165.

71. F. C. Frank and B. R. Lawn: Theory of Hertzian fracture, *Proc. Roy. Soc. London*, 1967, vol. A299, pp. 291-306.

72. S. M. Wiederhorn and B. R. Lawn: Strength degradation of glass resulting from impact with sphere, *J. Amer.Ceram. Soc*., 1977, vol. 66, pp. 451-458.

73. B. R. Lawn and R. Wilshaw: Review Indentation fracture: principles and applications, *J. Mater. Sci.*, 1975, vol. 10, pp. 1049-1081.

74. I. M. Hutchings: Strain rate effects in microparticle impact, *J. Phys. D: Appl. Phys.*, 1977, vol. 10, pp. L179-L184.

75. D. B. Marshall, B. R. Lawn and A. G. Evans: Elastic/plastic indentation damage in ceramics: The lateral crack system, *J. Amer.Ceram. Soc*., 1982, vol. 65, pp. 561-566.

76. T. Deng, M. S. A. Bradley and M. S. Bingley: An investigation of dynamics within a centrifugal accelerator type erosion tester, *Wear*, 2001, vol. 247, pp. 55-65.

77. A. J. Burentt, M. S. A. Bradley, D. J. O' Flynn, T. Deng and M. S. Bingley: Anomalies in the results obtained from rotating disc accelerator erosion testers: a discussion of possible causes, *Wear*, 1999, vol. 233-235, pp. 275-283.
78. P. H. Shipway: The effect of plume divergence on the spatial distribution and magnitude of wear in gas-blast erosion, *Wear*, 1997, vol. 205, pp. 169-177.
79. A. J. Burnett, S. R. De Silva and A. R. Reed: Comparison between "send blast" and "centripetal effect accelerator" type erosion testers, *Wear*, 1995, vol. 186-187, pp. 168-178.
80. P. H. Shipway and I. M. Hutchings: Influence of nozzle roughness on conditions in a gas-blast erosion rig, *Wear*, 1993, vol. 162-164, pp. 148-158.
81. S. Söderberg, S. Hogmark, U. Engman and H. Swahn: Erosion classification of materials using a centrifugal erosion tester, *Trib. Int*., 1981, Dec., pp. 333-343.
82. I. R. Kleis: A test rig for the investigation of wear in a loose abrasive, *Trans. of the Tallinn Polytech. Inst.*, 1958, vol. 152, pp. 1-18.
83. A. Shimizu, Y. Yagi, H. Yoshida and T. Yokomine: Erosion of Gaseous Suspension Flow Duct Due to Particle Collision. I. Experimental Determination of Erosion Rate by Individual Collision, *J. Nucl. Sci. Technol*., 1993, vol. 30, No 9, pp. 881-889.
84. D. J. O'Flynn, A. J. Burnett and M. S. Bingley: proceedings of world tribology congress, London, UK, September, 1997, poster paper in session Wear by Hard Particles.
85. A. J. Burnett, M. S. A. Bradley, D. J. O´Flynn, T. Deng and M. S. Bingly: Anomalies in the results obtained from rotating disc accelerator erosion testers: a discussion of possible causes, *Wear*, 1999, Dec., vol. 233-235, pp. 275-283.
86. S. Dosanjh and J. A. C. Humphrey: The influence of turbulence on erosion by a particle laden fluid jet, *Wear*, 1985, vol. 103, pp. 309-330.
87. ASTM G76-89: Standard Practice for Conducting Erosion Tests by Solid Particle Impingement using Gas Jets, ASTM, Philadelphia, 1992.
88. D. R. Andrews and N. Horsfield: Particle collision in the vicinity of an eroding surface, *J. Appl. Phys*., 1983, vol. 16, pp. 525-538.
89. N. Birks and G. H. Meier: *Introduction to high temperature oxidation of metals*, Edward Arnold, London, 1983.
90. H. J. Engell: The concentration gradient of iron-ion-vacancies in wuctite scaling films and the mechanism of oxidation of iron, 1958, *Acta Met*., vol. 6, pp. 439-445.
91. D. Caplan and G. I. Sproule: Effect of oxide grain structure on the high-temperature oxidation of Cr, *Oxid. Metals*, 1975, vol. 9, pp. 459-472.
92. N. Birks and H. Rickert: The oxidation mechanism of some nickel-chromium alloys, *J. Inst. Met*., 1962-63, vol. 91, pp. 308-311.
93. J. D. Redmond and K. H. Miska: The basics of Stainless steels, *Chem. Eng*. 1982, vol. 18, pp. 79-93.
94. T. W. Clyne and P. J Withers: *An Introduction to Metal Matrix Composites*, Cambridge University Press, 1993, pp. 13-270.
95. C. F. Legzdins, I. V. Samarasekera and J. A. Meech: MMCX- An expert system for metal matrix composite selection and design, *Can. Metall.* 1997, vol. Q36, pp. 177-202.

96. Z. Hashin and S. Shtrikman. A variational approach to the effective magnetic permeability of multiphase materials, *J. Appl. Phys.*, 1962, vol. 33b, pp. 3125-3131.

97. Z. Hashin and S. Shtrikman. A variational approach in the theory of the elastic behaviour of multiphase materials, *J. Mech. Phys. Solids.*, 1963, vol. 11, pp. 127-140.

98. A. Mortensen: *Metal matrix composites: An overview*. In: Encyclopedia of Advanced Materials 1, D Bloor, RJ Flemings, and S Mahajan, eds., Cambridge: Pergamon Press 1993, pp 1497-1502.

99. H. J. Rack and P. Ratnaparkhi: Damage tolerance in discontinuously reinforced metal-matrix composites, *JOM.*, 1988, Nov., pp. 55-57.

100. M. Friend: Toughness in metal matrix composites. *Mats. Sci. & Tech.* 5 (1):, 1989, vol. 5(1), pp. 1-7.

101. A. J. Padkin, M. F. Boreton and W. J. Plumbridge: Fatigue crack growth in two-phase alloys, *Mat. Sci. Technol.*, 1987, vol. 3, pp. 217-223.

102. D. R. Williams and M. E. Fine: Quantitative determination of fatigue microcrack growth in $SiC_w$ reinforced 2124 Al alloy composites. Proceedings of 5th International Conference On Composite Matserials (ICCM V), San Diego. WC Harrigan, J Strife and AK Dhingra (eds.), TMS-AIME, 1985, pp 639-670.

103. T. Christman and S. Suresh: Effects of SiC reinforcement and aging treatment in fatigue crack growth in an Al-SiC composite, *Mater. Sci. Eng.* 102A (1988) 211-216.

104. K. S. Aradhya and M.K. Surappa: Estimation of mechanical properties of 6061 Al-$SiC_p$ composites using finite element method, *Scripta Met. et Mater.*, 1991, vol. 25, pp. 817-822.

105. L. H. Hihara and R. M. Latanision: Galvanic corrosion of aluminium-matrix composites, *Corros.*, 1992, vol. 48, pp. 546-552.

106. S.L. Coleman, V. D. Scott and B. McEnaney: Corrosion behaviour of aluminium-based metal matrix composites, *J. Mater. Sci.*, 1994, vol. 29, pp. 2826-2834.

107. C. Chen and F. Mansfeld: Corrosion protection on an Al 6092/$SiC_p$ metal matrix composite, *Corros. Sci.*, 1997, vol. 39, pp. 1075-1082.

108. K. P. Cooper and P. L. Slebodnick: Microstructural inhomogenities and sea water corrosion in laser-deposited Ti-6Al-4V alloy matrix/carbide particulate composite surfaces, *J. Mater. Sci.*, 1998, vol. 33, pp. 3805-3816.

109. M. R. Bache, W. J. Evans, A. L. Shakesheff, J. Shield and I. Uygur: Influence of aqueous salt environments on fatigue response of $SiC_p$ reinforced aluminium alloys, *Mater. Sci. Tech.*, 2000, vol. 16, pp. 825-829.

110. T. M. Yue, Y. X. Wu and H. C. Man: On the role $CuAl_2$ precipitates in pitting corrosion of aluminum 2009/$SiC_w$ metal matrix composite, *J. Mater. Sci. Lett.*, 2000, vol. 19, pp. 1003-1006.

111. Z. Ahmad, P. T. Paulette and B. J. A. Aleem: Mechanism of localized corrosion of aluminum-silicon carbide composites in a chloride containing environment, *J. Mater. Sci.*, 2000, vol. 35, pp. 2573-2579.

112. JM Evans and DM Braddick: Corrosion behaviour of fiber-reinforced Al composites, *Corros. Sci.*, 1971, vol. 11, pp. 611-614.

113. M. Saxena, O. P. Modi, A. H. Yegenswaran and P. K. Rohatgi: Corrosion characteristics of cast aluminium alloy--3 wt.% graphite particulate composites in different environments, *Corros. Sci.*, 1987, vol. 27(3), pp. 249-256.

114. D. M. Aylor and P. J. Moran: Effect of reinforcement on the pitting behaviour of aluminum-base metal matrix composites, *J. Electrochem. Soc.*, 1985, vol. 132, pp. 1277-1281.

115. P. M. Singh and J. J. Lewandowski: Stress corrosion cracking of discontinuously reinforced aluminum (DRA) alloy 2014 during slow strain rate testing, *J. Mater. Sci. Lett.*, 1996, vol. 15, pp. 490-493.

116. G. A. Rozak, J. J. Lewandowski, J. F. Wallace and A. Altmisoglu: Effects of casting conditions and deformation processing on A356 aluminum and A356-20 vol.% SiC composites, *J. Compos.*, 1992, vol. 26, pp. 2076-2106.

117. S. Suresh, T. Christman and Y. Sugimura: Accelerated aging in cast Al alloy-SiC particulate composites, *Script Metall.*, 1989, vol. 23, pp. 1599-1602.

118. I. Dutta, S. M. Allen and J. L. Hafley: Effect of reinforcement on the aging response of cast 6061 Al-$Al_2O_3$ particulate composites, *Metall. Trans.*, 1991, vol. 22A, pp. 2553-2563.

119. M. G. Fontana, N. D. Greene: Corrosion Engineering. 3rd ed., New York: McGraw-Hill Book Company, 1987, pp. 41-45.

120. Z. Feng and C: Lin. Pitting behaviour of $SiC_p$/2024 Al metal matrix composites, *J. Mate.r Sci.*, 1998, vol. 33, pp. 5637-5642.

121. P. P. Trazskoma: Pit morphology of aluminum alloy and silicon carbide/aluminum alloy metal matrix composites, *Corros.*, 1990, vol. 46, pp. 402-409.

122. F. Mansfeld, S. Liu, S. Kim and H Shih: Corrosion protection of Al alloy and Al-based metal matrix composites by chemical passivation, *Corros.*, 1989, vol. 45, pp. 615-630.

123. R. H. Jones, in: *Environmental effects on the advanced materials*, Proceedings of conference on environmental effects on advanced materials, TMS, Warrendala, PA, 1991, pp. 283-302.

124. L. H. Hihara and R. M. Latanision: Corrosion of metal matrix composites, *Int. Mater. Re.*, 1994, vol. 39, pp. 245-64.

125. L. H. Hihara and R. M. Latanision. Localized corrosion induced in graphite/aluminum metal-matrix composites by residual microstructural chloride, *Corros.*, 1991, vol. 47, pp. 335-341.

126. E. Rabinowicz, *Friction and wear of materials*, Wiley, London, 1996.

127. E. Hornbogen: The rule of fracture toughness in the wear of metals, *Wear*, 1975, vol. 33, pp. 251-259.

128. M. M. Khruschov: Principles of abrasive wear, *Wear*, 1974, vol. 28, pp. 69-88.

129. K.-H. Zum Gahr, "Abrasive Wear", in *Proc. 5th. Int. Congr. on Tribology* (Eurotrib′89), vol. 2, ed. K. Holmberg and I. Nieminen, Helsinki, 1984, 34-45.

130. T. E. Fischer, M. P. Anderson, S. Jahanmir: Influence of fracture toughness on the wear resistance of Yttria-doped Zirconium oxide, *J. Am. Ceram. Soc*., 1989, vol. 72, pp. 252-257.

131. E. Pagounis, M. Talvitie and V. K. Lindroos: Influence of reinforcement volume fraction and size on the microstructure and abrasion wear resistance of hot isostatic pressed white iron matrix composites, *Metall. Mater. Trans. A*, 1996, vol. 27A, pp. 4171-4181.

132. H. L. Lee, W. H. Lu and S. L. Chen: *J. Mater. Sci.*, 1992, vol. 24, pp. 40-47.

133. M. A. Zamzam: Abrasive Wear of Aluminium-Matrix Composites, *Metall*., 1991, vol. 45(3), pp. 250-254.

134. S. Skolianos, T. Z. Kattmis, Tribological properties of SiCp-reinforced Al-4.5&Cu-1.5%Mg alloy composites, *Mater. Sci. Eng A*., 1993, vol. A163, pp. 107-113.

135. A. T. Alpas, J. D. Embury: Sliding and abrasive wear behaviour of an aluminium, *Scripta Metall*., 1990, vol. 24, pp. 931-935.

136. R. A. Saravanan, M. K. Surappa and B. N. Pramila Bai: Erosion of A356 Al-$SiC_p$ composites due to multiple particle impact, *Wear*, 1997, vol. 202, pp. 154-164.

137. A. Wang and I. M. Hutchings, in *Metal and Ceramic Matrix Composites: Processing, modelling and mechanical behaviour*, R. B. Bhagat, A. H. Clauer, P. Kumar and A. M. Ritter eds., The Minerals, Metals and Materials Society, OH, 1990, pp. 499-508.

138. S. Turenne, D. Simard and M. Fiset: Influence of structural parameters on the slurry erosion resistance of squeeze-cast metal matrix composites, *Wear*, 1991, vol. 149, pp. 187-197.

139. S. Turenne, Y. Chatigny, D. Simard, S. Caron and J. Masounave: The effect of abrasive particle size on the slurry erosion resistance of particulate-reinforced aluminum alloy, *Wear*, 1990, vol. 141, pp. 147-158.

140. A. J. Ninham and A. V. Levy: The erosion of carbide-metal composites, *Wear*, 1988, vol. 121, pp. 347-361.

141. D. G. Rickerby and N. H. Macmillan: The erosion of aluminium by solid particle impingement at oblique incidence, *Wear*, 1982, vol. 79, pp. 171-190.

142. M. Ramulu, S. P. Raju, H. Inoue and J. Zeng: Hydro-abrasive erosion characteristics of 30 vol.% $SiC_p$ /6061-T6 Al composite at shallow impact angles, *Wear*, 1993, vol. 166, pp. 55-63.

143. X. W. Liu, On the mechanical and corrosion properties of TiN/654SMO metal matrix composite, master thesis, Helsinki University of Technology, 1996.

144. H. V. Atkinson and B. A. Rickinson, in "Hot Isostatic Processing", the Adam Hilger series on new manufacturing processes and materials, series editor: John Wood, H. I. P. Limited, 1991.

145. Institute of materials science, Tempere University of Technology.

146. R. Nieminen and T. Tiainen, Materials for waste fired boilers – Final report, Tampere University of Technology, Institute of Materials Science, Report 13/1992, 3-6.

147. E. Pagounis, M. Talvitie, V. K. Lindroos, Influence of the metal/ceramic interface on the microstructure and mechanical properties of HIPed iron-based composites, *Compos. Sci. and Tech.*, 1996, vol. 56, pp. 1329-1337.

148. J. M. Howe, Bonding, structure, and properties of metal/ceramic interfaces: Part 1 Chemical bonding, chemical reaction, and interfacial structure, *Int. Mater. Rev*., 38 (1993, vol. 38, pp. 233-256.

149. J. M. Howe, Bonding, structure, and properties of metal/ceramic interfaces: Part 2 Interface fracture behaviour and property measurement, *Int. Mater. Rev*., 1993, vol. 38, pp. 257-271.

150. P. L. Ratnaparkhi and J. M. Howe, Structure and mechanism of bonding at a diffusion-bonded Al/SiC interface, *Acta Metall. Mater*., 1994, vol. 42, pp. 811-823.

151. M. Heinonen: Microstructural control in the powder metallurgical processing of $Cr_3C_2$ reinforced steel matrix composites, master thesis, Helsinki University of Technology, 2000.

## Appendix A:

### Statement of Contribution

The author's contribution to the contents of the doctoral dissertation "A Study on the Erosion and Erosion-oxidation of Metal Matrix Composites", by Xuwen Liu, is specified as below.

The author has a full contribution to the entire **Introduction** part. The knowledge and the information presented in this part reflect the author's intensive reading and ponderation in comprehending the fundamentals and backgrounds of the subject of the manuscript.

The author has a significant contribution to the contents of the **Experiment** part, particularly in the selection of matrix alloy, determination of reinforcement particle size and volume fraction, sieving and mixing of powders, filling of mixtures into capsules for HIPing consolidation, sampling, post-test treating and measuring of test pieces. However, to the practical nature of the study, contributions of other members in the research group are indispensable to the completion and success of the whole body of the experimental work. The contributions of other project members are presented in appendix B, entitled to "Contributions of research group".

The author has, in terms of the methodology in data treatment, a unilateral contribution to the whole part of the **Results**. There are two points that the author wants to emphasise in particular. First, the author's idea of data rationalisation in the section concerning erosion-oxidation test is of a great importance, from which the material performance could be assessed, the possible mechanisms could be investigated, and the conclusions thereby could be reached. Second, the section of determination of plastic zone size is an approach to verify the author's understanding of erosion as a physical phenomenon.

The author has a full contribution to the entire parts of **Discussion** and **Conclusions**, of which the whole contents reflect an independent work of the author. To the information concerning the third stage of the study that is presented in the end of the **Discussion**, the author considers that other members' contributions are equally or more important.

Finally, it is important to notice that along with the experimental data dealt in the dissertation much more results from all the stages of the study are in possession by the research group.

## Appendix B:

### Contributions of research group

#### The project

The main part of research activities discussed below were carried out in Laboratory of Physical Metallurgy and Materials Science in Helsinki Universtity of Technology (HUT) during 1998-2001 in a project titled "Erosion and erosion-corrosion resistant powder metallurgical materials for the applications of energy technology (ERCOMAT)", which was part of "Materials for Energy Technology – KESTO Technology Programme 1997-2001" of National Technology Agency, Tekes. Fortum Oyj, Metso Powdermet Oy, Foster Wheeler Energia Oy, Wärtsilä Oyj participated the project as industrial sponsors. The research project was aimed to develop new powder metallurgical (PM) metal matrix composite (MMC) materials, which have improved erosion and erosion-corrosion resistance compared with materials currently utilized in the critical components of high temperature processes in energy technology. The research scientists in the project, which was headed by Professor Veikko Lindroos (4/1998-12/2001), were Mr. Jussi Hellman (4/1998-12/2001, Mr. Xuwen Liu (4/1998-12/2001), Mrs. Päivi Kivikytö-Reponen (5/1998-2/2000, 9-12/2001), Mrs. Desirée Luhulima (7/1998-8/2001), and Ms. Mirva Heinonen (10/1999-10/2000) in the Laboratory of Physical Metallurgy and Materials Science, HUT. Mr. Tuomo Viitala (7-12/1998) participated the weld-coating tests of the project in the Laboratory of Engineering Materials, HUT, and Mr. Mika Sirén (4-8/1998) and Mr. Topi Kosonen (8/1998-2/2001) carried out joining studies of MMC materials in the Technical Research Centre of Finland, VTT.

#### Contributor's roles and intellectual property rights

The selection and design of MMC materials for the experimental procedures was carried out by Hellman and Liu. The commercially available reference alloys were selected based on a published literature study by Kivikytö-Reponen, Liu, Hellman and Lindroos, and recommendations from the industrial sponsors of the project. The erosion test programme (room temperature erosion test with the centrifugal erosion tester) was designed by Hellman with important suggestions from Liu, and implemented by Hellman and Kivikytö-Reponen. Preparation of erosion test specimen was carried out by Liu and Luhulima. The procedure for investigation the topographic feature of the erosion test specimens was made by Liu, with the instructions on the finalisation and implementation of the procedure from Hellman. The assistance of Luhulima was important in the microscopy studies of the eroded specimen. The erosion-oxidation test programme (High temperature erosion-oxidation test using the gas-blast erosion tester) was planned by Hellman and Liu, while the experiments were carried out in Tampere University of Technology by local operator and supervised by Hellman. The analysis of topographic features of eroded materials was operated by Liu, while Hellman's suggestions were important. The procedure for analysis of cross-sectioned erosion-oxidation test specimen was designed by Liu and Hellman. The specimens were prepared and studied by means of scanning electron microscopy by Liu and Luhulima. The single-particle-impact-erosion studies were performed by Kivikytö-Reponen. The microhardness measurements were designed and carried out by Liu. The phase analysis of the MMC materials was carried out and reported by Heinonen (HUT) and Kosonen (VTT). The plasma transferred arc (PTA) weld-coating tests with MMC materials were operated and analysed by Viitala. The diffusion bonding and HIP (Hot isostatic pressing) joinability studies of MMC materials with steels were performed by Sirén and Kosonen.

Regarding the intellectual property rights of the members of the research group, the information on each contributor's role as above shall be presented in all publications derived from the experimental data and investigations of the project.